The Thesis Committee for Ebrahim Khalil Rasromani Certifies that this is the approved version of the following thesis:

Exploring Anisotropy in Rock Fluid Flow and Elastic Behavior

APPROVED BY
SUPERVISING COMMITTEE:

Supervisor:

Hugh Daigle

Co-Supervisor:

Kenneth Gray

Exploring Anisotropy in Rock Fluid Flow and Elastic Behavior

by

Ebrahim Khalil Rasromani, B.S.

Thesis

Presented to the Faculty of the Graduate School of

The University of Texas at Austin

in Partial Fulfillment

of the Requirements

for the Degree of

Master of Science in Engineering

The University of Texas at Austin

May 2016

Acknowledgements

I would like to thank the sponsors of the Wider Windows Industrial Affiliate Program and gratefully acknowledge the collaborative discussions with colleagues from British Petroleum, Chevron, ConocoPhillips, Marathon Oil, National Oilwell Varco, Occidental, and Shell. I would also like to acknowledge Dr. Kenneth Gray's dedication to the students in the Wider Windows Industrial Affiliate Program and thank Dr. Hugh Daigle for his input throughout my time in graduate school. Finally, I would like to thank Ho Eun Chae for helping with some of the initial research done.

Abstract

Exploring Anisotropy in Rock Fluid Flow and Elastic Behavior

Ebrahim Khalil Rasromani, M.S.

The University of Texas at Austin, 2016

Supervisor: Hugh Daigle, Kenneth Gray

The difficulty in modeling hydrocarbon reservoirs stems from their inherent anisotropic and heterogeneous nature. Due to their simplicity, isotropic fluid flow and geomechanical models are often used in industry. In comparison to the isotropic models, anisotropic models require more data to be collected for initialization and higher computational power for processing. The increasing complexity of reservoirs today and demand for higher accuracy production forecasting and better optimization of production and drilling development programs makes the case for the use of these more complex models. This thesis first presents a scheme for efficiently calculating the anisotropic permeability tensor to better represent the initial reservoir flow behavior. Various methods for modeling the change in permeability throughout the reservoir development are then explored. As hydrocarbons are produced and reservoir pressure depletes, the change in stress state induces a change in the reservoir permeability. The error associated with the assumption that permeability change is the same in all directions, often used in industry, is assessed by comparing an isotropic permeability change model to the strain-induced anisotropic permeability change model developed by Wong (2003) through a case study of a production well in Tor formation of Valhall field. The final part of the

thesis assesses the difference between the resulting fracture pressure predicted by the Kirsch equations and the Amadei solution to stress around a wellbore to demonstrate the importance of the incorporation of anisotropic elastic rock properties in geomechanical modeling of shale formations (Kirsch, 1898; Amadei, 1983). This is done through a case study of a horizontal well in the Lower Barnett Shale in Fort Worth Basin. Our results suggest that anisotropic reservoir behavior can be incorporated into reservoir models without a significant increase in computational power required and in some cases can significantly improve the prediction of the current and future reservoir state.

Table of Contents

List of Tables

List of Figures

Chapter 1: Introduction

To accurately predict the behavior of a reservoir the initial reservoir conditions must be well estimated and the appropriate models must be applied. Reservoir permeability is an important parameter to determine for reservoir production forecasting. In industry, permeability is typically measure in one direction, along the bedding plane, to minimize cost. In order to better capture the flow behavior of a reservoir, we present a scheme for assessing the directionality of reservoir permeability through calculation of the full permeability tensor in Chapter 2. The scheme involves the use of lattice-Boltzmann method (LBM) and the fast marching squared method (FMM^2) (Garrido et al., 2007). Through the FMM^2, the principal flow axes are identified and the normalized permeability tensor is estimated. With one LBM simulation, one can obtain the full permeability tensor by scaling the normalized permeability tensor by the unidirectional permeability obtained through LBM. Our results validate the application of the presented scheme in real rocks.

The determination of the initial reservoir permeability alone does not yield accurate long-term production forecasting. As hydrocarbons are produced and reservoir pressure depletes, the permeability of the reservoir changes due to the change in the reservoir stress state. Models that couple geomechanics and fluid flow must be incorporated into reservoir simulators for accurate determination of future production in depleting reservoirs. Most of the models in the literature assume that permeability changes are the same in all directions, even though deformation varies directionally (Mordecai and Morris, 1971; Gangi, 1978; Brace, 1980; Touhigi-Baghini, 1998). In Chapter 3, we compare the isotropic permeability change model commonly used in industry to a strain-induced anisotropic permeability change model presented by Wong

(2003). Through a case study of a vertical production well in the Tor formation of Valhall field, we evaluate the evolution of the near-wellbore and far-field permeability with depletion predicted by each model. The Kirsch equations are applied to obtain the stress distribution around the wellbore and the constitutive stress-strain relationship for isotropic elastic media is used to calculate the strain distribution (Kirsch, 1898). In the isotropic permeability alteration model, the change in permeability is related to the volumetric strain. In the anisotropic permeability alteration model, the change in the permeability tensor is a linear combination of elements of the strain tensor as specified by Wong (2003). Results indicate that the near-wellbore radial permeability with depletion is overestimated through the isotropic permeability alteration model and hence would yield inaccurate well performance predictions.

The Kirsch equations used in Chapter 3 assume isotropic elastic rock properties. Real rocks do not exhibit perfectly isotropic elastic behavior. Lekhnitskii (1963) developed a generalized version of the Kirsch equations for anisotropic elastic media. Amadei (1983) applied these equations to stress distribution around a deviated wellbore. The Amadei solution represents a more realistic representation of the stress distribution in both the near-wellbore and the far-field regions. Its application is simple as it is a fully analytical solution, but it faced much criticism due to an inherent singularity under special cases of symmetry (Ong, 1994; Ong and Roegiers, 1995). Gaede et al. (2012) have shown that this singularity, though mathematically apparent in theory, is unlikely to be encountered in real rocks. In Chapter 4, we compare fracture pressure predictions obtained through the Kirsch equations and the Amadei solution to evaluate the error associated with the assumption of isotropy of the elastic rock properties commonly used in industry (Kirsch, 1898; Amadei, 1983). This is done through a case study of a horizontal well in the Lower Barnett Shale of the Fort Worth Basin. As shale formations

exhibit anisotropic elastic behavior, we show that the fracture initiation pressure would be underestimated through the Kirsch equations and that the Amadei solution best represents stress distribution in anisotropic formations (Sone and Zoback, 2013).

Chapter 2: Estimating the anisotropic permeability tensor

Permeability is a routine laboratory measurement. Recent developments in numerical modeling have allowed for effective calculation of single-phase permeability numerically. Numerical techniques include computational fluid dynamics (CFD) and the lattice-Boltzmann method (LBM). For an accurate description of the flow properties of a porous medium, the permeability of the medium must be known in all directions. In order to obtain the permeability tensor of a porous medium, one must perform either multiple laboratory experiments or multiple numerical experiments of a core in different directions. Such a way of calculating the anisotropic permeability is time consuming and can be computationally expensive. This paper presents a scheme for quickly assessing the directionality of permeability through a variation on the fast marching method (FMM) termed fast marching square method (FMM^2) and introduced by Garrido et at. (2007). Given a computed tomography (CT) image of a core sample, results indicate that a combination of FMM^2 and LBM can be used to effectively calculate the anisotropic permeability tensor.

INTRODUCTION

Permeability is a measure of the ability of a porous medium to transmit a fluid. It was first defined as the proportionality constant between fluid flux, fluid properties and flow potential in Darcy's law (Darcy, 1856). It is often assumed that the permeability of a rock is isotropic, but real rocks are not perfectly isotropic and permeability is dependent on the direction of fluid flow (Freeze and Cherry, 1979). The directional nature of permeability requires it to be mathematically described as a second-order tensor rather than simply a scalar quantity. Real rocks tend to have a direction of maximum permeability and a direction of minimum permeability. The minimum and maximum

permeability directions are assumed to be orthogonal (Scheidegger, 1954). These directions identify the principal flow directions and can be mathematically described by the eigenvalues and eigenvectors of the permeability tensor.

Due to the increase in complexity in the reservoirs today, it is important to fully capture their flow behavior. The key to understanding the flow properties of a reservoir is to collect core samples from different depths and different locations in the reservoir to correctly account for heterogeneity throughout the reservoir. Permeability measurements can be made on these core samples. Most permeability measurements in the lab are conducted using non-reactive gases as the fluid to minimize the potential for permeability alteration from the interaction between the rock and the fluid (American Petroleum Institute, 1998; American Petroleum Institute, 1956). When rock samples are sensitive to drying techniques, a liquid is used as the fluid. Steady state and unsteady state permeability measurement techniques have been developed (Cui et al., 2009; Darabi et al., 2012; Darcy, 1856; Rushin et al., 2004; American Petroleum Institute, 1998). For conventional reservoirs, the steady state permeability measurement is usually done. This technique entails injection of a fluid in a specialized core holder to measure the relationship between flow rate and pressure gradient as the fluid is transmitted through the porous medium (American Petroleum Institute, 1998). The apparatus includes a pump or a pressurized gas cylinder, a Hassler core holder, flow meters and pressure gauges. Fluid is injected until pressure and flow rate stabilize. Both the fluid flow rate across the sample and the pressure differential between the upstream and downstream ends of the core are recorded to calculate the permeability through

$$k = \frac{q\mu L}{A(p_u - p_d)} \tag{2.1}$$

where k is the permeability, q is the fluid flow rate, μ is the viscosity, L is the core length, A is the core cross-sectional area and p_u and p_d are the upstream and downstream pressures (Darcy, 1856). If the fluid used is a gas, the measurement must be done several times at different pressure differentials to perform the Klinkenberg correction and account for gas slippage effects (Klinkenberg, 1941). If using a liquid, no correction is necessary but it's good practice to take several measurements with different flow rates and pressure gradients to make sure the results are consistent (American Petroleum Institute, 1998). The long time, up to a day, and high complexity of yielding an accurate measurement in the lab makes the case for numerical permeability measurements.

LBM has been successfully applied to permeability measurements of porous media (Gao et al., 2012). The main advantage of LBM over CFD is its ease of implementation and parallelization. LBM is a mesoscopic description for modeling fluid flow and its theory is based on non-equilibrium statistical mechanics and kinetic theory. More specifically, it involves the discretization of the Boltzmann transport equation. Rather than evaluating the motion of individual particles as is done in molecular dynamics, LBM involves evaluating the evolution of the particle probability distribution (Sukop and Throne, 2006). The particle probability distribution function, $f(\bar{x}, \bar{v}, t)$, is a function of position $\bar{x}$, microscopic velocity $\bar{v}$, and time t. $f(\bar{x}, \bar{v}, t)d\bar{x}d\bar{v}$ is the probability of finding a particle at time t positioned between $\bar{x}$ and $\bar{x} + d\bar{x}$ with velocity between $\bar{v}$ and $\bar{v} + d\bar{v}$. The Boltzmann transport equation is defined as

$$\frac{Df}{Dt} = \Omega \tag{2.2}$$

where f is the particle probability distribution function, D/Dt is the material derivative and Ω is the collision operator. In LBM, the evaluation space is discretized by confining particles in space to nodes on a uniform lattice such as that shown in Figure 1.

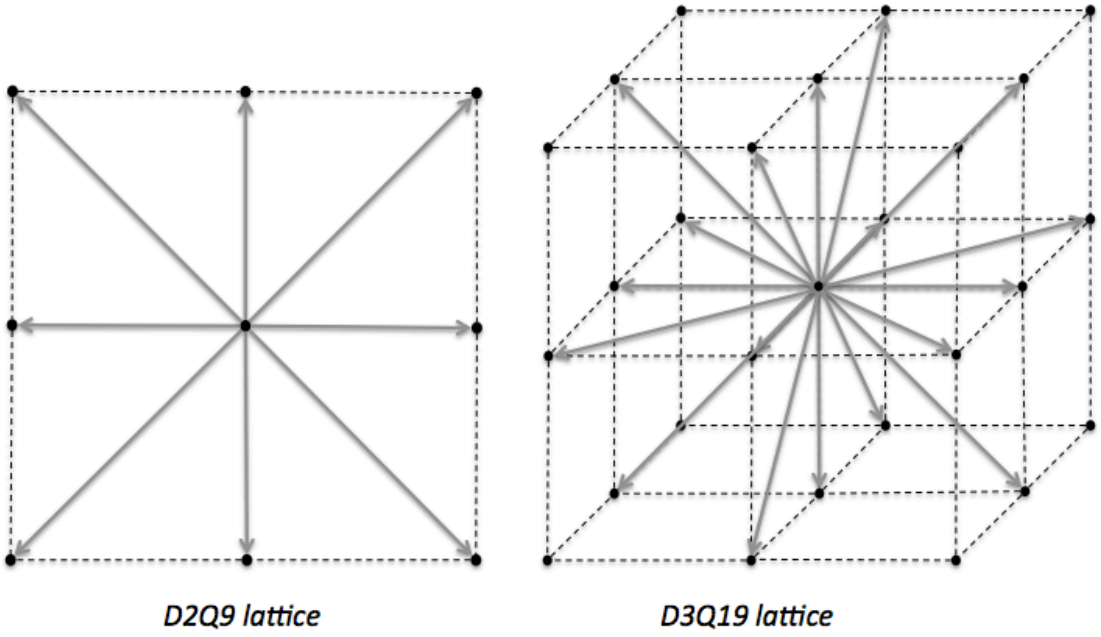

Figure 1: Typical D2Q9 and D3Q19 lattice used the lattice-Boltzmann method. DnQm refers to a lattice with in n dimensional space and m possible velocity directions.

Microscopic interactions are local and occur on a single node. The particles are restricted to move in the direction of the links between nodes. Because the allowed directions are limited, local equilibrium is incorporated to the local collision rules to recover the macroscopic fluid dynamic behavior. The Bhatnagar-Gross-Krook (BGK) collision operator is typically used for LBM given by

$$\Omega = -\frac{1}{\tau}(f - f^e) \tag{2.3}$$

where τ is the relaxation time constant and f^e is the equilibrium distribution function (Bhatnagar et al., 1954). The relaxation time constant determines the effectiveness of the microscopic dynamics moves towards the local equilibrium, hence inherently defines the fluid's viscosity. The Maxwell distribution function is used as the equilibrium function.

Macroscopic quantities such as fluid density ρ, macroscopic velocity $\bar{u}$, pressure p, and kinematic viscosity ν can be recovered from the mesoscopic description as shown in Equations 2.4a-2.4d.

$$\rho(\bar{x},t) = \int m\, f(\bar{x},\bar{v},t) d\bar{v} \tag{2.4a}$$

$$\rho(\bar{x},t)\, \bar{u}(\bar{x},t) = \int m\, \bar{v} f(\bar{x},\bar{v},t) d\bar{v} \tag{2.4b}$$

$$p(\bar{x},t) = {c_s}^2 \rho(\bar{x},t) \tag{2.4c}$$

$$\nu = {c_s}^2 \left(\tau - \frac{1}{2}\right) \tag{2.4d}$$

Note that m in Equations 2.4a-2.4b is the particle mass, and c_s is the speed of sound in Equation 2.4c-2.4d. The bounce-back boundary condition is typically used to implement the no-slip boundary. In the bounce-back boundary condition, a particle scatters back to the bulk fluid when it reaches a boundary node. This is done in such a way that mass and momentum are conserved (Zou and He, 1997).

In order to calculate permeability through LBM, the fluid must be driven to simulate the fluid flow in a porous medium. Narvaez and Harting (2010) have assessed various ways of driving fluid flow including fluid injection, pressure boundary condition and applied external force. Their results indicate that the pressure boundary condition is the most effective in porous medium fluid flow simulation. In LBM simulation, the pressure boundary condition is specified by setting the fluid density at the inlet and the outlet through Equation 2.4c. By choosing a value for the relaxation time constant and the pressure differential between the inlet and the outlet, one can calculate the permeability through Equation 2.1. The relaxation time constant and the pressure differential must be chosen such that the Reynolds number is low as Darcy's law for permeability calculation is only applicable in the laminar flow regime. Note that steady state must be reached in the LBM simulation to obtain an accurate permeability estimate.

Steady state is reached when the apparent permeability calculated at each time step stabilizes toward one value. The next section demonstrates an example of LBM used for numerical permeability measurement of porous media.

LATTICE-BOLTZMANN METHOD FOR SINGLE-DIRECTIONAL PERMEABILITY MEASUREMENT

We have used Palabos, an open-source solver based on the lattice-Boltzmann method, to simulate flow and calculate the system permeability (Latt, 2009). To validate our Palabos code, we simulate Couette flow in two-dimensions and compare our simulation results to the theory. We then apply LBM on an idealized pack of spherical grains to demonstrate its application to measure single-directional permeability of porous media.

Couette flow is the laminar flow of a Newtonian fluid between two parallel plates, with one plate moving relative to the other (Bird et al., 2007). For the code validation study, we consider the case were both plates are stationary. At fully developed steady state, the velocity profile is parabolic. The permeability of the system is given by $h^2/12$, where h is the distance between the parallel plates. A diagram of the Couette flow model and dimensions is shown in Figure 2. A lattice-Boltzmann simulation was performed through Palabos with D2Q9 lattice, depicted in Figure 1, and the BGK collision model (Bhatnagar et al., 1954). Bounce back boundary conditions were applied at the plate boundaries and Zou/He pressure boundary conditions were applied at the inlet and the outlet such that the pressure gradient is 0.0355 Pa/m (Zou and He, 1997). Note that the pressure gradient was chosen such that the flow is laminar by computing the Reynolds number and the Mach number. Details of the parameters used for the LBM simulation is shown in Table 1.

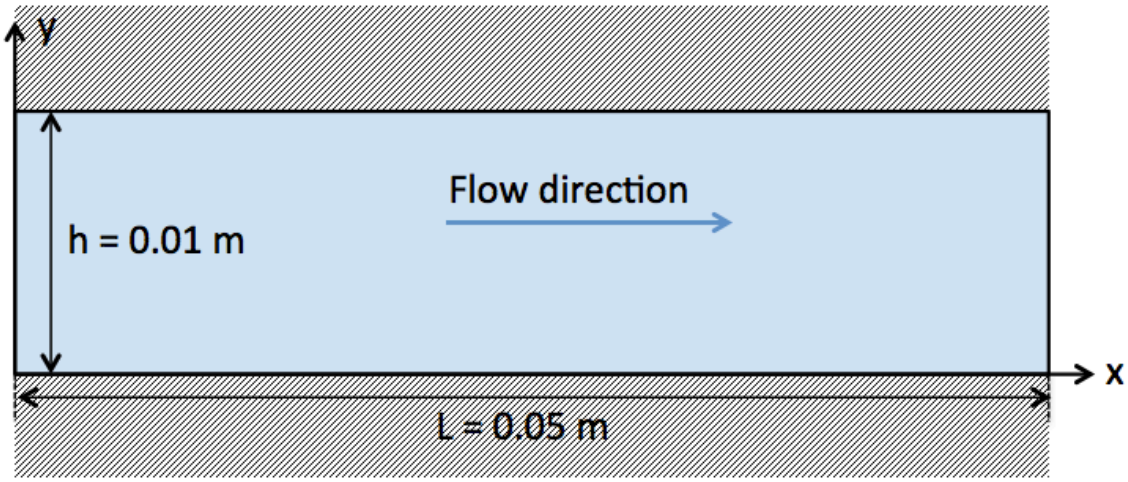

Figure 2: Couette flow diagram with model dimensions.

Table 1: Input parameters used to simulate the Couette flow with stationary parallel plates through LBM. Note that n_x and n_y are the number of lattice nodes in the x and y directions, h is the distance between the parallel plates, L is the length of the between the inlet and the outlet, τ is the relaxation time constant, $\Delta P/L$ is the pressure gradient applied and ν and ϱ are the fluid kinematic viscosity and density respectively. In this case, the fluid modeled though LBM is water at 25°C.

Parameter	Value
τ	1
L	0.05 m
h	0.01 m
$\Delta P/L$	0.0355 Pa/m
n_x	496
n_y	100
ν	1.00E-06 m^2/s
ϱ	998.29 kg/m^3

The velocity profile from the simulation matches the theory as shown in Figure 3. According to theory, the estimated permeability value of 8114.6 md obtained from LBM yields a 3.9% error. This error is attributed to discretization of space and time. Our code is therefore valid for use in porous media application.

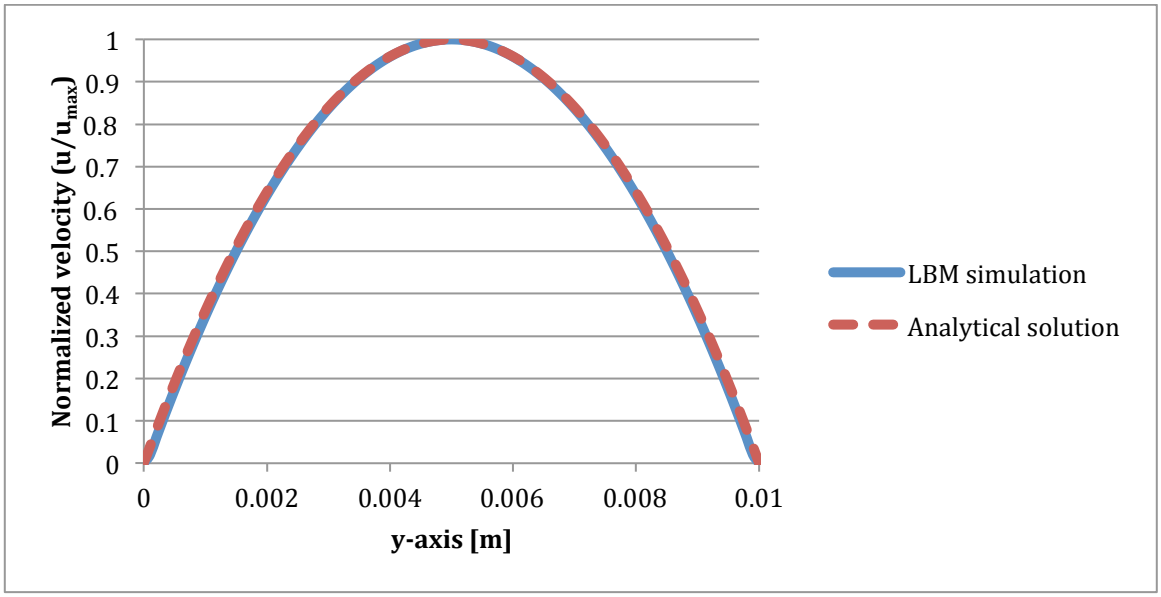

Figure 3: Velocity profile comparison between the LBM simulation and the theory for Couette flow with stationary parallel plates.

To simulate an idealized porous system, we generated a face-centered cubic system of spherical grains as shown in Figure 4 with grain resolution of 44x44x44 pixels.

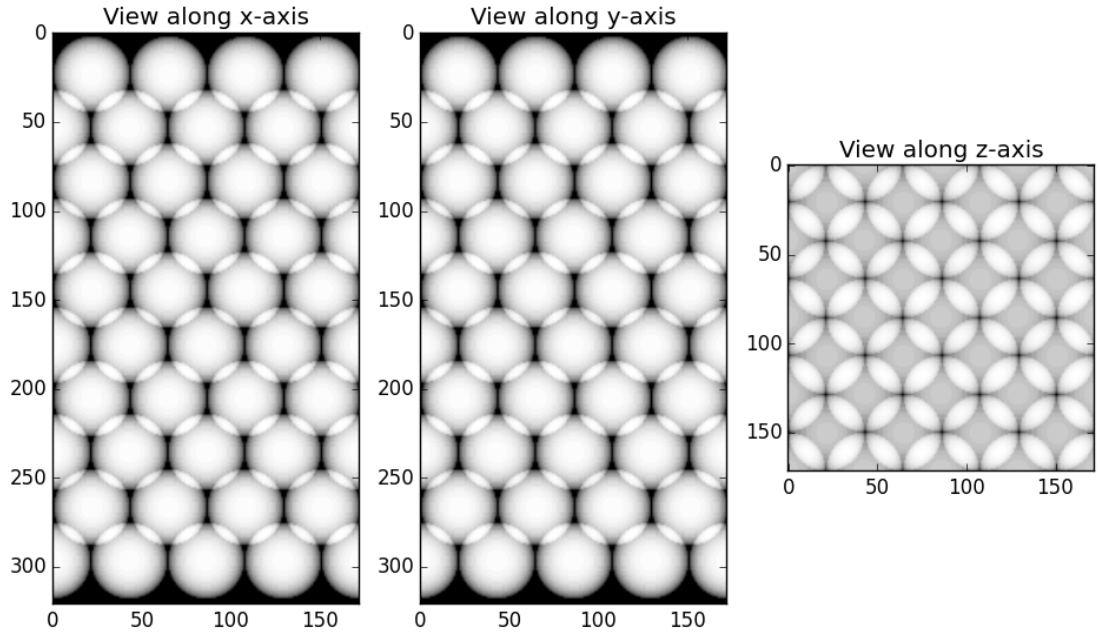

Figure 4: Generated porous medium with axes dimensions in pixels. The system dimensions are 0.004 m by 0.004 m by 0.0074 m with spherical grain diameter of 0.001 meters and porosity 29.27%. Note that the axes dimensions shown are in pixel units.

LBM was performed with the BGK collision model, D3Q19 lattice and water as the fluid. Periodic boundary conditions were applied in the x and y directions and Zou/He pressure boundary conditions were applied at the inlet and outlet to set a pressure gradient of 0.09 Pa/m along the z direction (Zou and He, 1997). Details of the inputs to the LBM simulation are shown in Table 2.

Table 2: Input parameters to simulate fluid flow in a face-centered cubic spherical grain pack through LBM. Note that n_x, n_y and n_z are the number of lattice nodes in the x, y and z directions, d is the spherical grain diameter, ϕ is the system porosity, τ is the relaxation time constant, $\Delta P/L$ is the pressure gradient applied and ν and ϱ are the fluid kinematic viscosity and density respectively. In this case, the fluid modeled though LBM is water at 25°C.

Parameter	**Value**
d	0.001 m
ϕ	29.27%
τ	1
$\Delta P/L$	0.09 Pa/m
n_x	172
n_y	172
n_z	321
ν	1.00E-06 m^2/s
ϱ	998.29 kg/m^3

At the start of the LBM simulation, the system's apparent permeability fluctuates with time as shown in Figure 5. With increasing time steps, the system approaches steady state. The simulation was run for 8997 time steps until the apparent permeability of the system stabilized to a value of 292.9 darcy. Note that the resulting Reynolds number obtained at steady state is 2.54e-5.

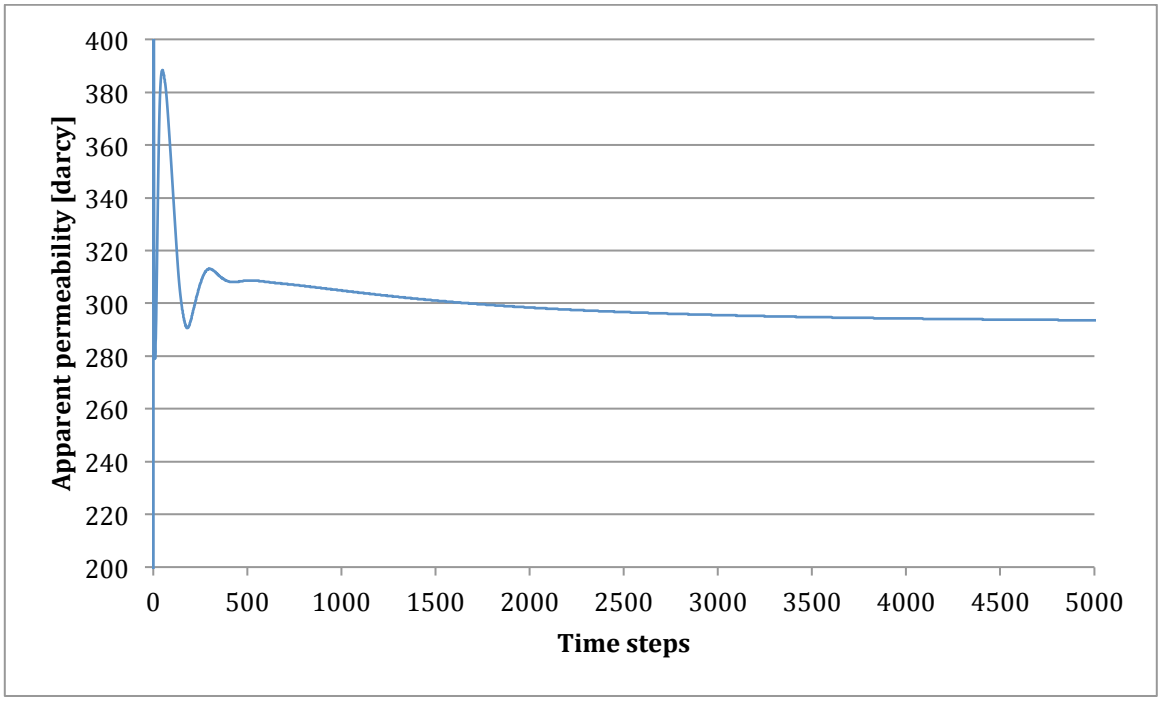

Figure 5: The apparent permeability profile throughout LBM simulation of flow of water through a face-centered cubic spherical grain pack.

According to Carman-Kozeny theory, the permeability k of a spherical grain pack is described as

$$k = \frac{\phi^3 d^2}{180(1-\phi)^2} \tag{2.5}$$

where ϕ is the system porosity and d the grain diameter (Carman, 1937). Given $\phi = 29.27\%$ and $d = 0.001$ m, the permeability of the spherical grain pack estimated from Carman-Kozeny theory is 282.2 darcy. Therefore, permeability measurement of the idealized porous medium through LBM yields a 3.80% error attributed to discretization of space and time.

STATEMENT OF PROBLEM

The single-phase permeability of a rock in one particular direction can be measured effectively through either core laboratory fluid flow experiments or

numerically through LBM. To obtain the full permeability tensor, many experiments must be performed in different flow directions. In the lab, this entails cutting core plugs in different directions and performing steady state permeability measurements for each core as done in Johnson and Hughes (1948). As each steady state permeability measurement can take up to a day to perform, obtaining the full permeability tensor in the lab can take several weeks.

Although unidirectional permeability measurements through LBM can be done in less than an hour with a supercomputer, performing many LBM simulations to calculating permeability in different directions can be computationally expensive. In addition, further complexities arise in setting up the boundary conditions for multi-directional permeability calculation with LBM as shown in Figure 6.

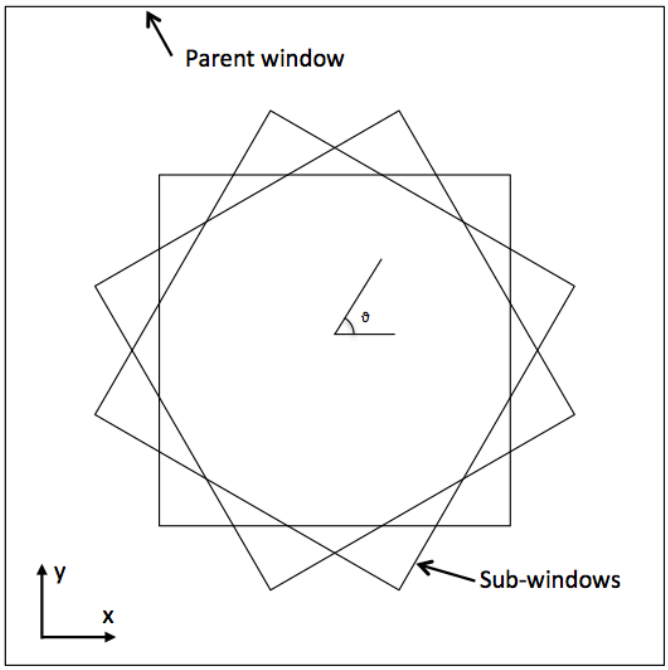

Figure 6: The required system rotation for measuring permeability through LBM in different directions. The parent window represents the initial image of the porous medium. The sub-window is subsection of the parent window rotated in the direction at which permeability would like to be measured.

The parent window represents a CT image of a core sample. LBM simulation can measure the permeability in the x and y direction using the parent window. In order to obtain the permeability in other directions, a subset of the parent window must be taken, the sub-window. Note that by specifying a sub-window, we reduce the evaluation space of our permeability measurement and may lose significant information about our core in doing so. The alternative is to obtain a CT image of core plugs taken in different directions and perform LBM permeability measurements numerically with each core image. This alternative method can take up to a week to perform. This paper presents a scheme for calculating the full permeability tensor through a combination of FMM[2] and LBM within a few hours.

METHODOLOGY

We first introduce FMM^2 and its application to assessing the directionality of the anisotropic permeability tensor. We then apply the technique to a two-dimensional elliptical grain pack and a three-dimensional spherical grain pack to validate the use of FMM^2 in an idealized porous medium. Finally, we utilize a CT image of a Berea sandstone rock to demonstrate FMM^2's effectiveness in calculate the anisotropic permeability tensor of real rocks.

The fast marching method and its application to anisotropic permeability tensor measurement

There are many flow parameters that are related to permeability. The Kozeny-Carman equation (Kozeny, 1927; Carman, 1937), for example, relates permeability to tortuosity. More specifically, the Kozeny equation describes the flow of a Newtonian fluid in a curved capillary tube of non-uniform cross-sectional area. The equation is given by

$$k = \frac{\phi^3}{\nu\tau^2(1-\phi)^2{\rho_g}^2{S_a}^2} \tag{2.6}$$

where ϕ is the porosity, ρ_g is the grain density, S_a is the specific surface area, ν is a dimensionless parameter related to the capillary tube cross-sectional shape and τ is the tortuosity. Note that tortuosity is the only parameter that varies with direction (Witt and Brauns, 1983). The ratio of the permeability in any two orthogonal directions is given by the square inverse ratio of the tortuosity (Witt and Brauns, 1983; Wong, 2003; Scholes et al., 2007; Daigle and Dugan, 2011). By obtaining the tortuosity of a core sample in various directions, one can identify the principal permeability axes and only one LBM simulation in the direction of one of the principal axes must be performed to yield the full permeability tensor.

To compute tortuosity in a rock, the path around the solid grains must be found from one point to another. FMM has been successfully used to compute the path around obstacles in robotic obstacle avoidance applications (Garido et al., 2007; Gomez at al., 2013; Valero-Gomez et al., 2013; Alvarez et al., 2014). FMM is an effective and well-developed technique and allows for calculation of tortuosity in a core sample. We use a variation on the original FMM, called FMM^2, first introduced by Garrido et al. (2007). In application to porous media, FMM^2 produces a path around the grains such that the path is at the center of the pore throats whereas FMM would yield an off-center path that tends to underestimate the tortuosity.

FMM is a numerical algorithm for solving the Eikonal equation given by

$$\|\nabla T(x,y,z)\| F(x,y,z) = 1 \tag{2.7}$$

where T is the arrival time of a monotonically advancing front and F is the speed at which the front propagates (Sethian, 1996). In obstacle avoidance application, the propagation speed of the front is set to a small value at the locations of the obstacles and to a large value in free space. The initial condition $T(x_f, y_f, z_f) = 0$ is set to initiate the wave propagation at point $[x_f, y_f, z_f]$. FMM algorithm is used to obtain the arrival time throughout the evaluation space. The path from a starting point $[x_i, y_i, z_i]$ in the evaluation space to $[x_f, y_f, z_f]$ can be obtained by finding the path of steepest descent of the level curves of T. By definition we must have

$$d\bar{r} \cdot \nabla T = 0 \tag{2.8}$$

where $\bar{r}$ is a position vector pointing to the path. The Runge-Kutta method can be used to solve Equation 2.8 and obtain the path around the obstacles from point $[x_i, y_i, z_i]$ to point $[x_f, y_f, z_f]$. Figure 7 shows an example of the wave front arrival time in a two-dimensional space with an elliptical obstacle and $[x_f, y_f] = [9,2]$.

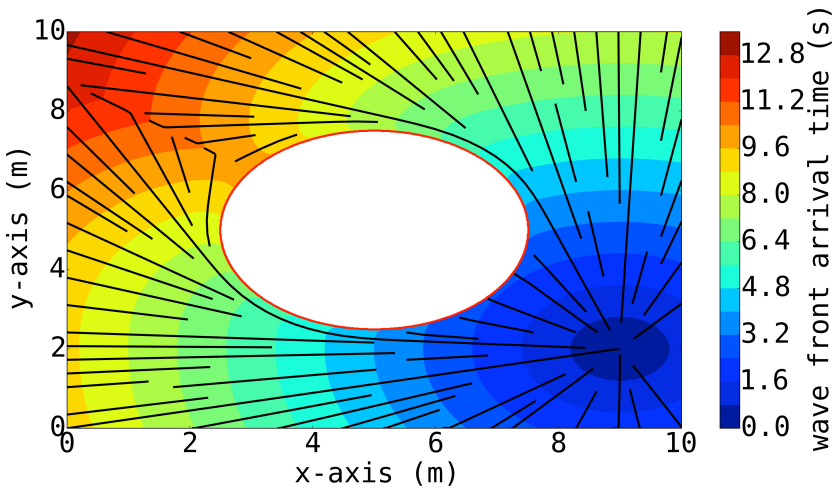

Figure 7: Contours of the wave front arrival time obtained through FMM. The wave propagation begins at the source point [x, y]=[9,2]. The path lines represent the paths to around the elliptical obstacle outlined in red to the source point. Note that the path lines are perpendicular to the contours as they represent paths of steepest descent of the level curves of the front arrival times.

Note that the front arrival time values increase the further one moves away from the end point $[x_f, y_f] = [9,2]$. In addition, the contours of the front arrival time are perpendicular to the paths around the obstacle to the end point as dictated by Equation 2.8. Once an end point is specified and the arrival time is calculated through evaluation of Equation 2.7, it is simple to obtain the path from any start point in the evaluation space. The tortuosity of the path is given by

$$\tau_{\hat{n}} = \frac{\|\bar{r}_f - \bar{r}_i\|}{\int_{\bar{r}_i}^{\bar{r}_f} \|d\bar{r}\|} \tag{2.9}$$

where $\bar{r}_f$ and $\bar{r}_i$ are the position vectors of the end and start of the path respectively. Note that $\tau_{\hat{n}}$ is the tortuosity in the direction $\hat{n} = \frac{\bar{r}_f - \bar{r}_i}{\|\bar{r}_f - \bar{r}_i\|}$.

According to Clennell (1997), hydraulic tortuosity can be calculated through analysis of the streamlines determined in numerical viscous flow simulation of porous media. For tortuosity estimation, each streamline is weighted by its contribution to the

overall flux. Parts of the pore space with the greatest streamline concentration, such as the centers of pores, are therefore weighted more strongly, hence the overall hydraulic tortuosity is most similar to the tortuosity of the streamlines passing through the centers of the pores. As shown in Figure 8, the path produced by FMM is not smooth and does not pass through the center of adjacent obstacles. In application to porous media, FMM therefore underestimates the tortuosity.

FMM^2 is more effective in estimating the tortuosity of a porous medium (Garrido et al., 2007; Clennell, 1997). As its name implies, FMM^2 involves the application of the original FMM twice. Rather than setting the front propagation speed to a small value at the obstacle and a large value in free space as done in FMM, the front propagation speed is a function of the distance from the obstacles in FMM^2 as depicted in Figure 9. FMM is first applied to find the distance from the obstacles by propagating multiple waves at the location of the obstacles. The resulting wave front arrival times are proportional to the distance from the obstacles. Another FMM is performed using distance from the obstacles as the front propagation speed. This allows the production of a path with a trajectory at the center of adjacent obstacles as shown in Figure 8. In application to porous media, FMM^2 yields the most representative effective path than FMM for hydraulic tortuosity estimation as defined by Clennell (1997). A code based on Baerentzen (2001), Hassouna et al. (2007) and van Ulitert et al (2007) is used throughout this paper for performing FMM^2. It is available online at http://www.mathworks.com/matlabcentral/fileexchange/24531-accurate-fast-marching.

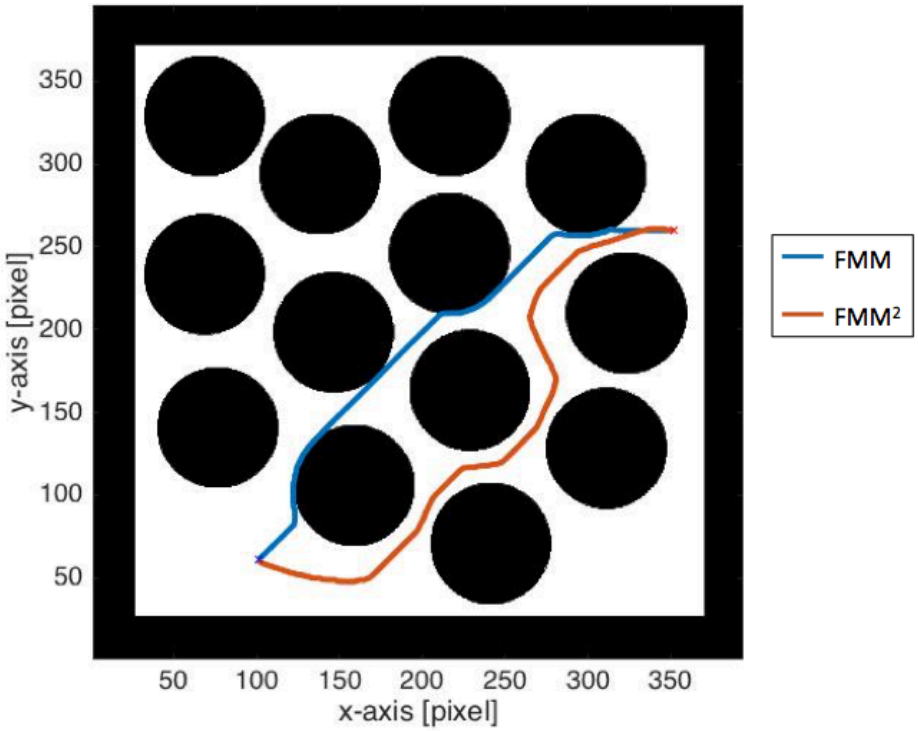

Figure 8: A comparison of the path around a random arrangement of circular obstacles obtained through FMM and FMM^2. The tortuosity of the path obtained through FMM and FFM^2 is 1.10 and 1.24 respectively.

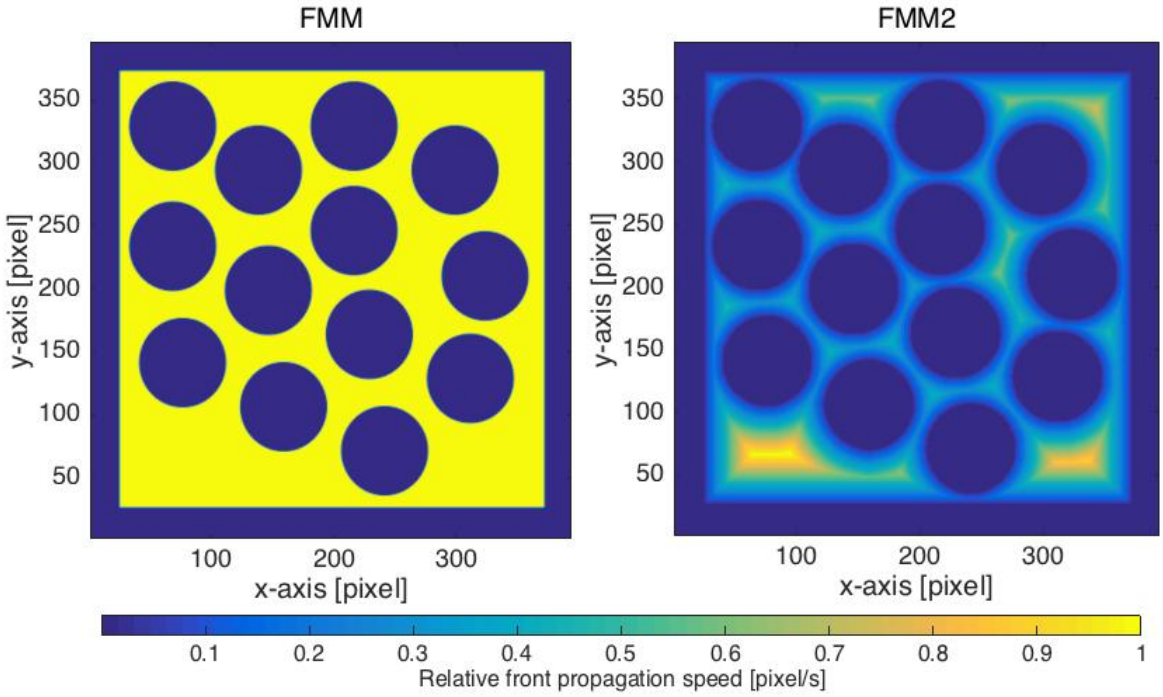

Figure 9: A comparison of the normalized wave propagation speed distribution for FMM and FMM^2 used to produce the paths shown in Figure 8.

Through FMM^2, the tortuosity of a rock can be obtained in various directions. As shown in Appendix B, the tortuosity tensor is obtained by fitting an ellipsoid to the tortuosity data. The principal tortuosity axes correspond to the principal permeability axes. Principal tortuosity values τ_1, τ_2, τ_3 are related to principal permeability values k_1, k_2, k_3 by

$$\frac{k_2}{k_1} = \left(\frac{\tau_1}{\tau_2}\right)^2, \frac{k_3}{k_1} = \left(\frac{\tau_1}{\tau_3}\right)^2. \tag{2.10}$$

The normalized principal permeability tensor is therefore given by

$$k_D/k_1 = \begin{bmatrix} 1 & 0 & 0 \\ 0 & k_2/k_1 & 0 \\ 0 & 0 & k_3/k_1 \end{bmatrix} = \begin{bmatrix} 1 & 0 & 0 \\ 0 & \left(\frac{\tau_1}{\tau_2}\right)^2 & 0 \\ 0 & 0 & \left(\frac{\tau_1}{\tau_3}\right)^2 \end{bmatrix}. \tag{2.11}$$

With one LBM simulation, k_1 can be measured and the full permeability tensor is obtained. Note that this requires the rotation of the original image of the porous medium in the direction of principle permeability axes to set the appropriate boundary conditions for fluid flow with LBM as depicted in Figure 6. To avoid image rotation, LBM can be performed in each of the orthogonal directions set by the original image of the porous medium to yield the full permeability tensor. Three examples will be presented next to test the validity of the scheme described in this section.

RESULTS

Two-dimensional FMM^2 application to anisotropic permeability calculation of idealized grain pack

The FMM^2 technique for tortuosity measurement is tested in two-dimensions by creating a rhombohedral packing of elliptical grains with an aspect ratio of 5 and 20° inclined bedding plane. The image generated is shown in Figure 10. By setting the end point $\bar{r}_f = [13,53.6]$ and the start point $\bar{r}_i = [10,0.4]$, FMM^2 is used to obtain the path around the elliptical grain shown as the blue curve in Figure 10.

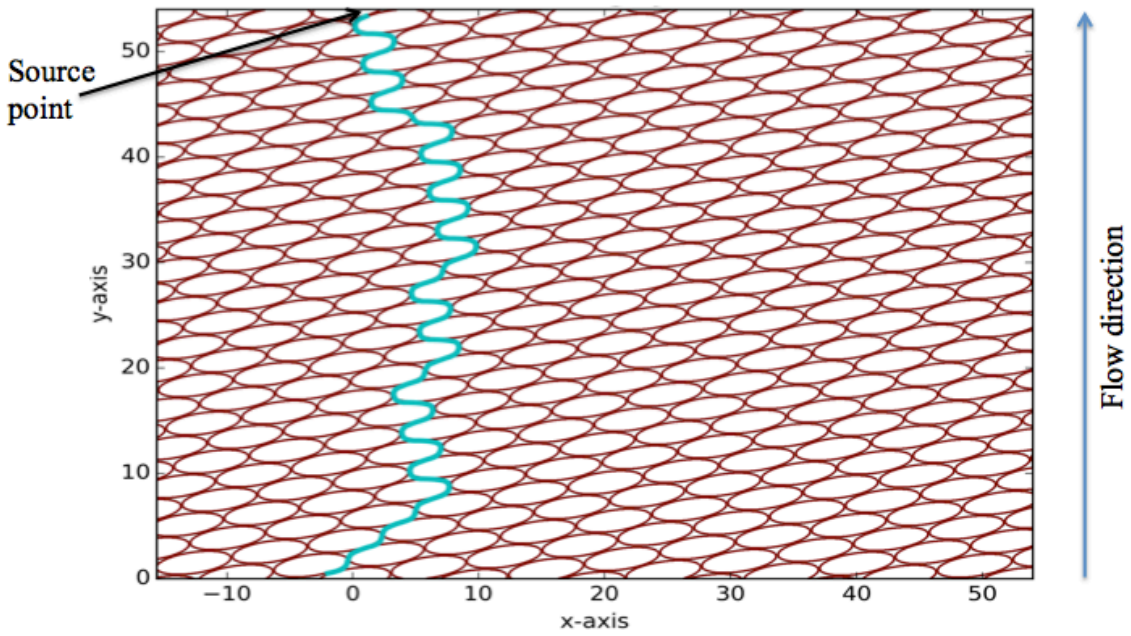

Figure 10: The path obtained through FMM2 to calculate the tortuosity in the $\hat{n} = [0.0563, 0.9984]$ direction of a rhomohedral packing of elliptical grains with aspect ratio of 5 and 20° inclined bedding plane. Axes shown are in pixel units. Tortuosity value of 1.65 was obtained.

In this case, the tortuosity in the $\hat{n} = [0.0563,0.9984]$ direction is 1.65. To obtain the tortuosity in different directions and minimize the computational time of the FMM^2 algorithm, the end point is chosen to be in the middle of the image as shown in Figure 11. By doing so, FMM^2 is performed once and the path to the end point can be calculated from multiple start points through solving Equation 2.8 with Runge-Kutta method as done in Figure 11. Directional tortuosity values can be obtained from each path line.

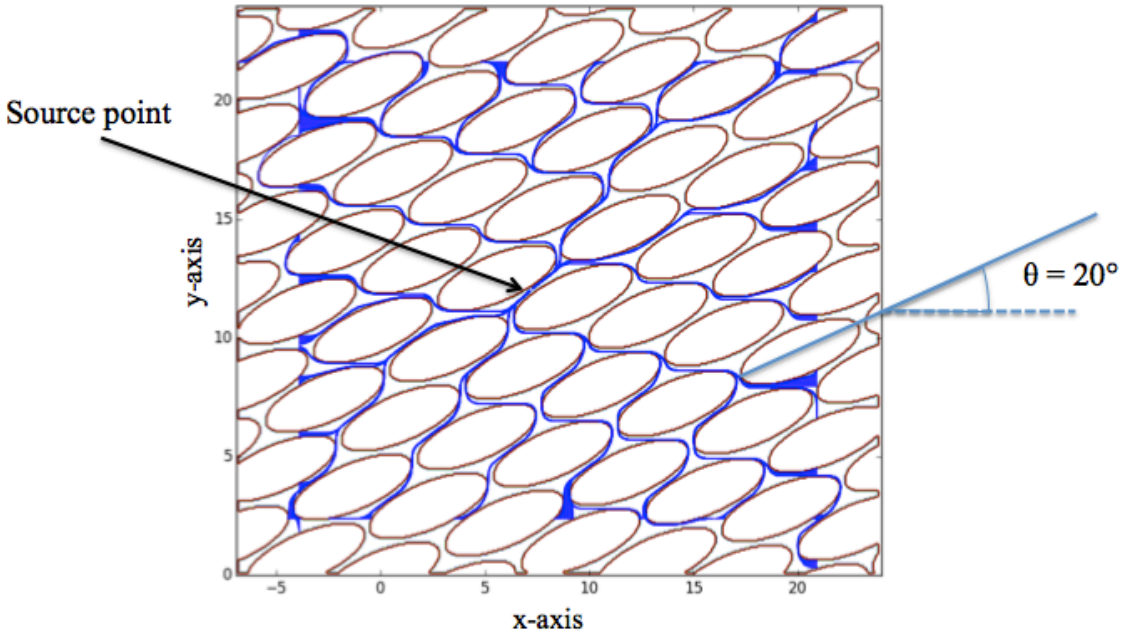

Figure 11: Multiple paths obtained from FMM[2] to obtain the tortuosity of the idealized porous medium in different directions. Axes shown are in pixel units.

An ellipse centered at the origin is fitted to the directional tortuosity data as shown in Figure 12 to identify the principal tortuosity values and directions. Appendix A describes the method used for ellipse data fitting. The data fitted ellipse equation is given by

$$\bar{x}^T A \bar{x} = \begin{bmatrix} x & y \end{bmatrix} \begin{bmatrix} 0.5034 & 0.1921 \\ 0.1921 & 0.1543 \end{bmatrix} \begin{bmatrix} x \\ y \end{bmatrix} = 1. \tag{2.12}$$

The eigenvalue and eigenvector of A indicate that the axis of minimum tortuosity is at a 23.8° angle counter-clockwise from the x-axis and the tortuosity anisotropy ratio $\tau_1/\tau_2 = 2.9$. In theory, the minimum tortuosity axis is aligned to the bedding plane. FMM accurately reproduces the direction of the bedding plane of the elliptical grain pack. The tortuosity tensor τ is obtained by rotating the diagonalized tortuosity tensor τ_D from the principal axes to the axes defined in Figure 10.

$$\tau_D = \begin{bmatrix} 3.7985 & 0 \\ 0 & 1.3036 \end{bmatrix} \tag{2.13a}$$

$$\tau = \begin{bmatrix} 1.7121 & -0.9232 \\ -0.9232 & 3.3900 \end{bmatrix} \tag{2.13b}$$

The normalized principal permeability tensor k_D is obtained from the principal tortuosity values and is given by

$$k_D/k_1 = \begin{bmatrix} 1 & 0 \\ 0 & k_2/k_1 \end{bmatrix} = \begin{bmatrix} 1 & 0 \\ 0 & \left(\frac{\tau_1}{\tau_2}\right)^2 \end{bmatrix} = \begin{bmatrix} 1 & 0 \\ 0 & 8.4902 \end{bmatrix}. \tag{2.14}$$

Note that the permeability is highly anisotropic as the porous medium consists of elliptical grains with a relatively high aspect ratio. One can calculate the normalized permeability tensor by a coordinate transformation of the principal permeability tensor.

$$k/k_1 = Vk_DV^{-1}/k_1 = \begin{bmatrix} 7.2638 & 2.7717 \\ 2.7717 & 2.2264 \end{bmatrix} \tag{2.15a}$$

$$V = \begin{bmatrix} 0.4046 & -0.9145 \\ -0.9145 & -0.4046 \end{bmatrix} \tag{2.15b}$$

V in Equation 2.15 is the transformation matrix consisting of the eigenvectors of A. To obtain the full permeability tensor, LBM can be performed in the direction of the bedding plane to find k_1.

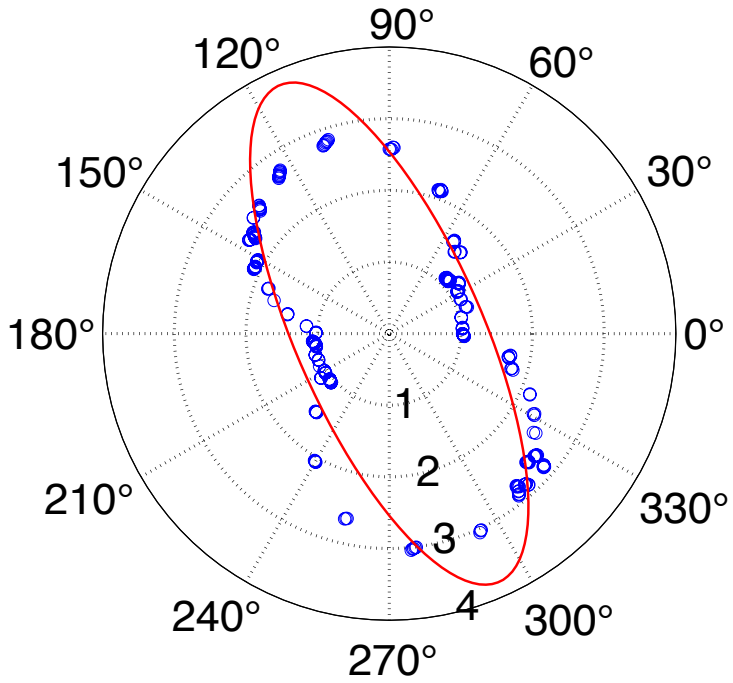

Figure 12: Rose diagram of directional tortuosity values obtained through FFM2 for rhombohedral pack of elliptical grains with aspect ratio 5 and 20° bedding plane.

Three-dimensional FMM^2 application to anisotropic permeability calculation of idealized grain pack

The validity of FMM^2 application to anisotropic permeability tensor measurement is assessed in three-dimensions. We generate a face-centered cubic system of spherical grains with grain resolution 60x60x60 pixels as shown in Figure 13.

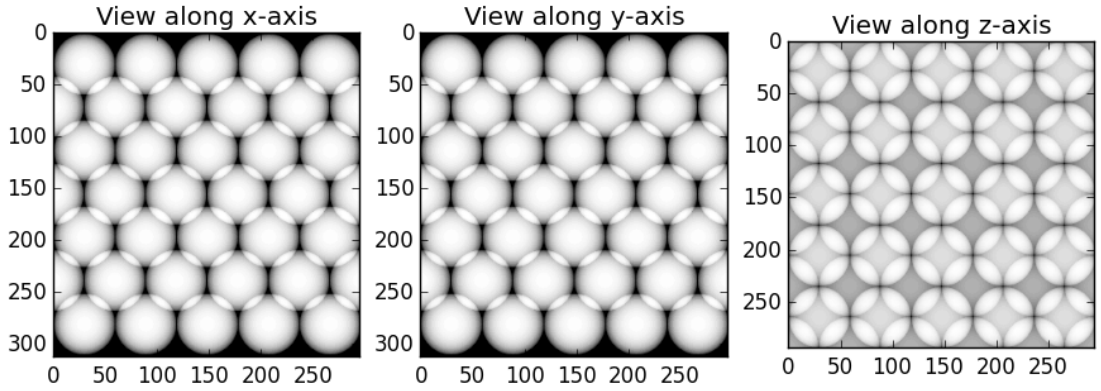

Figure 13: The generated face-centered cubic geometry of spherical grains for directional tortuosity calculation through FMM^2. Axes shown are in pixel units.

FMM^2 is performed by propagating a wave front at the center of the spherical grain pack and calculating the front arrival times. Through the Runge-Kutta method, the path from various start points is obtained as shown in Figure 14. Note that paths' trajectory converges to the center of the spherical grain pack as specified.

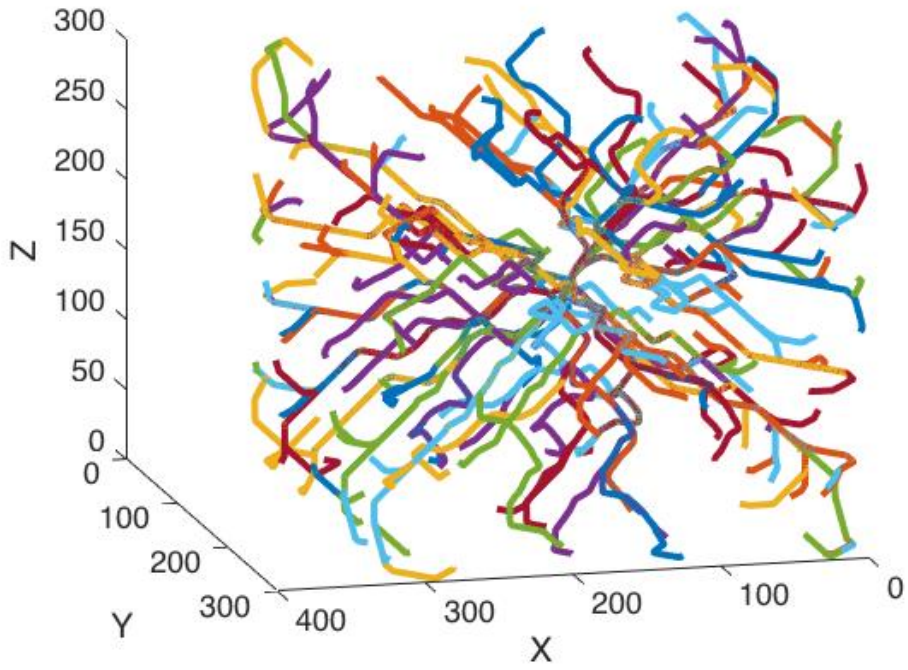

Figure 14: A collection of paths obtained through FMM^2 for the idealized porous medium shown in Figure 13. Axes shown are in pixel units.

The tortuosity at various directions is obtained from each path line by application of Equation 2.9. A histogram of the tortuosity data obtained is shown in Figure 15. Note that the tortuosity ranges between 1.10 and 1.65 with a mean value of 1.33.

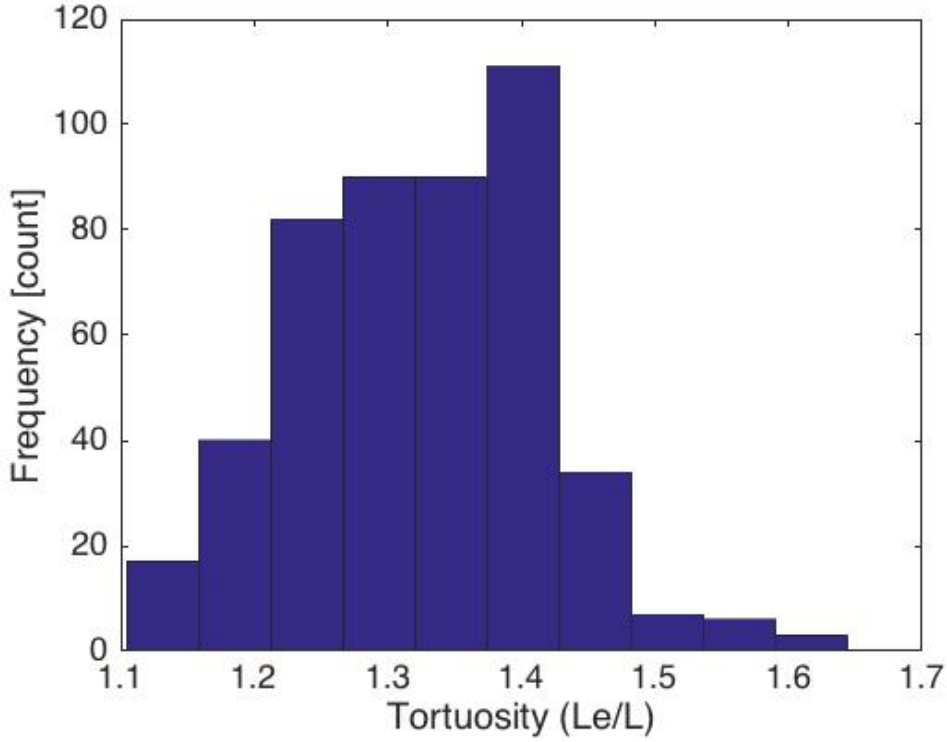

Figure 15: A histogram of the tortuosity of the idealized porous medium shown in Figure 13 found through FMM[2].

An ellipsoid centered at the origin is fitted to the directional tortuosity data through least-squares regression as discussed in Appendix B. As depicted in Figure 16, the equation of the data-fitted ellipsoid is

$$\bar{x}^T A \bar{x} = \begin{bmatrix} x & y & z \end{bmatrix} \begin{bmatrix} 0.6153 & 0.0117 & -0.0015 \\ 0.0117 & 0.5294 & -0.0011 \\ -0.0015 & -0.0011 & 0.5344 \end{bmatrix} \begin{bmatrix} x \\ y \\ z \end{bmatrix} = 1. \qquad (2.16)$$

We expect the tortuosity to be isotropic with equal principal tortuosity values as the grains are spherical and the geometry is symmetric. The eigenvalues of A estimate that the principal tortuosity values $[\tau_1, \tau_2, \tau_3] = [1.37, 1.37, 1.27]$. Although τ_1 and τ_2 are similar, τ_3 is significantly smaller in value. This is attributed to the fact that the symmetry of the geometry in the x and y directions differs from the symmetry in the z direction. The eigenvectors of A indicate that the principal tortuosity axes are given by

$$\bar{u}_1 = \begin{bmatrix} -0.1286 \\ 0.9821 \\ 0.1375 \end{bmatrix}, \bar{u}_2 = \begin{bmatrix} 0.0379 \\ -0.1337 \\ 0.9903 \end{bmatrix}, \bar{u}_3 = \begin{bmatrix} -0.9910 \\ -0.1326 \\ 0.0200 \end{bmatrix}. \quad (2.17)$$

The principal tortuosity axes are closely aligned to the axes defined by Figure 14. The normalized principal permeability tensor k_D is obtained from the principal tortuosity values through

$$k_D/k_1 = \begin{bmatrix} 1 & 0 \\ 0 & k_2/k_1 \end{bmatrix} = \begin{bmatrix} 1 & 0 & 0 \\ 0 & \left(\frac{\tau_1}{\tau_2}\right)^2 & 0 \\ 0 & 0 & \left(\frac{\tau_1}{\tau_3}\right)^2 \end{bmatrix} = \begin{bmatrix} 1 & 0 & 0 \\ 0 & 1.0127 & 0 \\ 0 & 0 & 1.1689 \end{bmatrix}. \quad (2.18)$$

Note that the permeability is relatively isotropic as expected. The normalized permeability tensor in the coordinates defined by Figure 14 are obtained through a coordinate transformation of the principal permeability tensor and represented by

$$k/k_1 = \begin{bmatrix} 1.1659 & 0.0221 & -0.0029 \\ 0.0221 & 1.0032 & -0.0021 \\ -0.0029 & -0.0021 & 1.0125 \end{bmatrix}. \quad (2.19)$$

The full permeability tensor is obtained by performing LBM in the $\bar{u}_1 = [-0.1286 \quad 0.9821 \quad 0.1375]^T$ direction.

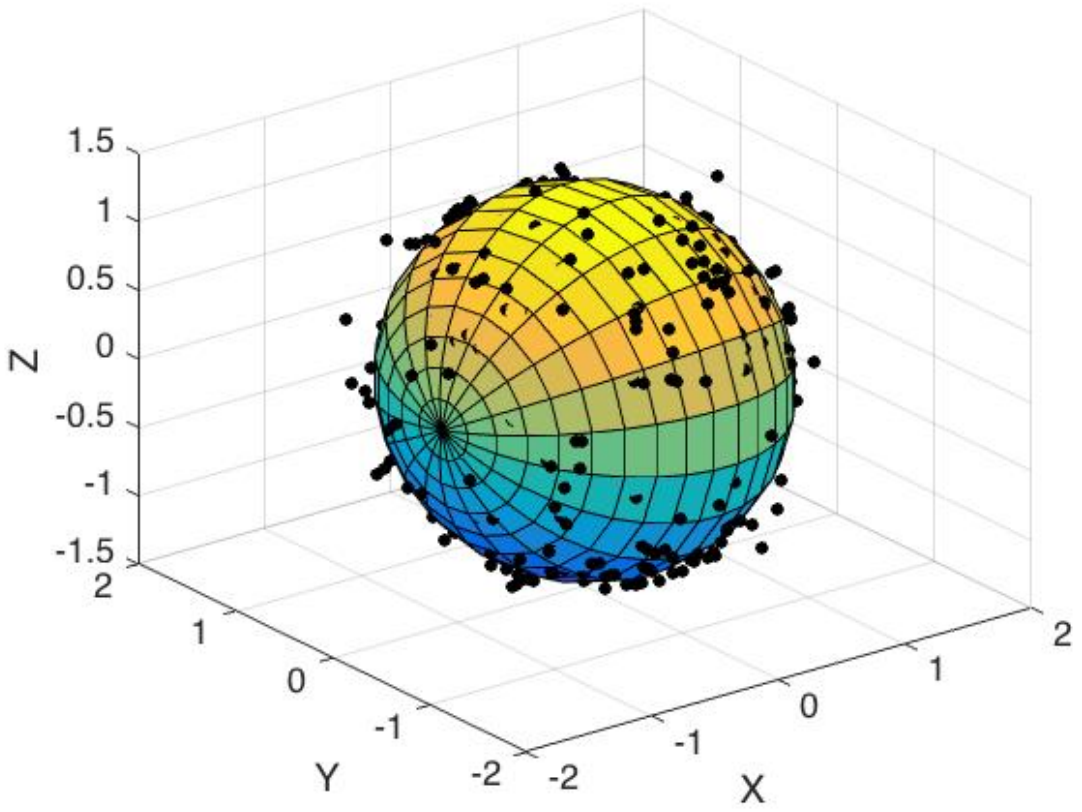

Figure 16: A rose diagram of directional tortuosity data for a face-centered spherical grain pack obtained with FMM^2 with the data-fitted ellipsoid.

FMM^2 application to anisotropic permeability calculation in real rocks

To validate the FMM^2 application to anisotropic permeability calculation in real rocks, a CT image of a sandstone core is used to represent the porous medium. Scans of core sample of Berea sandstone were obtained from the University of Texas High-Resolution X-ray CT Facility Archive.

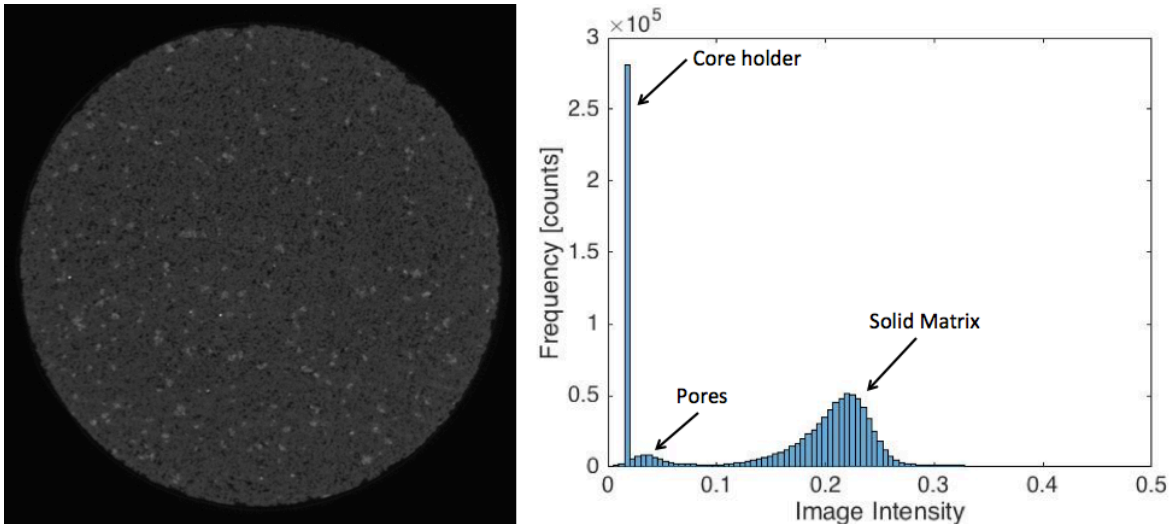

Figure 17: To the left is a CT scan image of a Berea sandstone obtained from the University of Texas High-Resolution X-ray CT Facility Archive. To the right is a histogram of the pixels in the CT scan image.

As depicted in Figure 17, the CT scan consists of multiple grayscale images of the Berea sandstone core. Shown alongside the core image is a histogram of the image pixels. Each pixel of a grayscale image has a value between 0 and 255. The image intensity normalizes the pixel value to be between 0 and 1. Most of the pixels have image intensity between 0.015 and 0.020 as indicated by the histogram in Figure 17. These pixels represent the core holder. There are two distributions evident in the histogram, one represents the pores and the other represents the solid matrix. A threshold exists between the two distributions that divides the image into a binary pore-solid matrix. ImageJ, an open source program for image analysis, is used to obtain the binary transform of the CT scan images as shown in Figure 18.

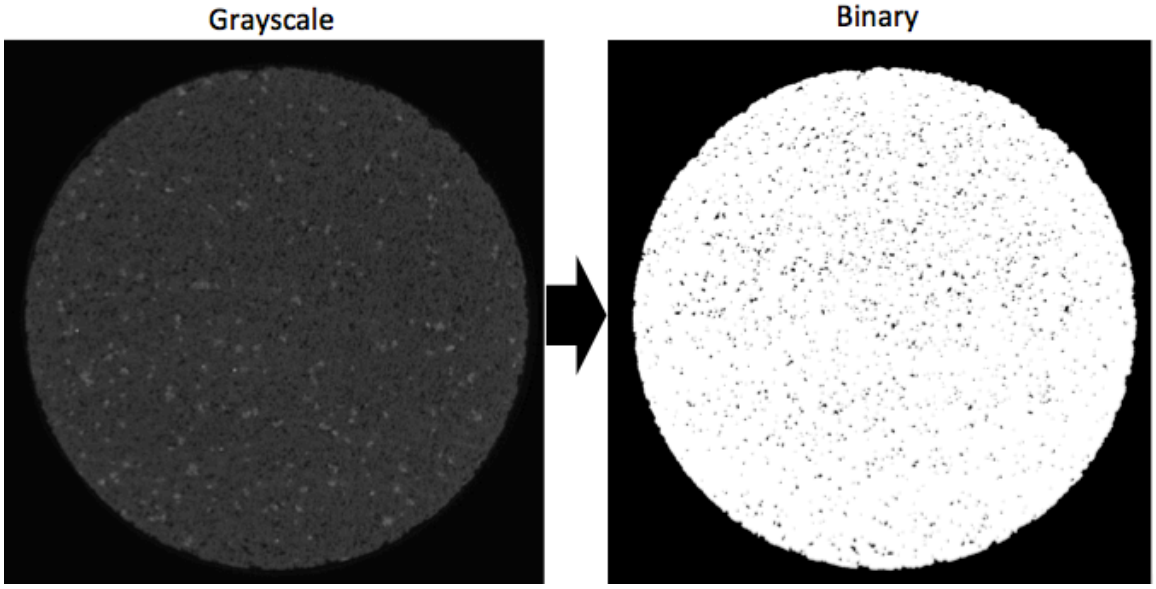

Figure 18: To the left is the original grayscale CT scan image of a Berea sandstone obtained from the University of Texas High-Resolution X-ray CT Facility Archive. To the left is the binary transform of the CT scan image obtained through the open source image analysis program ImageJ.

For simplicity, the first 550 images from the scan are used for the FMM^2 analysis. As discuss in the previous sections, the end point is chosen to be at near the center of the image to minimize computational time in obtaining the directional tortuosity data through FMM^2. Due to the complexity of the connectivity of pores in real rocks, FMM^2 is performed three times. Different end points are used in each FMM^2 application to yield a better representation of the tortuosity throughout the rock. Once the front arrival times are obtained, the Runge-Kutta method is used to find the paths from multiple start points throughout the core to each of the end points specified.

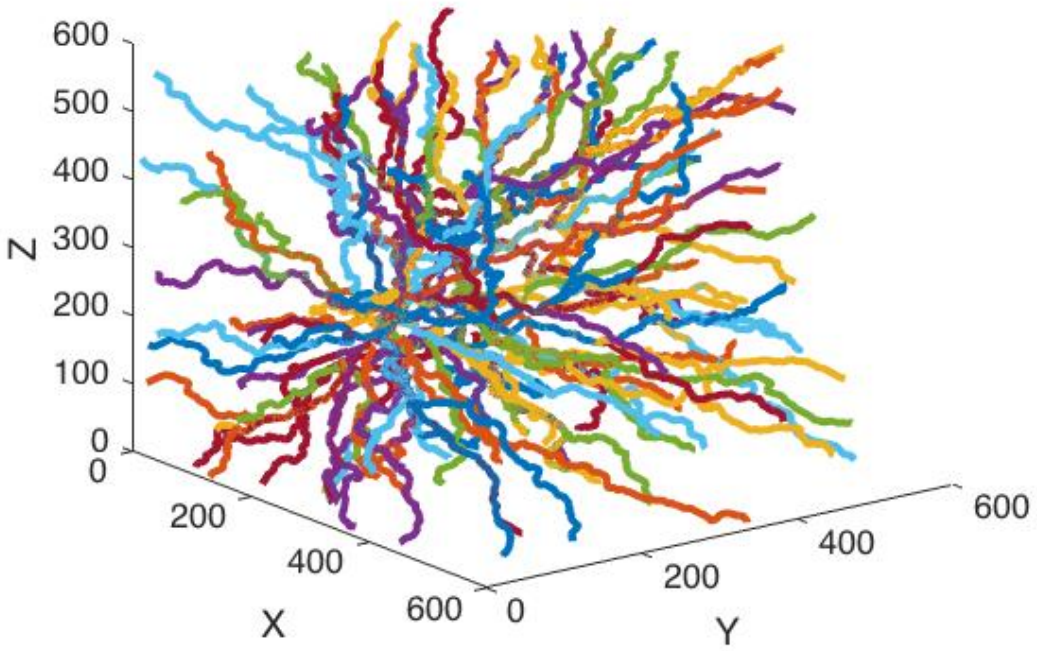

Figure 19: The paths obtained from FMM^2 to calculate directional tortuosity of a Berea sandstone core. Axes shown are in pixel units.

Figure 19 shows the collection of path lines found with FMM^2 and Runge-Kutta method. Note that all the paths end at three different point as specified. Equation 2.9 is used to obtain the directional tortuosity data from each path and an ellipsoid is fitted to the data through the algorithm described in Appendix B. Figure 20 show a plot of the directional tortuosity data and the data-fitted ellipsoid.

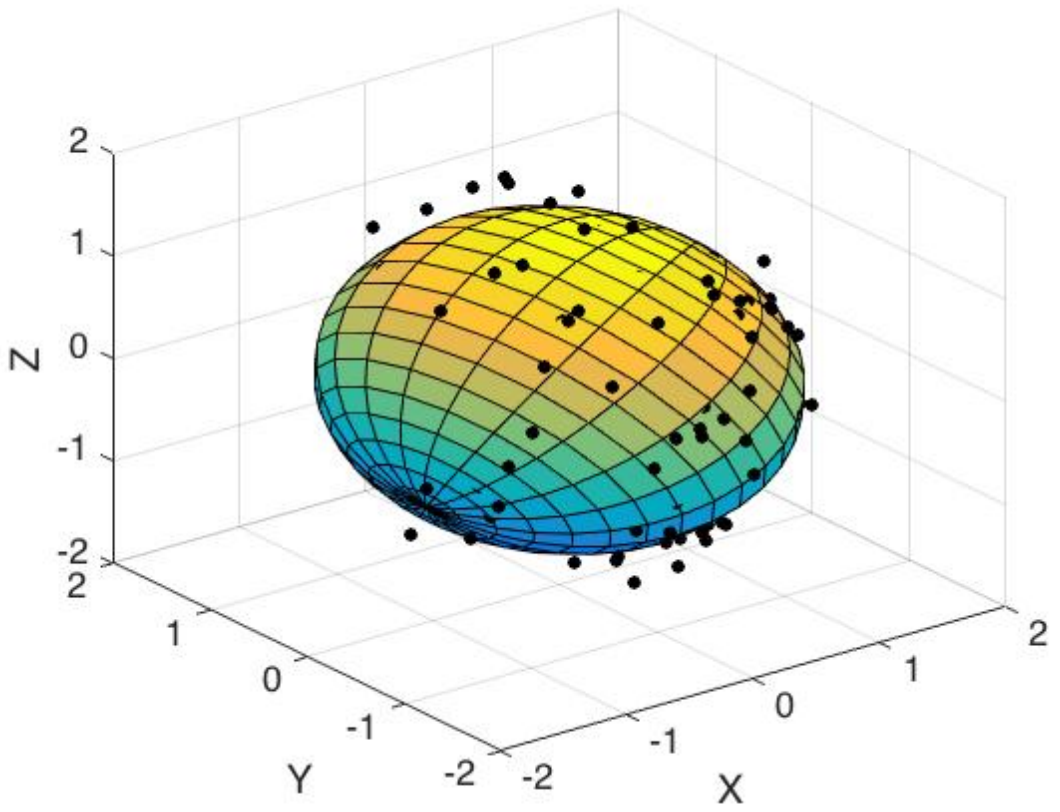

Figure 20: A rose diagram of the directional tortuosity data from the FMM[2] of the Berea sandstone core CT image with the data-fitted ellipsoid.

The equation of the data-fitted ellipsoid is

$$[x \quad y \quad z]\begin{bmatrix}0.4700 & 0.0070 & 0.0242\\ 0.0070 & 0.3640 & 0.0265\\ 0.0242 & 0.0265 & 0.4349\end{bmatrix}\begin{bmatrix}x\\ y\\ z\end{bmatrix} = \bar{x}^T A\bar{x} = 1. \tag{2.20}$$

The inverse square root of the eigenvalues of A indicate that the principal tortuosity tensor is given by

$$\tau_D = \begin{bmatrix}\tau_1 & 0 & 0\\ 0 & \tau_2 & 0\\ 0 & 0 & \tau_3\end{bmatrix} = \begin{bmatrix}1.6779 & 0 & 0\\ 0 & 1.5277 & 0\\ 0 & 0 & 1.4354\end{bmatrix}. \tag{2.21}$$

The principal tortuosity axes are defined by the eigenvectors of A and are shown in Equation 2.22.

$$\bar{u}_1 = \begin{bmatrix} 0.0090 \\ 0.9480 \\ -0.3181 \end{bmatrix}, \bar{u}_2 = \begin{bmatrix} -0.5185 \\ 0.2764 \\ 0.8092 \end{bmatrix}, \bar{u}_3 = \begin{bmatrix} 0.8550 \\ 0.1577 \\ 0.4940 \end{bmatrix} \quad (2.22)$$

The tortuosity tensor in the coordinate system described by the x-axis, y-axis and z-axis in Figure 19 is obtained through the coordinate transformation shown in Equation 2.23a-2.23b.

$$\tau = V\tau_D V^{-1} = \begin{bmatrix} 1.4603 & -0.0112 & -0.0394 \\ -0.0112 & 1.6604 & -0.0525 \\ -0.0394 & -0.0525 & 1.5204 \end{bmatrix} \quad (2.23a)$$

$$V = [\bar{u}_1 \quad \bar{u}_2 \quad \bar{u}_3] \quad (2.23b)$$

A histogram of the tortuosity measured through FMM[2] and Runge-Kutta is shown in Figure 21.

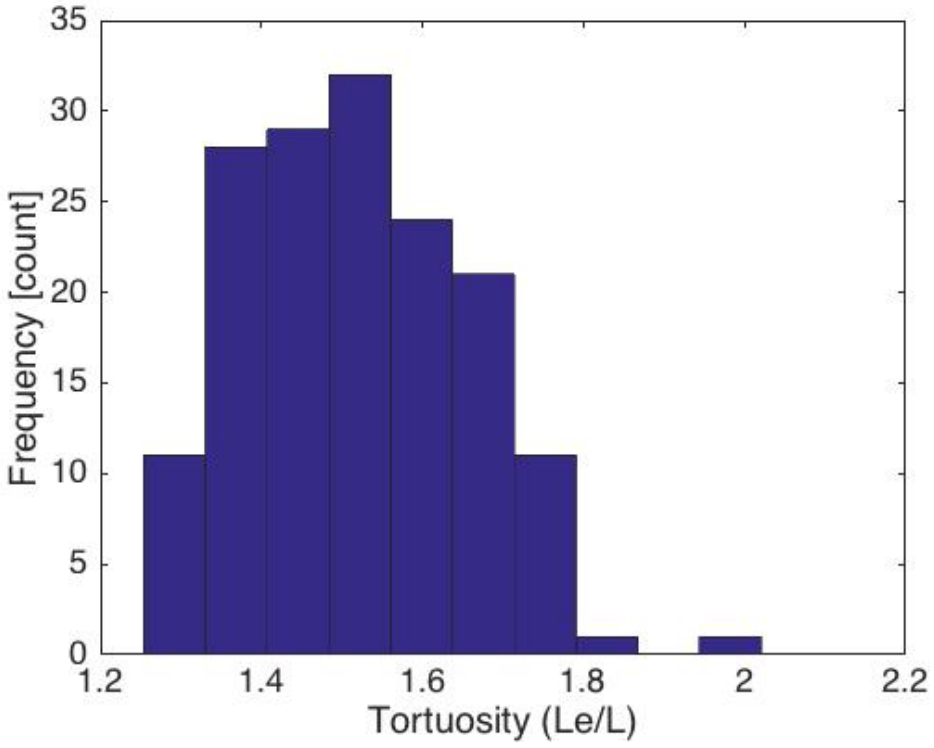

Figure 21: A histogram of the Berea sandstone tortuosity calculated through FMM[2].

Note that the tortuosity values range from 1.25 to 2.02 with a mean of 1.52. The normalized principal permeability tensor is obtained through the permeability-tortuosity anisotropy ratio relationship as shown in Equation 2.24.

$$k_D/k_1 = \begin{bmatrix} 1 & 0 & 0 \\ 0 & k_2/k_1 & 0 \\ 0 & 0 & k_3/k_1 \end{bmatrix} = \begin{bmatrix} 1 & 0 & 0 \\ 0 & \left(\frac{\tau_1}{\tau_2}\right)^2 & 0 \\ 0 & 0 & \left(\frac{\tau_1}{\tau_3}\right)^2 \end{bmatrix} = \begin{bmatrix} 1 & 0 & 0 \\ 0 & 1.2062 & 0 \\ 0 & 0 & 1.3663 \end{bmatrix} \quad (2.24)$$

As done with tortuosity, the normalized permeability tensor in the original coordinate frame described in Figure 19 is obtained through the tensor coordinate transformation

$$k/k_1 = {Vk_DV^{-1}}/{k_1} = \begin{bmatrix} 1.3232 & 0.0198 & 0.0682 \\ 0.0198 & 1.0249 & 0.0747 \\ 0.0682 & 0.0747 & 1.2244 \end{bmatrix}. \quad (2.25)$$

Finally, LBM simulation can be performed in the direction of the principal axes defined by the unit vector $\bar{u}_1$ to first estimate k_1 then obtain the full permeability tensor through scaling the matrix representation of the normalized tortuosity tensor in Equation 2.25 by k_1.

CONCLUSIONS

In real rocks, permeability is never perfectly isotropic although it is often assumed to be so in industry. To accurately characterize the flow behavior of a rock, the permeability in many directions must be obtained. We have shown that the permeability in a particular direction can be measured numerically though LBM. To assess the directionality of permeability, FMM[2] is applied. With FMM[2], the principle flow axes can be found through calculating the tortuosity of the porous medium in different directions. The square inverse of the principal tortuosity is related to the principal permeability. By a combination of FMM[2] and LBM, the full permeability tensor of a porous medium can be

estimated. Our results show that the principal flow axes were correctly identified in applying FMM^2 to a two-dimensional rhombohedral pack of elliptical grains. In three-dimensions, FMM^2 was able to recover the isotropic nature of a face-centered cubic geometry of spherical grains. Finally, the proposed scheme was validated for calculating the full permeability tensor of real rocks through its application to a three-dimensional CT scan image of a Berea sandstone core.

Chapter 3: Evaluation of near-wellbore and far-field permeability in depleted reservoirs through strain-induced permeability model

Pore pressure depletion from hydrocarbon production causes an increase in effective stress in the reservoir and can result in significant compaction. The change in stress state with depletion induces a change in permeability both in the far-field and the near well-bore region of the producing wells. Modeling the depletion induced permeability alteration is crucial in forecasting hydrocarbon production. In industry, a porosity-based permeability model is typically used which assumes changes in permeability are equal in all directions, even though the deformations are different in each direction. Wong (2003) formulated a strain-induced model that allows for anisotropic changes in permeability. This chapter presents a case study of the Tor formation in the Valhall field to compare the near-wellbore and far-field permeability alterations predicted by the isotropic permeability change models and the anisotropic model by Wong. Results show a significant difference between the models and suggest that parameters of the anisotropic Wong model can be tuned to better represent the state of the reservoir.

INTRODUCTION

An increasing number of hydrocarbon reservoirs in the world are maturing. More than 70% of the oil and gas produced today comes from secondary or tertiary production (Meng and Fuh, 2010). Hydrocarbon production from these fields has resulted in significant pore pressure depletion, causing the effective stress in the reservoirs to increase. This phenomenon can result in consolidation or failure of the rock, surface subsidence, lost circulation, pressure management issues during drilling, fluid production issues and casing failure (e.g., Sulak and Danielsen, 1988; Aadnoy, 1991; Ali et al., 1994;

Dusseault et al., 1998; Streit and Hillis, 2002; van Oort et al., 2003). A particular concern for drilling and production is the associated depletion-induced permeability alteration in the reservoir, as this will influence the production rates of existing wells and drilling fluid invasion in the subsequent wells that are drilled throughout the development program. To properly plan the development of the reservoir and accurately forecast production, models that couple the stress, deformation and permeability must be incorporated in the drilling planning programs and reservoir simulators.

A hydrocarbon reservoir experiences large stresses due to overlying rock, surrounding rock, nearby faults and tectonic forces. A portion of the external load of the total stress is supported by the pore pressure of the fluid in the reservoir. As pore pressure decreases due to hydrocarbon production, the load carried by the rock itself increases. Such load is termed the effective stress. Terzaghi (1924) modeled the concept of effective stress applicable to a fully saturated rock through

$$\sigma_{ij} = S_{ij} - \delta_{ij} P_P \tag{3.1}$$

where σ_{ij} is the effective stress, S_{ij} is the total stress, δ_{ij} is the Kronecker delta ($\delta_{ij} = 1$, if $i = j$, $\delta_{ij} = 0$ otherwise) and P_P is the pore pressure. Biot (1962) extended the definition of effective stress to partially saturated rock by introducing the Biot coefficient α to the model yielding Equation 3.2.

$$\sigma_{ij} = S_{ij} - \alpha \delta_{ij} P_P \tag{3.2}$$

Deformations in a rock are evaluated through a constitutive relation that relates the effective stress to the strains. For linear elastic material the effective stress tensor σ and strain tensor ε are related through a fourth-order invariant compliance tensor D.

$$\varepsilon = D \cdot \sigma \tag{3.3}$$

It is often useful to express Equation 3.3 in matrix notation, also called Voigt notation. Voigt notation takes advantage of the symmetry of the stress and strain tensor and

expresses the stress and strain tensor as a six-dimensional vector. Equation 3.3 in Voigt notation for isotropic materials is express as

$$\begin{Bmatrix} \varepsilon_{xx} \\ \varepsilon_{yy} \\ \varepsilon_{zz} \\ \varepsilon_{yz} \\ \varepsilon_{xz} \\ \varepsilon_{xy} \end{Bmatrix} = \begin{bmatrix} \frac{1}{E} & \frac{-\nu}{E} & \frac{-\nu}{E} & 0 & 0 & 0 \\ \frac{-\nu}{E} & \frac{1}{E} & \frac{-\nu}{E} & 0 & 0 & 0 \\ \frac{-\nu}{E} & \frac{-\nu}{E} & \frac{1}{E} & 0 & 0 & 0 \\ 0 & 0 & 0 & \frac{1+\nu}{E} & 0 & 0 \\ 0 & 0 & 0 & 0 & \frac{1+\nu}{E} & 0 \\ 0 & 0 & 0 & 0 & 0 & \frac{1+\nu}{E} \end{bmatrix} \begin{Bmatrix} \sigma_{xx} \\ \sigma_{yy} \\ \sigma_{zz} \\ \sigma_{yz} \\ \sigma_{xz} \\ \sigma_{xy} \end{Bmatrix} \tag{3.4}$$

where ν and E are material constants termed Poisson's ratio and Young's modulus respectively. Note that linear elasticity assumes infinitesimal strains or small deformations. If strains observed in the reservoir are large and finite, the nonlinear theory of elasticity must be used.

Various models exist for coupling the stress, strain and permeability. The simplest models relate changes in effective stress relative to some reference value directly to changes in permeability (e.g., Zhai and Sharma, 2005). More complex models invoke the porosity-permeability relationship in accounting for changes in porosity, tortuosity and surface area through evaluation of the volumetric strain. Note that in the linear theory of elasticity, the volumetric strain ε_V is expressed as the summation of the normal strains.

$$\varepsilon_V = \frac{\Delta V}{V} = (1+\varepsilon_{11})(1+\varepsilon_{22})(1+\varepsilon_{33}) - 1 \approx \varepsilon_{11} + \varepsilon_{22} + \varepsilon_{33} \tag{3.5}$$

If the solid grains are assumed to be incompressible, the volumetric strain is related to the change in porosity through

$$\varepsilon_V = \frac{\phi - \phi_o}{1 - \phi} \tag{3.6}$$

where ϕ and ϕ_o are the final and initial porosity respectively. Through application of Kozeny-Poiseuille correlation and Equation 3.6 the effects of deformation on permeability can be expressed as

$$\frac{k}{k_i} = \frac{(1 + \varepsilon_V/\phi_o)^3}{1 + \varepsilon_V} \tag{3.7}$$

where k_i and k are the initial and final permeability respectively (e.g., Tortike and Farouk, 1993; Wang and Xue, 2002). Note that Equation 3.7 accounts for changes in porosity and specific surface area with deformation. A similar expression, based on the Carmen-Kozeny theory (Carman, 1937) is written as

$$\frac{k}{k_o} = \left(\frac{\phi}{\phi_o}\right)^3 \left(\frac{1-\phi_o}{1-\phi}\right)^2. \tag{3.8}$$

In industry, an empirical porosity-permeability correlation is often used to relate changes in porosity to changes in permeability. Cores from a reservoir are collected and the permeability and porosity of the cores are measured to evaluate the heterogeneity in the reservoir. The porosity and permeability are then plotted on a semi-log plot and a line is fitted to the data such that $k = \eta e^{\beta\phi}$ where η and β are the data fitting parameters obtained through least-square regression analysis. We can therefore model the change in permeability through

$$\frac{k}{k_o} = e^{\beta(\phi-\phi_o)}. \tag{3.9}$$

STATEMENT OF PROBLEM

The permeability changes of a porous medium subject to deformation are usually determine through a state variable that accounts for the volumetric change, such as porosity, void ratio or volumetric strain. Such state variables are scalar and hence yield an isotropic change in permeability, i.e. assume the change in permeability is equal in all directions, even through the deformations are different in each direction.

Strain deformation results in both volume dilation and grain rearrangement, which affects both cross-sectional area of flow and tortuosity. Wong (2003) formulated a model based on the Carman-Kozeny equation to attribute changes in flow area and path to changes in permeability and relates them to the strains. Specifically, the model relates changes in hydraulic flow parameters to principle strains rather than volumetric strains. The Wong model therefore allows for anisotropic changes in permeability and hence produces a more realistic representation of deformation-induced permeability alteration.

This paper evaluates the changes in near-wellbore and far-field permeability of a vertical producing well in the Tor formation of the Valhall field with depletion. In comparing the predicted permeability changes through the anisotropic Wong permeability model and the isotropic permeability alternation model, we assess the potential error associated with isotropic permeability change assumption commonly used in industry.

MODEL DEVELOPMENT

The strain-induced Wong permeability model

Through the Hamilton-Cayley equation (Mase, 1970), it can be shown that the principal permeability tensor is a function of the strains (Wong, 2003). Assuming infinitesimal strains, the permeability can be expressed as a linear combination of the elements of the strain tensor. In tensor notation, this can be expressed as

$$k = C \cdot \varepsilon \tag{3.10}$$

where C is a fourth-order tensor. In Voigt notation, Equation 3.10 can be expressed as

$$\begin{Bmatrix} k_{11} \\ k_{22} \\ k_{33} \\ k_{23} \\ k_{13} \\ k_{12} \end{Bmatrix} = \begin{bmatrix} c_{11} & c_{12} & c_{13} & c_{14} & c_{15} & c_{16} \\ c_{21} & c_{22} & c_{23} & c_{24} & c_{25} & c_{26} \\ c_{31} & c_{32} & c_{33} & c_{34} & c_{35} & c_{36} \\ c_{41} & c_{42} & c_{43} & c_{44} & c_{45} & c_{46} \\ c_{51} & c_{52} & c_{53} & c_{54} & c_{55} & c_{56} \\ c_{61} & c_{62} & c_{63} & c_{64} & c_{65} & c_{66} \end{bmatrix} \begin{Bmatrix} \varepsilon_{11} \\ \varepsilon_{22} \\ \varepsilon_{33} \\ \varepsilon_{23} \\ \varepsilon_{13} \\ \varepsilon_{12} \end{Bmatrix}. \tag{3.11}$$

Equation 3.11 is the generalized relation for the Wong model. Wong (2003) showed that permeability and strains can be expressed in terms of their principal values due to the property of symmetric square matrices. In the isotropic case, the Wong model reduces to

$$\begin{bmatrix} k_1 \\ k_2 \\ k_3 \end{bmatrix} = \begin{bmatrix} k_{1i} \\ k_{2i} \\ k_{3i} \end{bmatrix} + \begin{bmatrix} a' & b' & b' \\ b' & a' & b' \\ b' & b' & a' \end{bmatrix} \begin{bmatrix} \varepsilon_1 \\ \varepsilon_2 \\ \varepsilon_3 \end{bmatrix} \tag{3.12}$$

where k_i is the final permeability, k_{i0} is the initial permeability, a' and b' are invariant model parameters and ε_i is the strain expressed in the principal axes $i = 1,2,3$. The constant a' characterizes the changes in permeability induced by normal (volumetric) deformation, while the $b' - a'$ characterizes the change in permeability induced by shear deformation. Equation 3.12 assumes that the principal strain axes and the principal permeability axes are aligned. Note that since strain is dimensionless, a' and b' have the same units as permeability. In order to render the material constants associated with the Wong model dimensionless, we rewrite the Wong model as

$$\begin{bmatrix} k_1/k_{1i} \\ k_2/k_{1i} \\ k_3/k_{1i} \end{bmatrix} = \begin{bmatrix} 1 \\ k_{2i}/k_{1i} \\ k_{3i}/k_{1i} \end{bmatrix} + \begin{bmatrix} a & b & b \\ b & a & b \\ b & b & a \end{bmatrix} \begin{bmatrix} \varepsilon_1 \\ \varepsilon_2 \\ \varepsilon_3 \end{bmatrix} \tag{3.13}$$

where $a = a'/k_{1i}$ and $b = b'/k_{1i}$. Figure 22 shows the various model parameters obtained from experiments conducted by Wong (2003). The experiments entail the measurement of permeability different directions of idealized packing of spheres, oil sands and locked sands under different loading conditions.

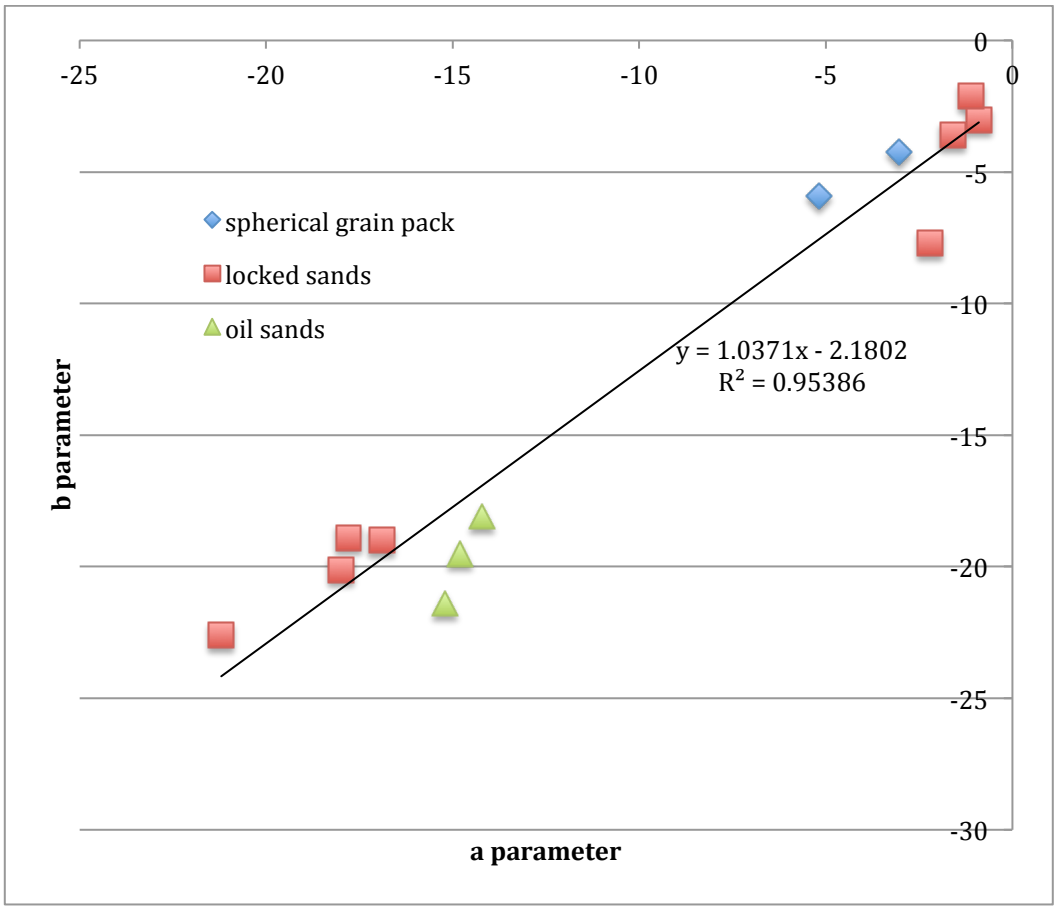

Figure 22: The a and b parameters of the strain-induced permeability Wong model obtained from various experiments presented in Wong 2003.

The Wong model parameters a and b are negative due to our sign convention of defining compressive stress as positive. Generally, a is larger than b and $a - b \approx 2.2$.

Note that by setting $a = b$ and applying Equation 3.6 for an isotropic initial permeability, we recover an isotropic permeability change model that only accounts for volumetric deformation.

$$\frac{k}{k_o} = 1 + a\varepsilon_V = 1 + a\frac{\phi - \phi_o}{1 - \phi} \tag{3.14}$$

Throughout this paper, we will refer to the isotropic permeability alteration model as the isotropic Wong model ($a = b$) and the anisotropic permeability alteration model as the anisotropic Wong model ($a \neq b$).

Stress distribution around a wellbore

The Kirsch equations describe the stress around a circular cavity of a linear isotropic material subject to external loading (Kirsch, 1898). Aadnoy et al. (1987) successfully applied this set of equations to calculate the stress around a deviated wellbore and assessed the fracture pressure and collapse pressure through incorporating various rock failure criteria. The Kirsch equations for a vertical wellbore are

$$S_r = \frac{1}{2}(S_{hmax} + S_{hmin})\left(1 - \frac{a^2}{r^2}\right) + \frac{1}{2}(S_{hmax} - S_{hmin})\left(1 + 3\frac{a^4}{r^4} - 4\frac{a^2}{r^2}\right)\cos 2\theta + \frac{a^2}{r^2}p_w \tag{3.15a}$$

$$S_\theta = \frac{1}{2}(S_{hmax} + S_{hmin})\left(1 + \frac{a^2}{r^2}\right) - \frac{1}{2}(S_{hmax} - S_{hmin})\left(1 + 3\frac{a^4}{r^4}\right)\cos 2\theta - \frac{a^2}{r^2}p_w \tag{3.15b}$$

$$S_z = S_v - 2\nu(S_{hmax} - S_{hmin})\frac{a^2}{r^2}\cos 2\theta \tag{3.15c}$$

$$S_{r\theta} = \frac{1}{2}(S_{hmax} - S_{hmin})\sin 2\theta\left(1 - 3\frac{a^4}{r^4} + 2\frac{a^2}{r^2}\right) \tag{3.15d}$$

$$S_{rz} = S_{\theta z} = 0 \tag{3.15e}$$

where S_{ij} is the total stress in cylindrical coordinates, a is the radius of the wellbore, S_{hmax} and S_{hmin} are the maximum and minimum horizontal stresses respectively, S_v is the overburden stress, ν is the Poisson ratio, r and θ are the radial and azimuthal coordinates of point of interest respectively and p_w is the wellbore pressure. Note that Equation 3.2 can be used to evaluate the effective stress.

Stress path determination

Pore pressure depletion does not only increase the effective stress in the reservoir, but it also changes the far-field stresses. Although the overburden stress is commonly assumed to be constant, the horizontal stresses change significantly with depletion. The stress path A is defined as the ratio of the change in horizontal stresses to the change in pore pressure and is expressed as

$$A = \frac{\Delta S_h}{\Delta P_p} = \alpha \frac{1 - 2\nu}{1 - \nu} \tag{3.16}$$

for linear, isotropic homogenous reservoir of infinite extent (Addis, 1997; Hillis, 2001; Engelder, 1994). Note that Equation 3.16 is assumed that the magnitude of the changes in the minimum and maximum horizontal stresses with depletion are the same. According to Segall and Fitzgeral (1998), Equation 3.16 is applicable when the ratio of the reservoir lateral extent to its thickness is 10:1.

CASE STUDY: TOR FORMATION IN VALHALL

The Valhall field is a chalk reservoir located in the North Sea. It consists of two late Cretaceous oil-bearing formations: the Tor formation and the underlying Hod formation. In this paper, we will use the Tor formation as a case study to evaluate the depletion-induced permeability alteration through the Wong model. Figure shows a stratigraphic column of the Valhall reservoir.

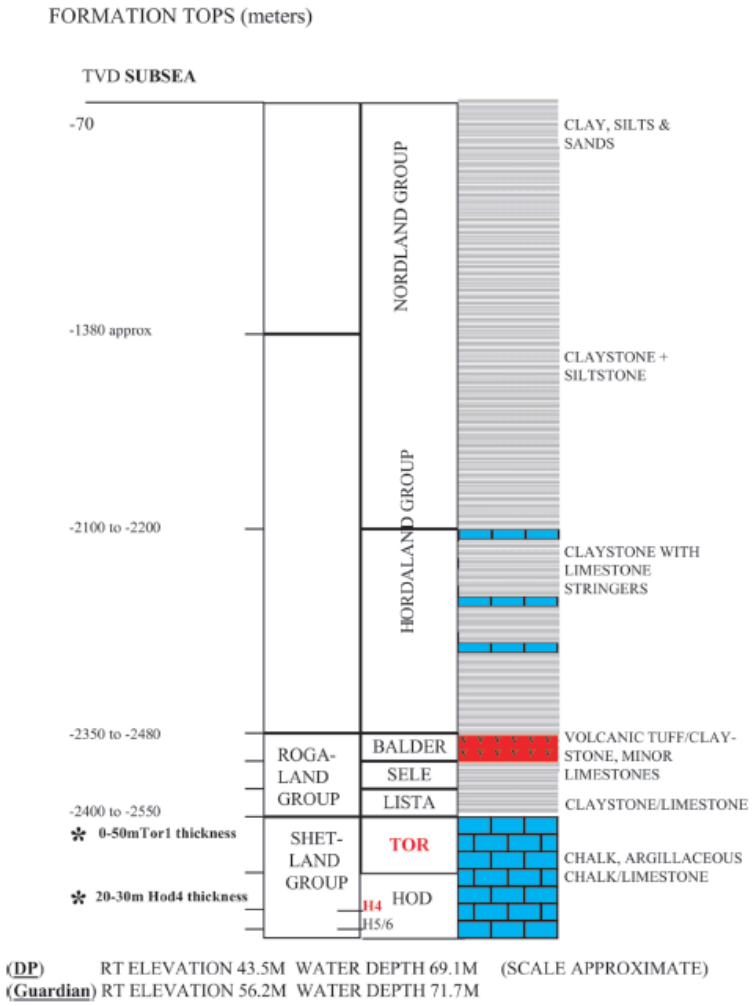

Figure 23: Stratigraphic column of the Valhall field (Kristiansen, 2007).

The Tor formation has an average thickness of 30 m and is at a total vertical depth of 2400 m subsea (York et al., 1992). Figure 24 shows a map of the Valhall field and indicates that the lateral extent of the Tor formation is 3 km on average.

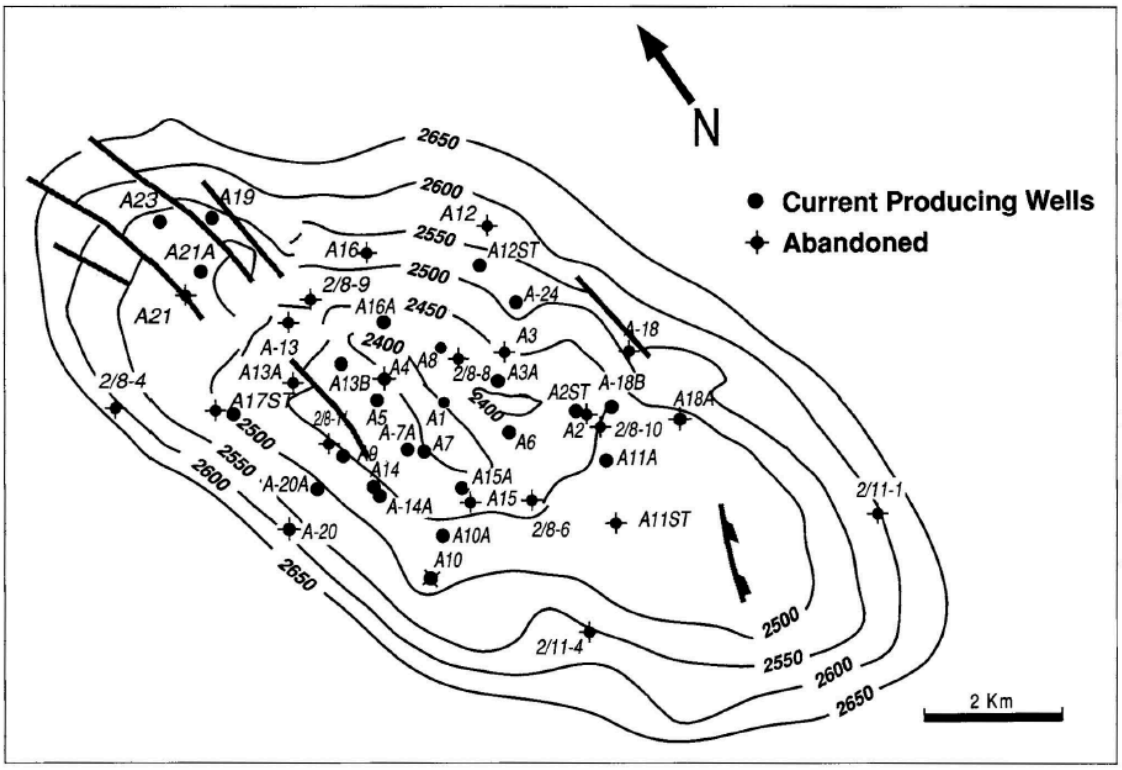

Figure 24: Contour map of the total vertical depth subsea of top of the Tor formation in the Valhall field (York et al., 1992).

Primary porosity for the Tor formation varies between 36% and 50% (Chan, 2005). Matrix permeability values measured from Valhall formation core analysis are low and rarely exceed 10 md (Munns, 1985). The porosity-permeability relationship obtained from core analysis is shown in Figure 25 (Munns, 1985). Note that Tor field label shown in the Figure 25 represents another field and thus does not represent data from the Tor formation of the Valhall field.

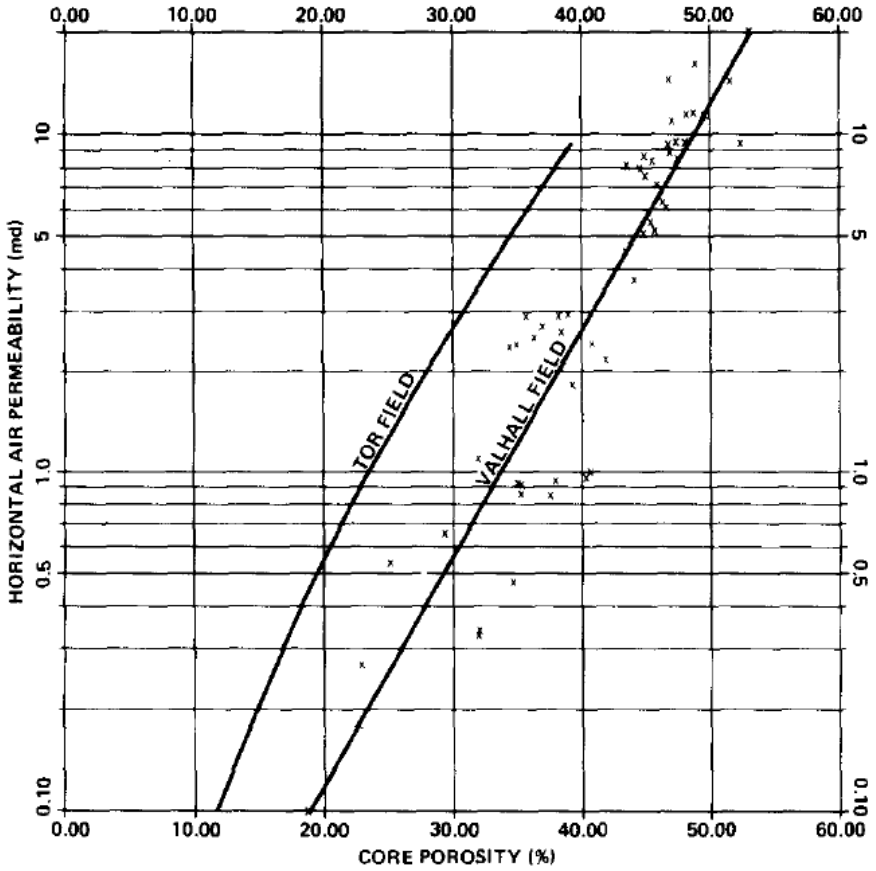

Figure 25: Semi-log plot of porosity versus permeability of cores obtained from the Tor formation in the Valhall field (Munns, 1984).

The data is fitted to an exponential function and results in the following empirical porosity-permeability relationship.

$$k = 0.0052e^{15.627\phi} \tag{3.17}$$

The permeability change can therefore be expressed through

$$\frac{k}{k_o} = e^{15.627(\phi-\phi_o)} \tag{3.18}$$

where $\phi_o = 0.41$ (Chan, 2005). A plot of Equation 3.18 is shown in Figure 26.

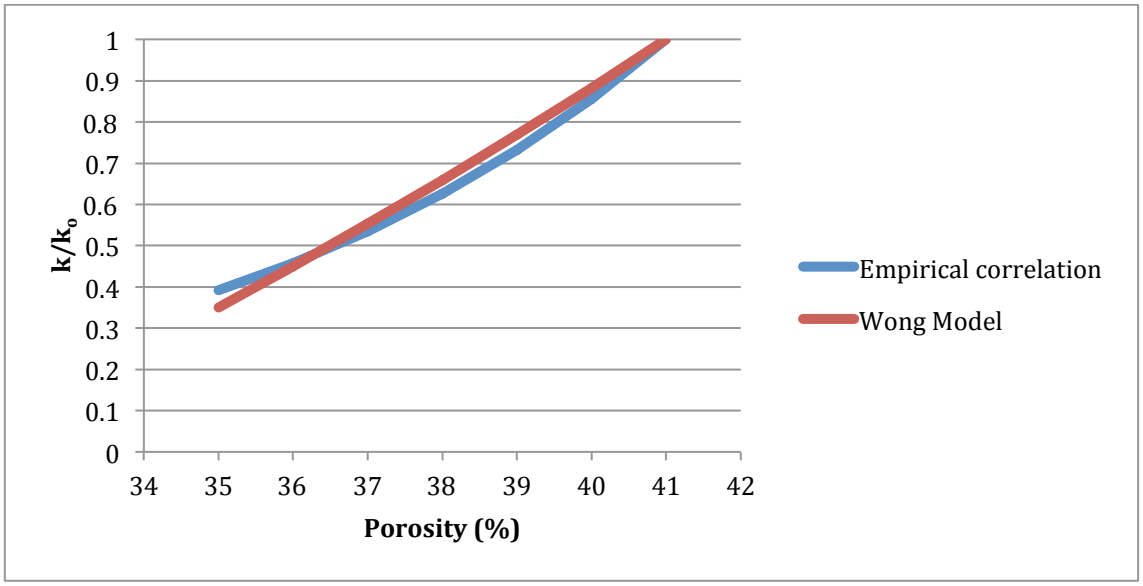

Figure 26: Permeability change as a function of porosity, given 41% initial porosity as estimated by Chan 2005, obtained from the empirical correlation of Equation (3.18) and the Wong model described by Equation (3.14) with a=-7.04.

Equation 3.14 is fitted to the empirical correlation in order to obtain an estimate of the Wong model parameters. Through least-squares regression analysis, we obtain the value $a = -7.04$. Note that the value of b for the Wong model can now be tuned to fit permeability data observed in the field or production history. In this paper, we will compare the change in permeability obtained when $a = b = -7.04$ and when $a = -5.94, b = -8.14$ (such that $\frac{b+a}{2} = -7.04$ in both cases). In doing so, we can assess the potential error attributed to the isotropic permeability change commonly used in industry. Ideally one would measure the values of a and b experimentally as done in Wong (2003). As we do not have access to strain-permeability data for chalk, we simply assume that the value of b relative to a follows the general trend shown in Figure 22 mostly representative of sandstone.

Hydrocarbon production in the Valhall field started in October 1982 and the Tor formation has undergone significant pore pressure depletion since then. The initial reservoir pressure is 42.2 MPa and within a span of 14 years the reservoir pressure dropped by more than half its initial value. Figure 27 shows the approximate pore pressure profile (Zoback and Zinke, 2002).

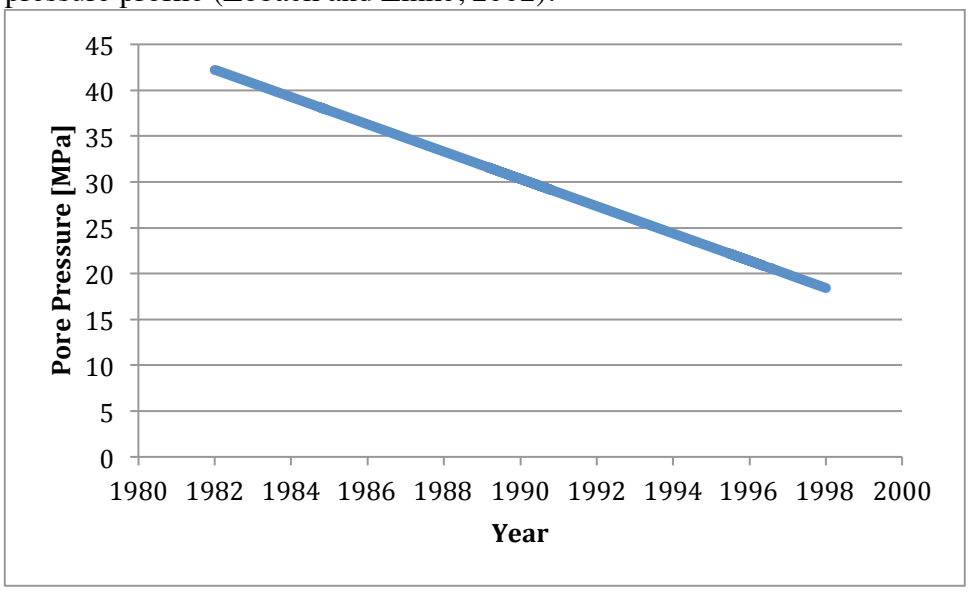

Figure 27: Pore pressure depletion history of the Tor formation in Valhall field (Zoback and Zinke, 2002).

The overburden stress and initial minimum horizontal stress are estimate to be 49.2 MPa and 45.4 MPa respectively (Zoback and Zinke, 2002). Figure 28 shows the change in horizontal stress with depletion for the Tor reservoir obtained from Zoback and Zinke (2002).

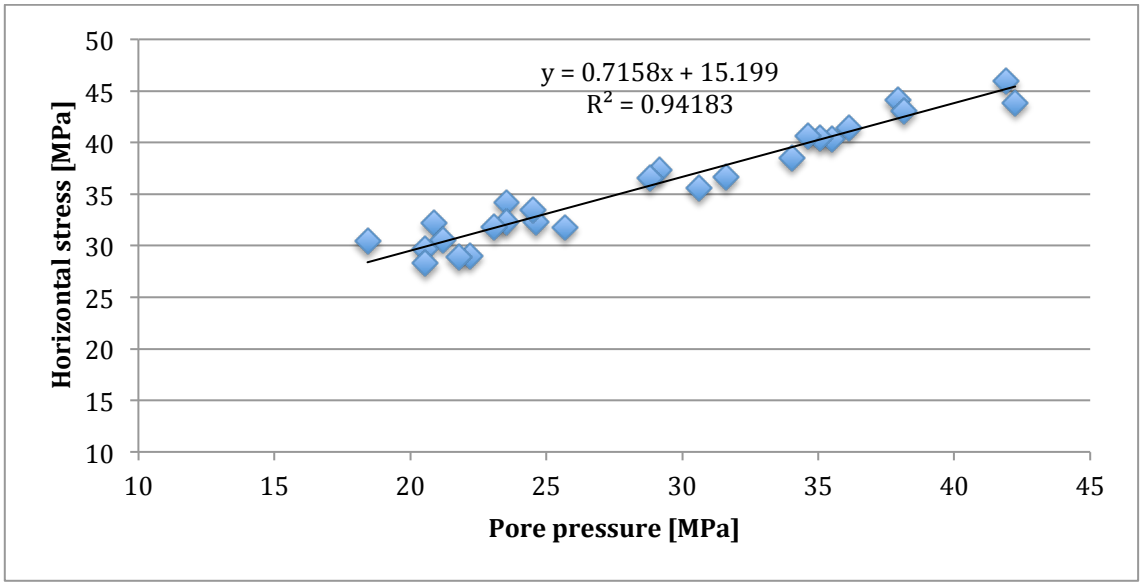

Figure 28: Pore pressure versus minimum horizontal stress of the Tor formation in Valhall field (Zoback and Zinke, 2002).

Note that the relationship between the horizontal stress and the pore pressure is approximately linear. As discussed in Zoback and Zinke (2002), the Tor reservoir was in a normal faulting stress state initially. The initial maximum horizontal stress will therefore be assumed to be the average of the minimum horizontal stress and the overburden stress. Although the ratio of the reservoir lateral extent to its thickness is larger than 10:1, Equation 3.16 fits the data well and given our data A=0.72. Assuming a Biot coefficient $\alpha = 1$, Equation BLAH yields a Poisson ratio $\nu = 0.22$. According to Kristiensen (1998), the Poisson's ratio of formations in the Valhall field varies between 0.16 and 0.43. The Poisson ratio obtained from Equation 3.16 is therefore a reasonable value. Based on Young's modulus values used in Patillo (1996) for simulating reservoir compaction in Valhall, we have chosen $E = 0.8$ GPa.

Tor reservoir permeability history data is not available publicly. Chan (2005) utilized laboratory data from Teufel et al. (1991), stress path data from Zoback and Zinke

(2002) and the Deformation Analysis in Reservoir Space (DARS) method to estimate the porosity reduction with depletion. According to Chan, the porosity of the Tor formation at the crest was reduced from 41% to 35% from 1982 to 1998 (Chan, 2005). The empirical porosity-permeability relationship defined by Equation 3.18 was then used to obtain the permeability history. Figure 29 show the estimated change in permeability and porosity with depletion.

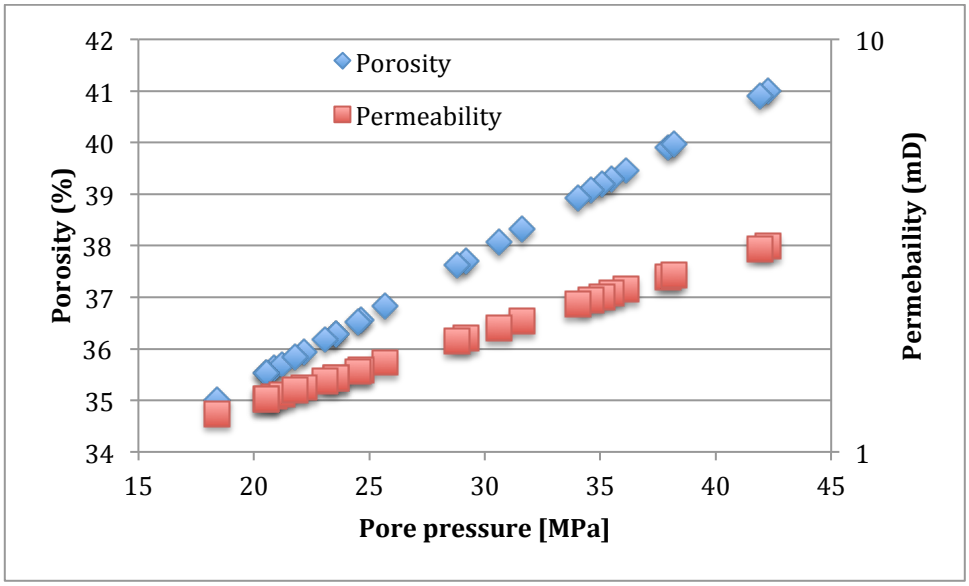

Figure 29: The estimated permeability and porosity as a function of reservoir pore pressure for the Tor formation in Valhall field (Chan, 2005; Munns, 1984; Teufel et al., 1991; Zoback and Zinke, 2002).

According to our calculations, the average reservoir permeability decreased from 3.15 md to 1.24 md over a span of 16 years as the pore pressure decreased from 42.2 MPa to 18.4 MPa.

With the stress path and pore pressure history, initial far-field stress, initial reservoir porosity and permeability, reservoir geomechanical material constants and the assumption that the wellbore pressure is 3 MPa less than the pore pressure to ensure

hydrocarbon production, the permeability distribution evolution can be evaluated through a combination of the Kirsch equations, the constitutive stress-strain relation and the Wong model. We will first compare the far-field permeability history obtained from our analysis to the estimated average reservoir permeability depicted in Figure 29 with $a = b = -7.04$ for the Wong model. Then we will set $a = -5.94, b = -8.14$ (such that $b - a = -2.2$ and $\frac{b+a}{2} = -7.04$) to assess how the permeability distribution evolution varies with a change in the Wong model parameters. Note that $a = b$ represents the isotropic Wong model in which the permeability change is isotropic, while $b < a$ represents the anisotropic Wong model with anisotropic change in permeability.

DISCUSSION AND RESULTS

Results from a case study of the permeability distribution evolution with depletion of a vertical production well in the Tor formation in Valhall are listed below. A computer program was developed to compute the permeability distribution throughout the history of the reservoir from 1982 to 1998. Case details are summarized in

Table 3.

Table 3: Data used as inputs to our model used to estimate the evolution of the permeability distribution with depletion in the Tor formation in Valhall field. Case 1 utilizes the isotropic Wong model defined by Equation (3.14) with a=b and Case 2 utilizes the anisotropic Wong model with b>a.

	Case 1 (isotropic)	**Case 2 (anisotropic)**
Initial P_p	42.2 MPa	42.2 MPa
Initial S_{hmin}	45.4 MPa	45.4 MPa
Initial S_{hmax}	47.3 MPa	47.3 MPa
S_v	49.2 MPa	49.2 MPa
$P_p - P_w$	3 MPa	3 MPa
ν	0.22	0.22
E	0.8 GPa	0.8 GPa
a	-7.04	-5.94
b	-7.04	-8.14
α	1	1
k_o	3.16 md	3.16 md
ϕ_o	0.41	0.41
A	0.72	0.72

Case 1 and 2 represent the isotropic and anisotropic permeability alteration models with depletion respectively.

Isotropic Wong model

Figure 30 and Figure 31 show the far-field porosity and permeability obtained from the isotropic Wong model. Note that permeability is a scalar for the isotropic Wong model and does not vary azimuthally in the far-field region (i.e. at $r/a \gg 1$). Our results strongly match the porosity and permeability history estimates.

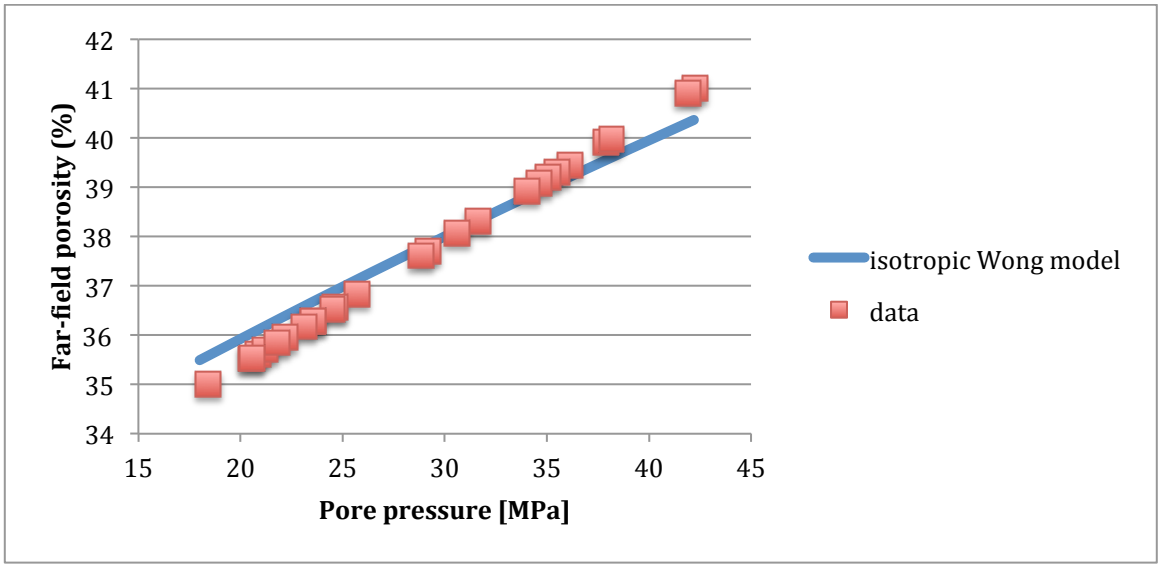

Figure 30: Comparison between the far-field porosity with depletion obtained from the isotropic Wong model and the estimated Tor formation permeability data obtained from Chan 2005.

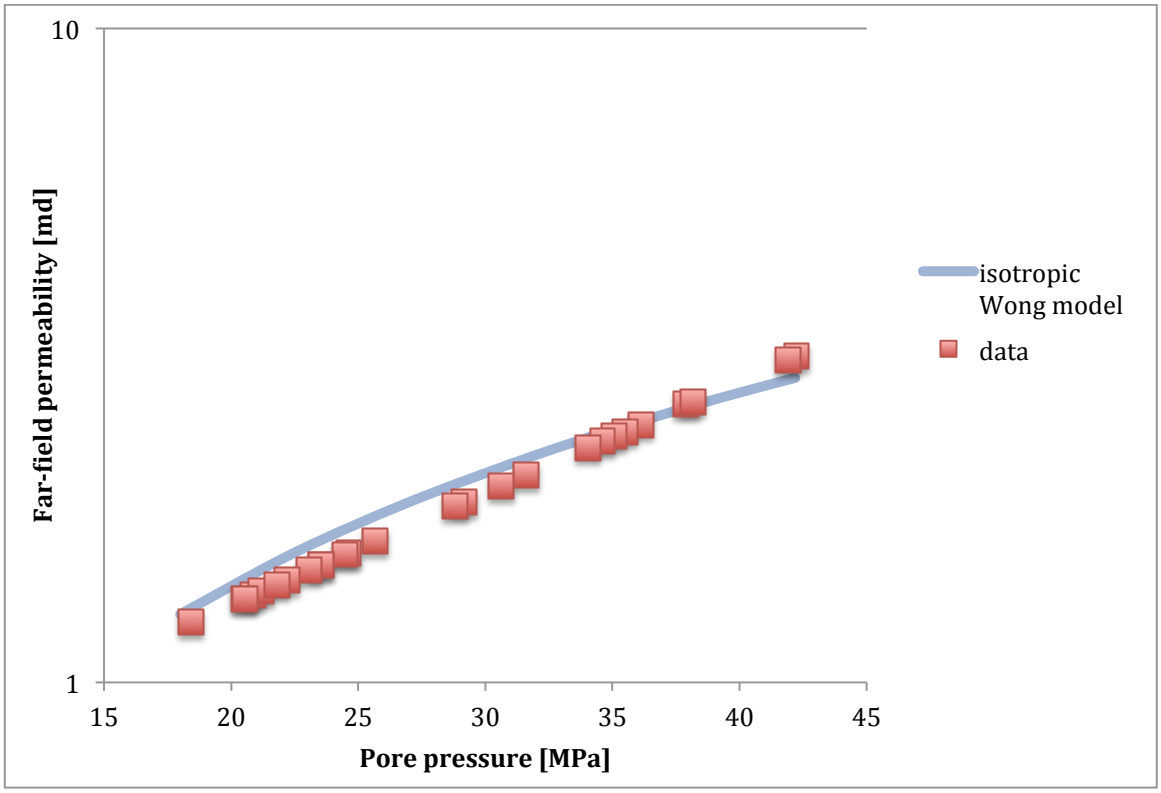

Figure 31: Comparison between the far-field permeability with depletion in the Tor formation at Valhall field obtained from the isotropic Wong model and reservoir permeability estimates derived from Chan (2005) and Munns (1984).

Figure 32 shows the distribution of the non-zero permeability components in the initial, non-depleted reservoir state. Due to the symmetry in the permeability distribution, we have chosen to only show the azimuthal range $\theta = [0°, 90°]$. Note that $\theta = 0°$ represents the direction of maximum stress and $\theta = 90°$ represents the direction of minimum stress. As expected, all the non-zero permeability components have identical distributions because the isotropic Wong model was used in this case. At the wellbore, i.e. at $r/a = 1$, the permeability is higher at the direction of maximum stress and lower at the direction of minimum stress due to the hoop stress distribution. At the minimum horizontal stress direction, the hoop stress is large resulting in significant compaction and hence reduces

the permeability significantly. At $\theta = 0°$ the permeability decreases with increasing radial distance, while at $\theta = 90°$ the permeability increases with increasing radial distance. Note that at $\theta = 45°$ the permeability remains the same with increasing radial distance.

Figure 33 shows the distribution of the non-zero permeability components in a depleted reservoir state. Note that the shape of the permeability distribution does not change. The permeability values simply shift down in value as pore pressure is reduced.

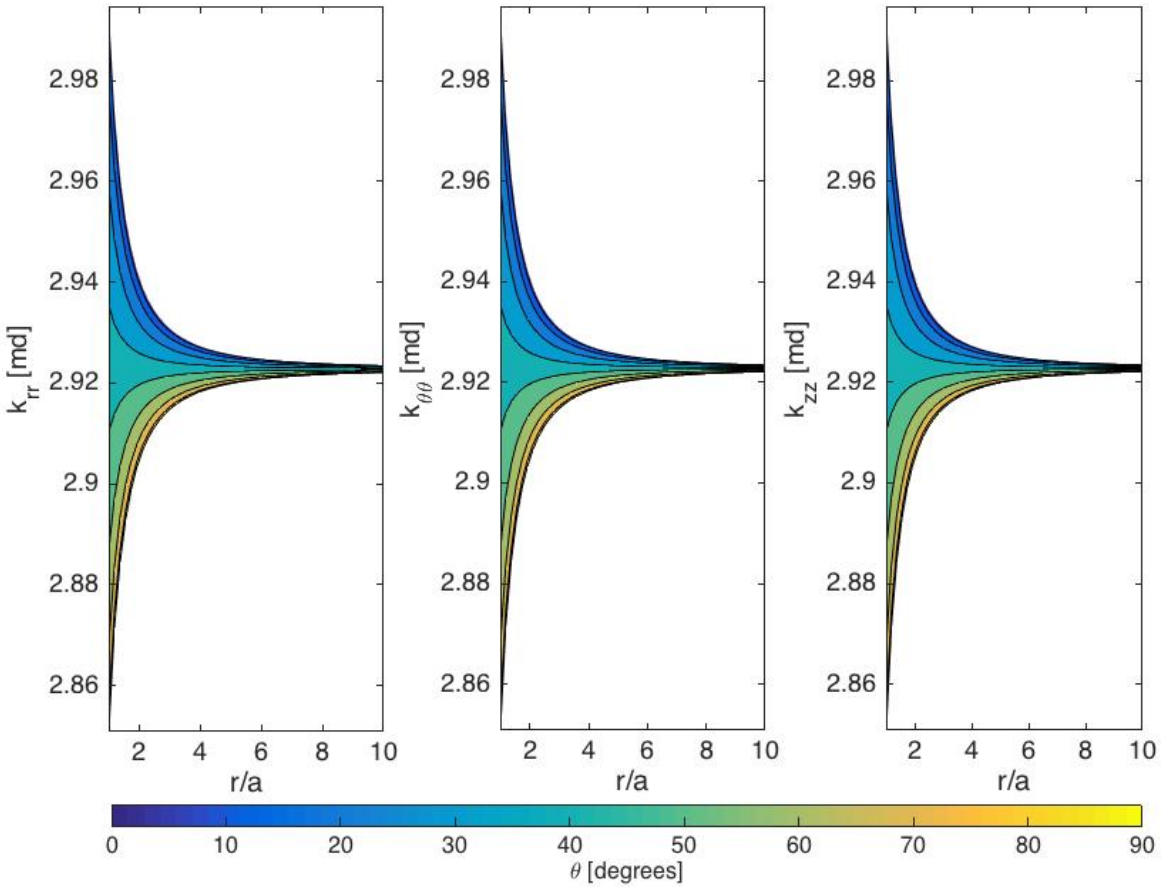

Figure 32: Permeability distribution around a vertical production well in the Tor formation at Valhall field at the initially un-depleted reservoir state, P_{pore} = 42.2 MPa, obtained through the isotropic Wong model with a=b=-7.04. A detailed list of parameters used in the model is presented in Table 3.

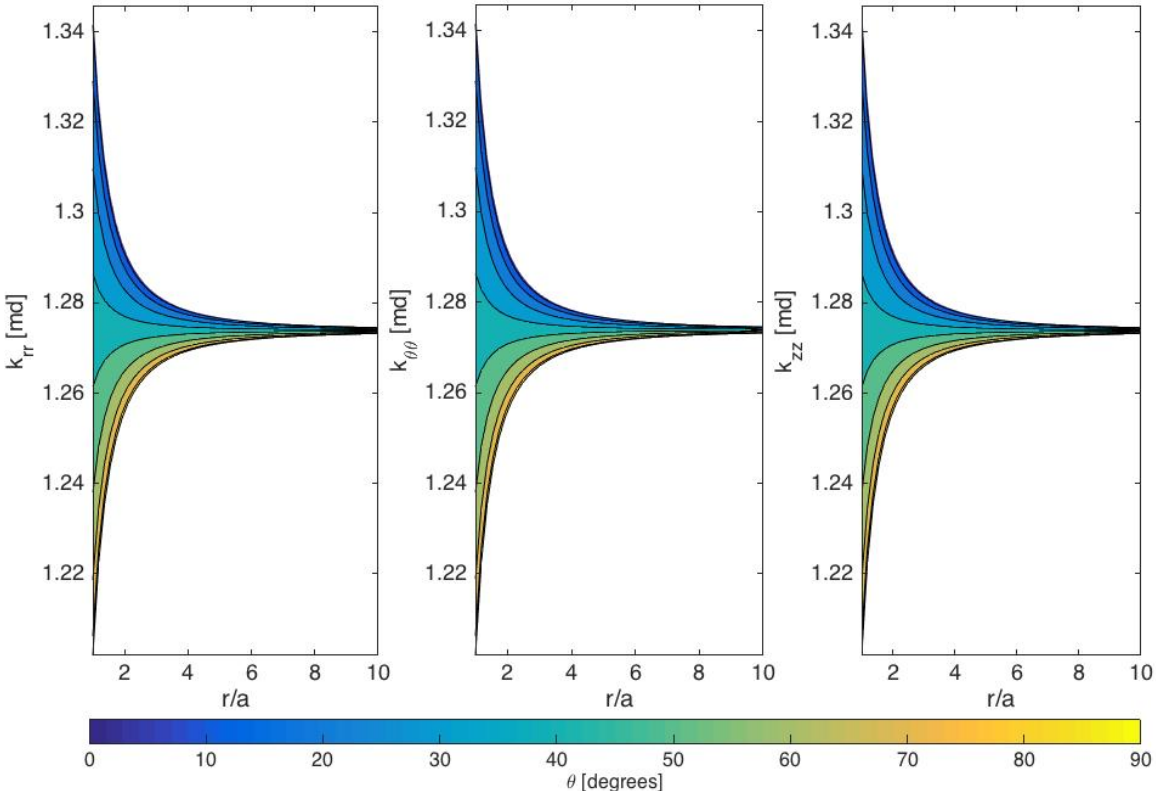

Figure 33: Permeability distribution around a vertical production well in the Tor formation at Valhall field at a depleted reservoir state, P_{pore} = 18.2 MPa, obtained through the isotropic Wong model with a=b=-7.04. A detailed list of parameters used in the model is presented in Table 3.

In the isotropic case, the determinate state variable for the permeability is the volumetric strain. Figure 34 shows the volumetric strain distribution at the initially un-depleted state and the final depleted state. Note that the permeability distributions follow the behavior of the volumetric strain distributions as expected.

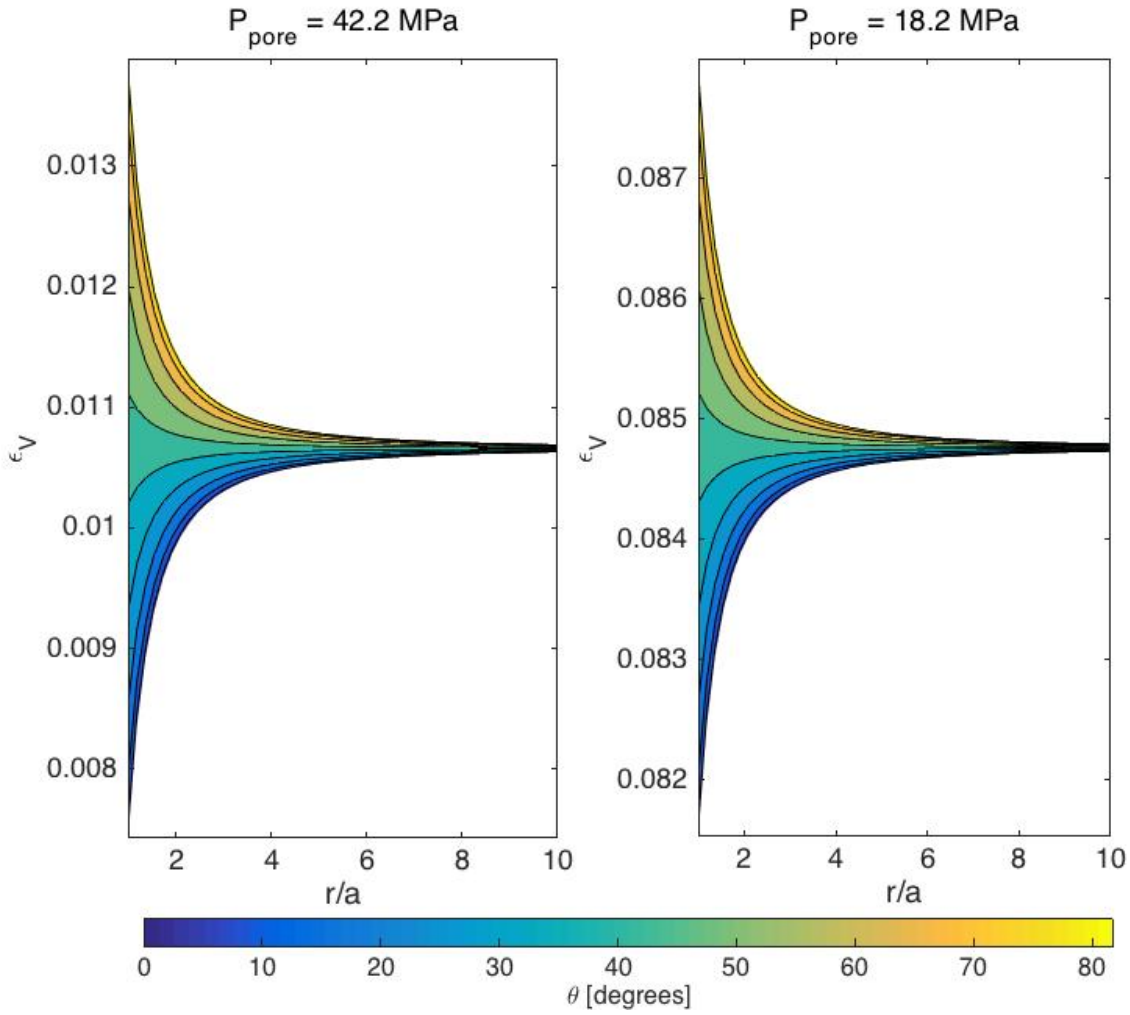

Figure 34: The evolution of the volumetric strain around a production well in the Tor formation at Valhall field obtained through the Kirsch equations and the constitutive stress-strain relation described by Equation 3.4. A detailed list of the parameters used for the model is presented in Table 3.

Anisotropic Wong model

The porosity distribution evolution with depletion does not differ from that obtained in Figure 30 for this case as the calculation of porosity is done directly through evaluation of volumetric strain and application of Equation 3.6, hence does not have an association the Wong model.

The average far-field permeability evolution with depletion obtained from the anisotropic Wong model is shown in Figure 35. In this case, the permeability does vary azimuthally in the far-field direction therefore we calculated the azimuthally averaged value of the far-field permeability to compare the permeability values obtained through the anisotropic Wong model to our permeability history estimates. Note that permeability changes are anisotropic, hence three separate curves for each of the non-zero permeability components are shown. Although the permeability changes are anisotropic, the averaged far-field permeability components follow a similar trend and match our data well.

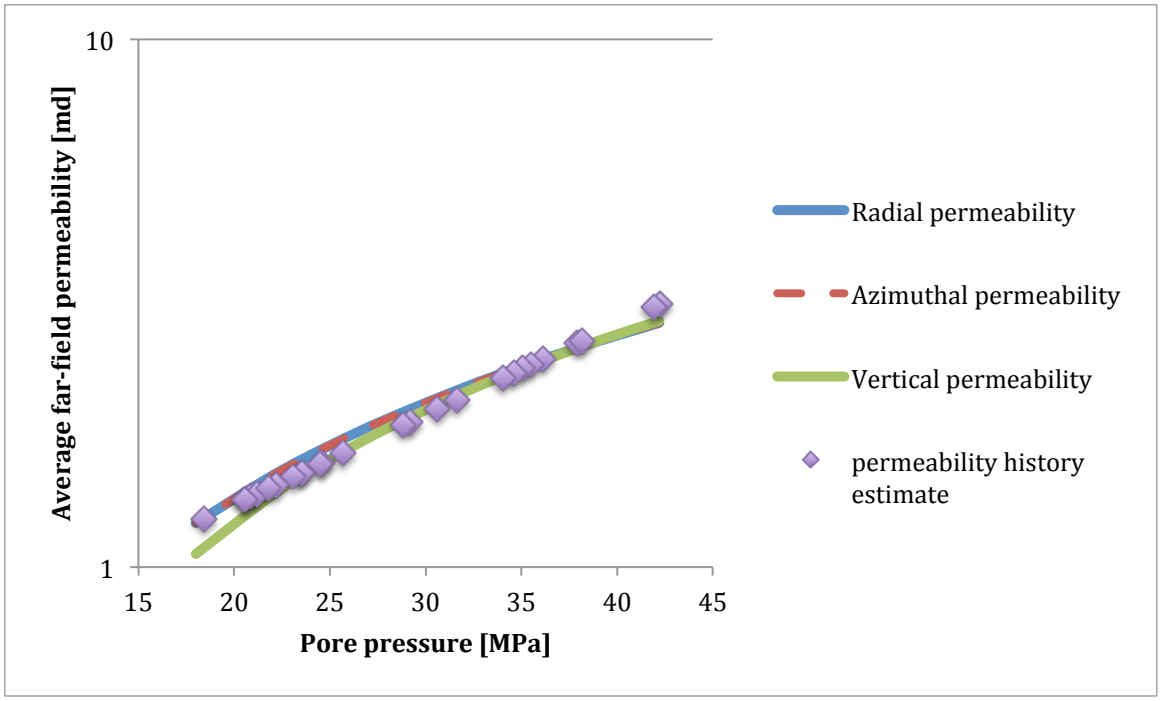

Figure 35: Comparison between the far-field permeability with depletion of the Tor formation in Valhall field obtained through the anisotropic Wong model and the estimated reservoir permeability data derived from Chan (2005) and Munns (1984).

Figure 36, Figure 37 and Figure 38 show the evolution of the non-zero permeability components distribution obtained by the anisotropic Wong model from an initially un-depleted state, intermediate depletion state and final depletion state. The permeability components do not have similar values and each behave differently. The vertical permeability distribution, k_{zz}, for the anisotropic case is similar to the permeability obtained from the isotropic case due to the zero vertical strain assumption in the Kirsch equations. Recall that we have chosen to only show the azimuthal range $\theta = [0°, 90°]$, due to the symmetry of the permeability distribution. For the $k_{r\theta}$ distribution, we had to shift the azimuthal range to $\theta = [-45°, 45°]$ in order to fully capture the behavior of the $k_{r\theta}$ permeability distribution. Note that the $k_{r\theta}$ permeability component is maximum at $\theta = 45°$ and minimum at $\theta = -45°$ though the permeability values are low compared to the other components. At the wellbore, $k_{r\theta}$ is zero. In the far-field region, $k_{r\theta}$ varies azimuthally between -0.01 md and 0.01 md. Unlike diagonal elements of the matrix representation of the permeability tensor, off diagonal permeability elements, such as $k_{r\theta}$, can have a negative magnitude. With depletion, the $k_{r\theta}$ distribution remains unchanged.

The radial and azimuthal permeability components change significantly in the anisotropic case and behave differently from the isotropic case. The radial permeability distribution, k_{rr}, increases at $\theta = 90°$ and decreases at $\theta = 0°$ with increasing radial distance as in the isotropic case, though the distribution is skewed toward lower permeability values near the wellbore and azimuthal variability exists in the far-field. The hoop stress appears to have diminishing effects on the near-wellbore radial permeability component, because it causes contractive azimuthal strain resulting in an increase in tortuosity in the radial direction. On the other hand, the hoop stress appears to have enhancing effects on the near-wellbore azimuthal permeability, because it causes dilative

radial strain resulting in a decrease in tortuosity in the azimuthal direction. In the isotropic case with $a = b$, we only considered changes in flow area due to increase in volumetric strain. By including anisotropy and setting $b > a$, we have incorporated the effect of tortuosity into the strain-induced permeability model. Assuming isotropic initial permeability, principle strains aligned to the $[r, \theta, z]$ coordinate system and zero vertical strain, Equation 3.13 can be rewritten as

$$\begin{bmatrix} k_{rr}/k_i \\ k_{\theta\theta}/k_i \\ k_{zz}/k_i \end{bmatrix} = 1 + \begin{bmatrix} a\varepsilon_V + (b-a)\varepsilon_{\theta\theta} \\ a\varepsilon_V + (b-a)\varepsilon_{rr} \\ b\varepsilon_V \end{bmatrix}. \tag{3.19}$$

The effect of flow area on each permeability component is determined by a and ε_V (Wong, 2003). For the radial permeability component, effect of tortuosity on permeability is dictated by $(b - a)$ and $\varepsilon_{\theta\theta}$ (Wong, 2003). For the azimuthal permeability component, the effect of tortuosity on the permeability is dictated by $(b - a)$ and ε_{rr} (Wong, 2003).

The $k_{\theta\theta}$ distribution tends to decrease with increasing radial distance. Near-wellbore azimuthal permeability is higher in the direction of maximum stress and lower in the direction of minimum stress as expected. However, in the far-field region the azimuthal permeability component is higher in the direction of minimum stress and lower in the direction of maximum stress. This change in behavior is attributed to the change in the state of the radial strain from a dilative state to a compressive state as we move further away from the near-wellbore region. At the far-field region, the radial strain component is comparable in magnitude to the azimuthal strain and is distributed in accordance to the far-field stresses, i.e. higher in the direction of maximum stress and lower in the direction of minimum stress. This causes higher contractive radial strain in the direction of maximum stress than the direction of minimum stress, hence results in

relatively low $k_{\theta\theta}$ values at direction of maximum stress associated with a high increase in the tortuosity.

As pore pressure decreases, k_{rr} distribution is reduced significantly at the near-wellbore region in comparison to the far-field region. On the contrary, the $k_{\theta\theta}$ distribution is enhanced significantly near the wellbore wall in comparison to the far-field region. With further depletion, increasingly less azimuthal variation is observed in the radial and azimuthal permeability components in both the near-wellbore and far-field region. This reduction in azimuthal variation is in accordance with the reduction in azimuthal variation observed in the strain components as shown in Figure 39.

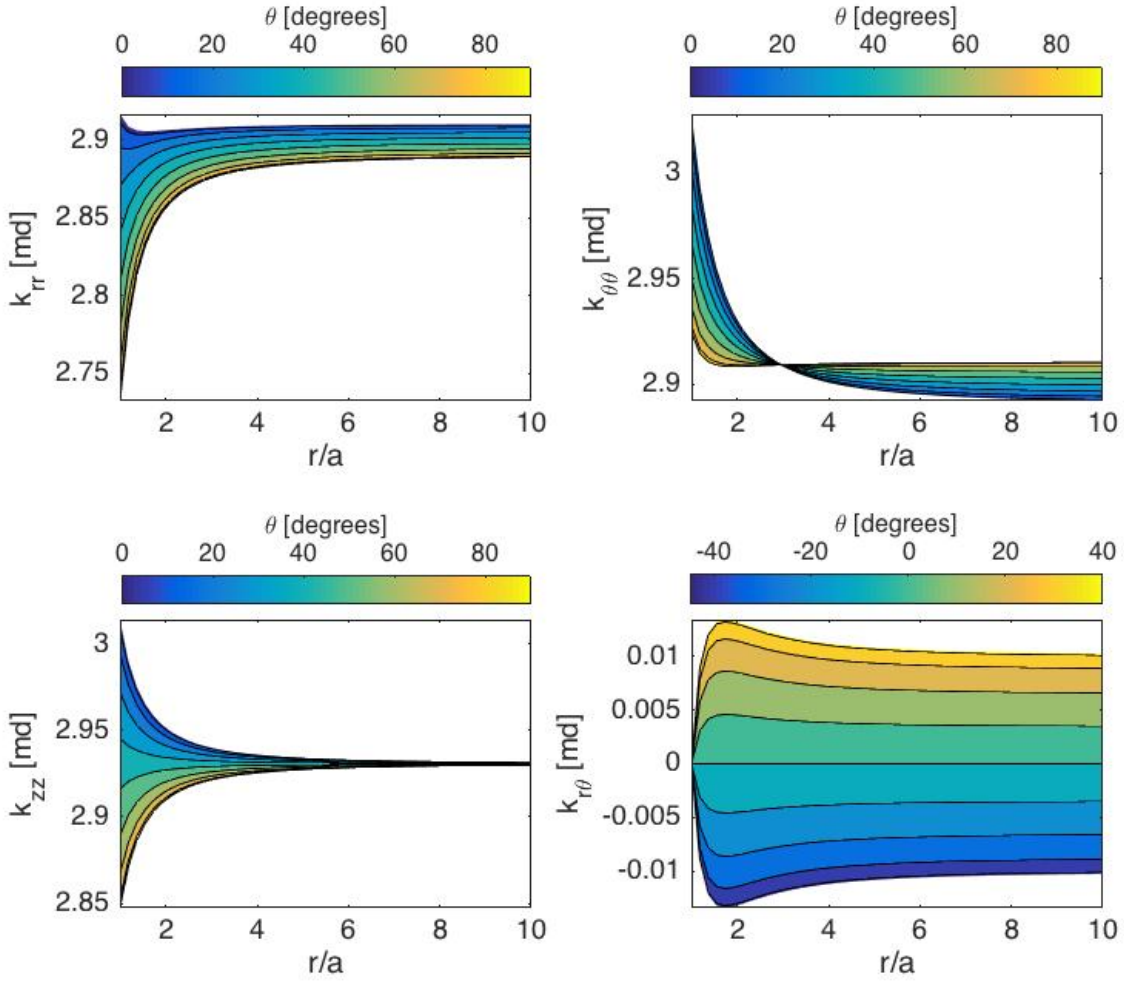

Figure 36: Permeability distribution around a vertical production well in the Tor formation at Valhall field at the initially un-depleted state, P_{pore} = 42.2 MPa, obtained through the anisotropic Wong model. A detailed list of parameters used in the model is presented in Table 3.

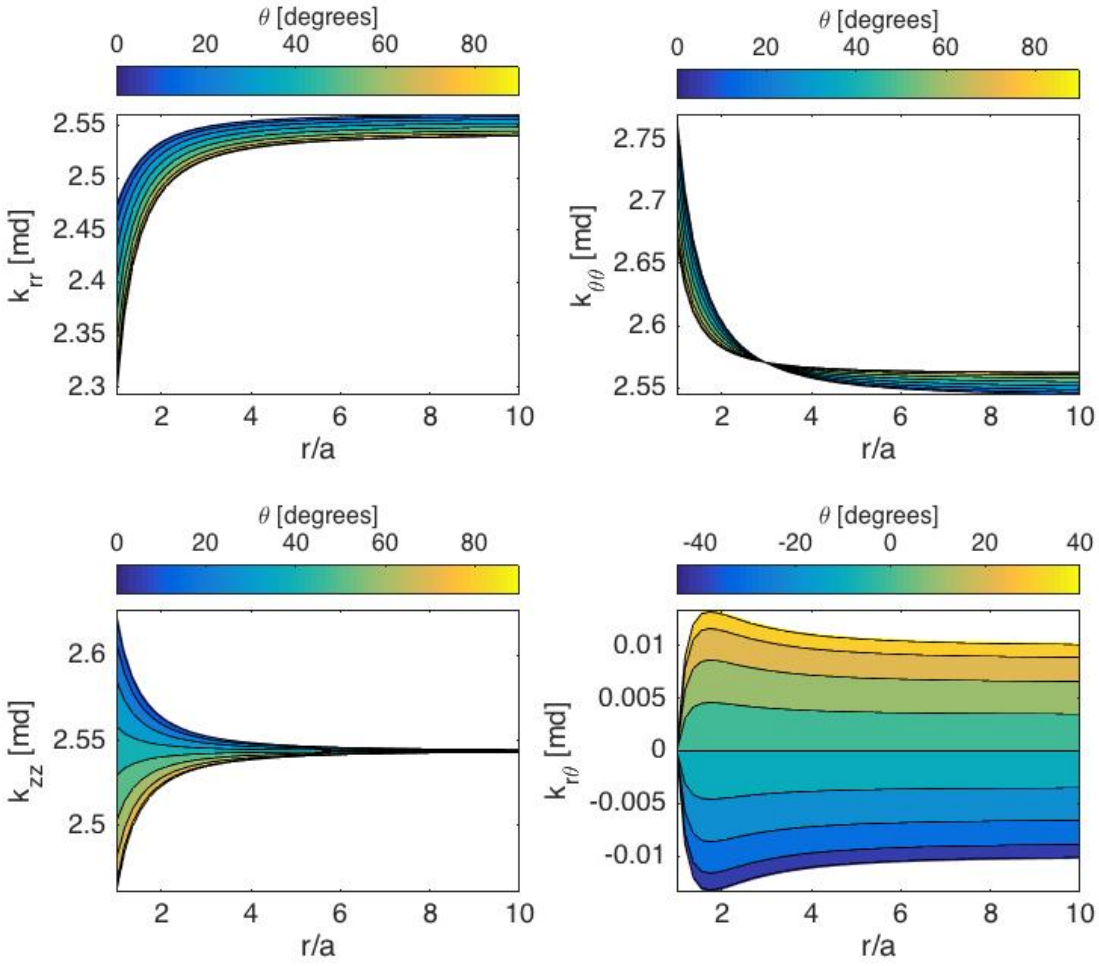

Figure 37: Permeability distribution around a vertical production well in the Tor formation at Valhall field at the initially un-depleted state, P_{pore} = 37.2 MPa, obtained through the anisotropic Wong model. A detailed list of parameters used in the model is presented in Table 3.

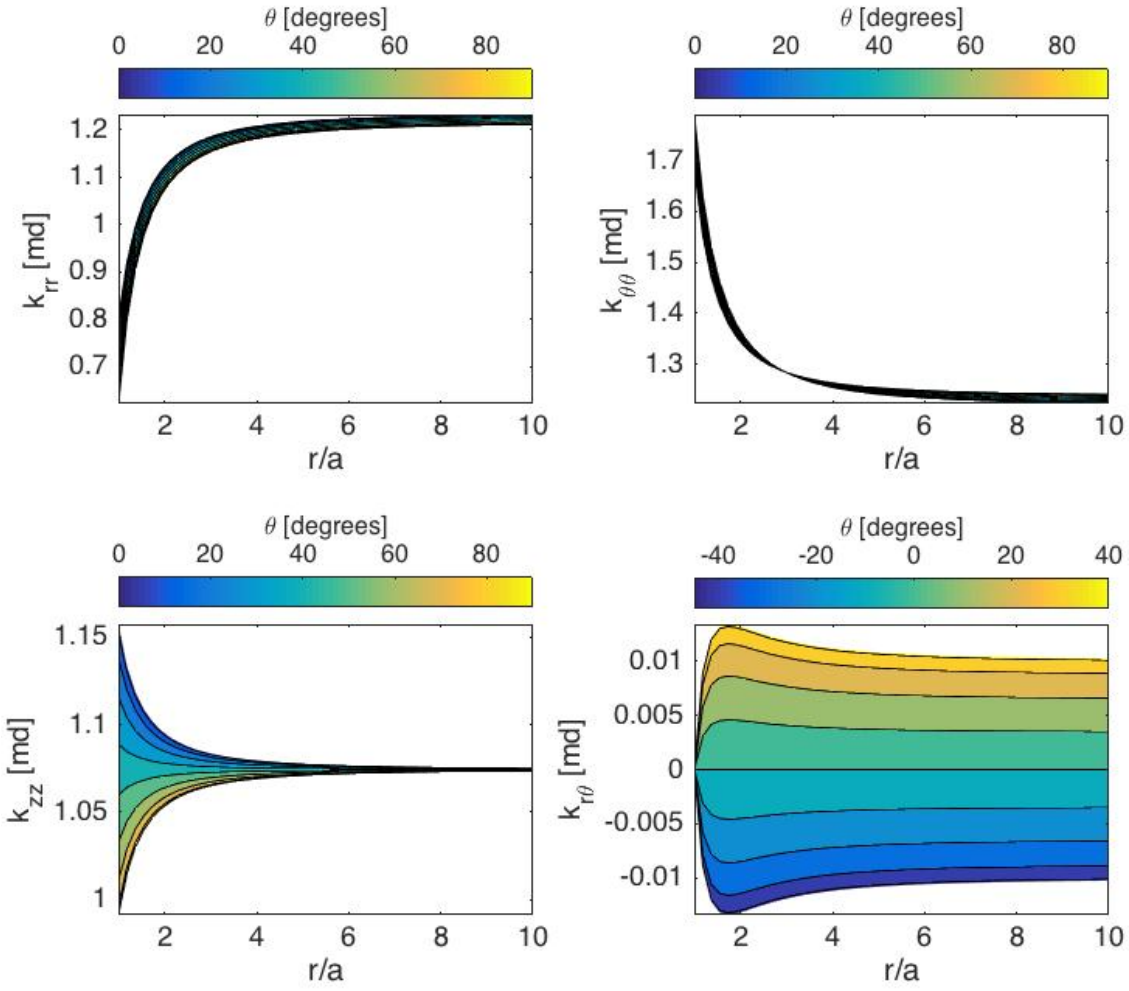

Figure 38: Permeability distribution around a vertical production well in the Tor formation at Valhall field at the initially un-depleted state, P_{pore} = 18.2 MPa, obtained through the anisotropic Wong model. A detailed list of parameters used in the model is presented in Table 3.

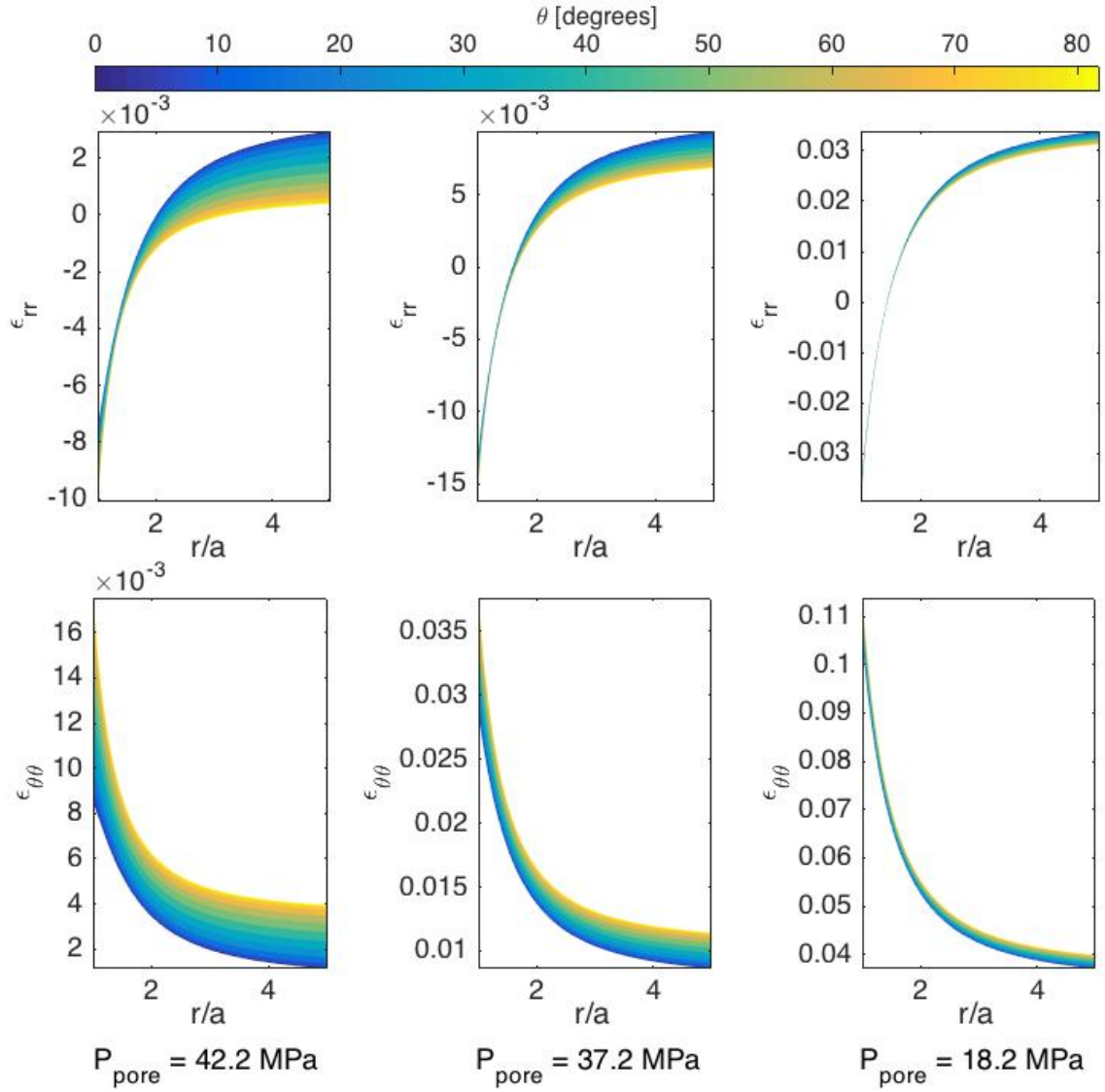

Figure 39: The evolution of the radial and azimuthal strain from an un-depleted state, intermediate state of depletion and a final depletion state around a production well in the Tor formation at Valhall field obtained through the Kirsch equations and the constitutive stress-strain relation described by Equation 3.4. A detailed list of the parameters used for the model is presented in Table 3.

CONCLUSIONS

We have used a combination of the Kirsch equations, the constitutive stress-strain relation and the strain-induced permeability alteration model by Wong to evaluate the

near-wellbore and far-field permeability in producing wells of depleted reservoirs (Wong, 2003; Kirsch, 1898). Through a case study of a producing well in the Tor formation at Valhall field, we compared the evolution of the permeability distribution with depletion through two permeability alteration models, one that considers isotropic permeability changes and the other considers anisotropic permeability changes. Isotropic permeability change models, commonly used in industry, assume permeability changes the same in all direction by an associated change in porosity or flow area. The anisotropic model by Wong (2003) incorporates changes in flow area and tortuosity in order to allow for anisotropic changes in permeability. In the case study, we were able to retrieve the average behavior of the reservoir documented in literature through both models (Munns, 1984; Zoback and Zinke, 2002; Chan, 2005). By introducing anisotropic in the permeability change, we say a significant difference in the near-wellbore permeability in comparison to the isotropic permeability change model. At the near-wellbore region of the producing well, the isotropic model will tend to overestimate the radial permeability and underestimate the azimuthal permeability. Assuming isotropic permeability change may therefore result in the overestimation of future production. Parameters of the anisotropic permeability alteration model by Wong (2003) can be tuned to improve well performance predictions and increase the accuracy of reservoir production forecasting.

Chapter 4: Fracture pressure profile for anisotropic formations

Accurate determination of the fracture pressure profile is important in drilling applications. Underestimation of the fracture pressure can lead to lost circulation issues. Minimizing loss circulation events reduces costs associated with unrecovered mud and unproductive time. In industry, the Kirsch equations are commonly used to calculate the fracture pressure due to their simplicity. The inherent assumption of isotropic elastic properties in the Kirsch equations can lead to significant error in calculating the fracture pressure in anisotropic shale formations. This paper utilizes the Fort Worth Basin as a case study to compare the fracture pressure from the isotropic solution and the anisotropic solution of stress around a horizontal borehole. Results suggest that as the difference between the far-field stress acting on the borehole increases, the effect of material elastic anisotropy is more evident.

INTRODUCTION

The calculation of stress around a cavity has been addressed in many publications. Kirsch (1898) developed the equations for stress around a circular cavity of an isotropic elastic homogeneous medium. A generalized version of the Kirsch equations was established by Lekhnitskii (1963) for anisotropic media. Amadei (1983) applied the generalized plane stress assumption to these equations to calculate the stress around an arbitrarily oriented wellbore. Aadnoy et al. (1987) incorporated various rock failure criteria to assess the stability of deviated boreholes in isotropic homogenous rock. Aadnoy (1988) evaluated the borehole stability in anisotropic rock formations, concluding that assuming isotropic rock properties instead of anisotropic elastic constants introduces small error for predicting the fracture-pressure, but high error for predicting collapse-pressure. The analytical Amadei (1983) solution faced much criticism due to an

inherent singularity in the stress equations under special cases of symmetry. Gaede et al. (2012) addressed these issues by showing that the singularity is unlikely to be encountered in real rocks and that the solution does indeed contain all special cases of symmetry.

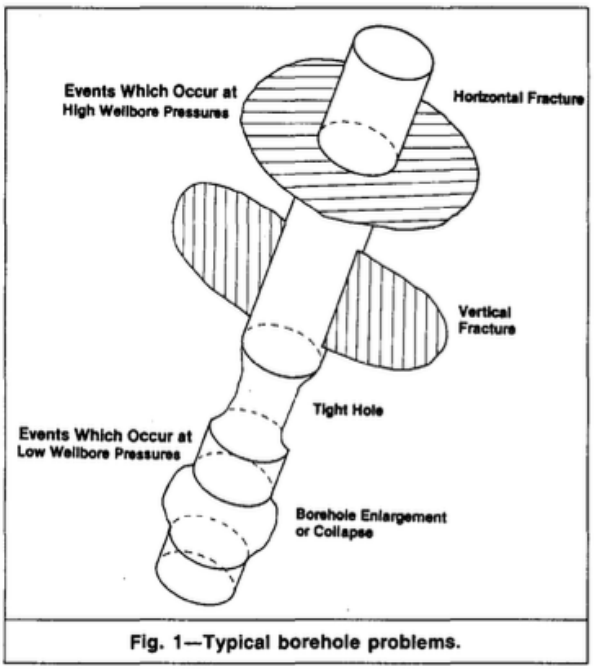

Figure 40: Depiction of various borehole problems faced while drilling a well (Aadnoy and Chenevert, 1987).

Wellbore instability issues include borehole collapse and lost circulation. Figure 40 shows a pictorial representation of borehole problems during drilling. Wellbore stability can be managed by wellbore pressure through the mud weight. Low mud weight can cause shear failure leading to borehole collapse issues. High mud weigh can cause tensile failure leading to borehole fracturing and lost circulation issues. The mud window is the range of mud weights that maintain the stability of the wellbore. Shear failure is commonly characterized by the Mohrs-Coulomb failure envelope given by $\tau=\tau_0(\beta)+\sigma\tan[\phi\ (\beta)]$ where τ_0 is the cohesion, ϕ is the angle of internal friction, τ is the

shear stress, and σ is the normal stress. The cohesion and angle of internal friction are material properties and depend on the bedding orientation for anisotropic materials as shown in Figure 41. Fracture failure is given by the tensile strength of the rock. When the minimum principal stress in the material exceeds the tensile strength of the material, a fracture forms. We assume that the tensile strength of the rock is zero because rocks are generally weak in tension and fractures will initiate in existing fractures as shown in Figure 42. This paper examines the tensile failure in anisotropic rock formation.

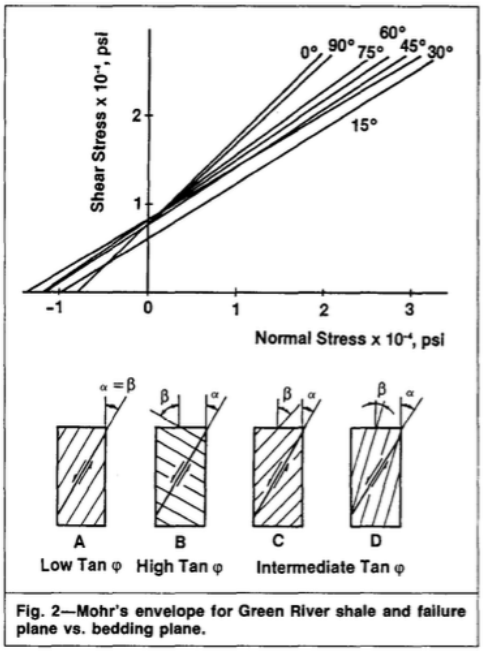

Fig. 2—Mohr's envelope for Green River shale and failure plane vs. bedding plane.

Figure 41: The modified Mohrs-Coulomb shear failure criteria for a transverly isotropic medium (Aadnoy, 1988).

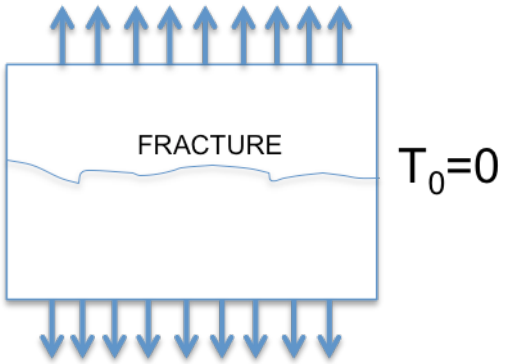

Figure 42: Representaiton of the zero tensile strength failure criteria.

The isotropic solution for stress around a borehole is commonly used in industry due to its simplicity. Only two elastic constants, the Young's modulus and the Poisson's ratio, fully define the relationship between stress and strain as shown in Equation C.1. A more realistic representation of rock formations is a transversely isotropic medium as shown in Figure 43. In a transversely isotropic medium, five elastic constants are required to define the stress-strain relationship as shown in Equation C.2 of Appendix C.

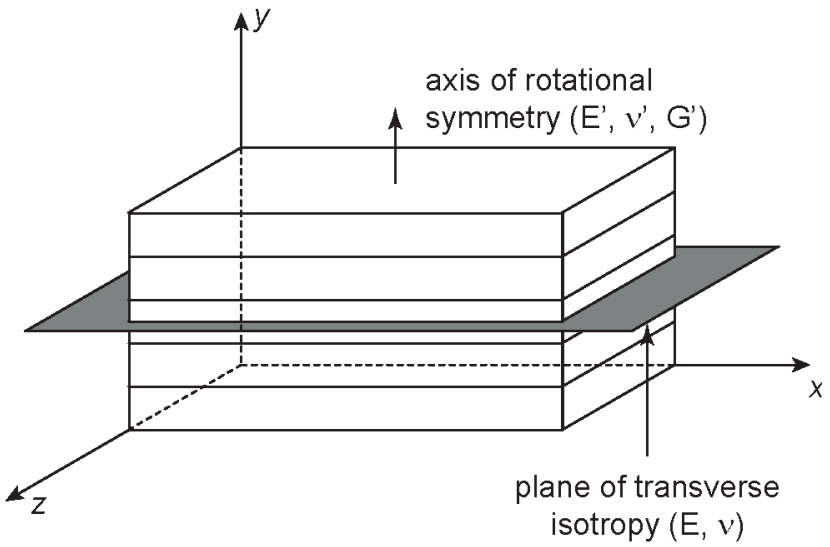

Figure 43: Representation of a transversly isotropic medium. (Image obtained from http://www.geomechanica.com/blog/wp-content/uploads/2014/02/Figure_5.png)

Through the propagation of acoustic waves through a formation, one can obtain the five elastic constants characterizing the rock's stress-strain relationship in the linear elastic regime as shown in Figure 44.

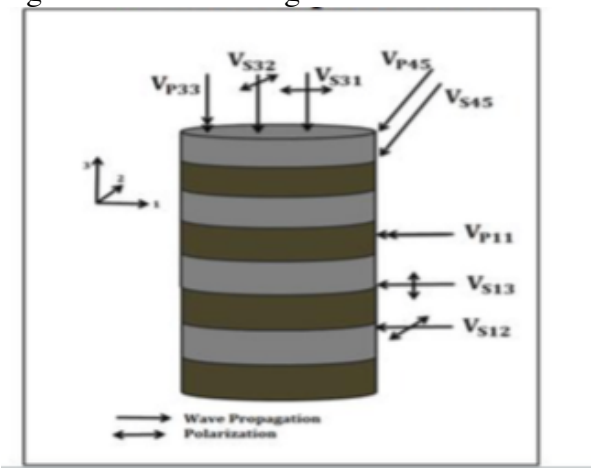

Figure 44: Representation of acoustic measurement technique for obtaining the elastic constants of a transversely isotrpic medium (Mokhtari, 2015).

STATEMENT OF PROBLEM:

Shale reservoirs exhibit anisotropic elastic behavior. Treating them as an isotropic medium can lead to error in calculating fracture-pressure. Such error may lead to loss circulation issues when drilling. In this chapter, we calculate the fracture-pressure in the of the Lower Barnett-shale formation in the Fort Worth Basin. In comparing the predicted fracture-pressure from the transversely isotropic solution to that of the isotropic solution, we evaluate the error associated with the isotropic assumption commonly used in industry.

METHODOLOGY:

A computer program is developed to calculate the stress around an anisotropic formation through the equations given in Amadei (1983). The code and the model are validated by comparing the output to results obtained in Gaede et al. (2012). Data on the Lower Barnett-shale formation bedding orientation, bedding azimuth, formation depth, in-situ stress orientation, in-situ stress magnitude, and formation elastic properties are obtained from Sone et al. (2013), Sone et al. (2014) and Bruner et al. (2011). The fracture pressure of a horizontal well orientated in the direction of minimum stress is calculated through the computer program and the model output for the isotropic and transversely isotropic cases are compared.

DISCUSSION AND RESULTS:

Model Validation

Both the isotropic and the anisotropic solutions to stress around a borehole given by Kirsch (1898) and Amadei (1983) are fully analytical. The complexity of the anisotropic solution stems from the fact that it involves the complex plane. In developing the code for the model, we faced some issues with one of the equations associated with

the anisotropic solution. Some equations such as f(z)=sqrt(z) are not functions in the complex plane as one input returns two values as shown in Figure 45. One must specify the range of phase angles such that the equation is indeed a function. As shown in Appendix B, the equations given by Amadei (1983) are simplified such that the phase angles range from [0,2π].

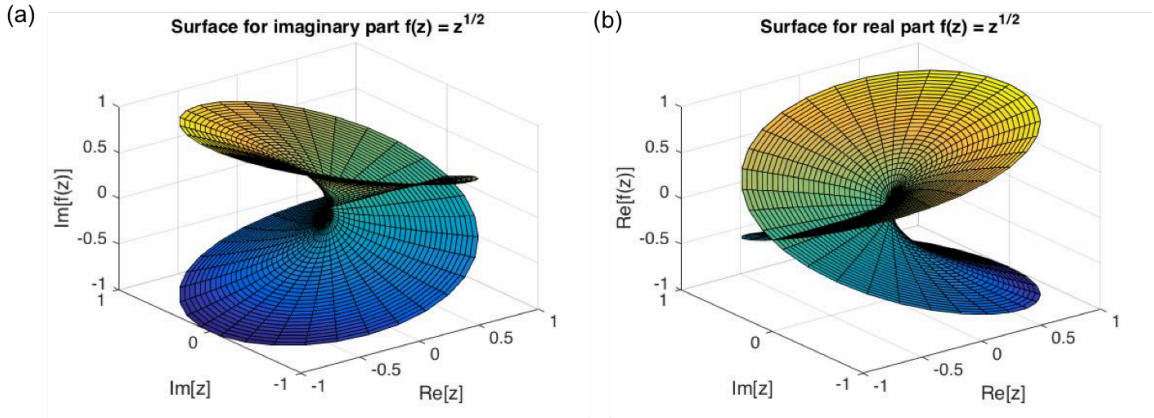

Figure 45: Reiman surface of the square root function.

Table 4: Model validation elastic material constant inputs (Gaede et al., 2012).

Geomechanical properties
E_h=31.17 GPa
E_v=15.42 GPa
v_h=0.079
v_v=0.32
G_v=7.05 GPa

Table 5: Various cases used to validate the anisotrpic model for stress around an arbitrarily oriented wellbore (Gaede et al., 2012). Note α_D and α_A are the wellbore deviation and azimuth respectively. β_D and β_A are the bedding dip angle and bedding azimuth respectively.

Case	α_D	α_A	β_D	β_A
1	0°	0°	0°	0°
2	45°	45°	0°	0°
3	90°	0°	0°	0°

In order to validate the developed computer program, we compare its output to results obtained by Gaede et al. (2012). Shown in Table 4 are the rock elastic properties used as inputs to the model. Three cases are used for validation with the orientation of the well as shown in Table 5: vertical, deviated and horizontal borehole orientation. Results shown graphically in Figure 46 indicates that the computer program output agrees with results obtained by Gaede et al. (2012).

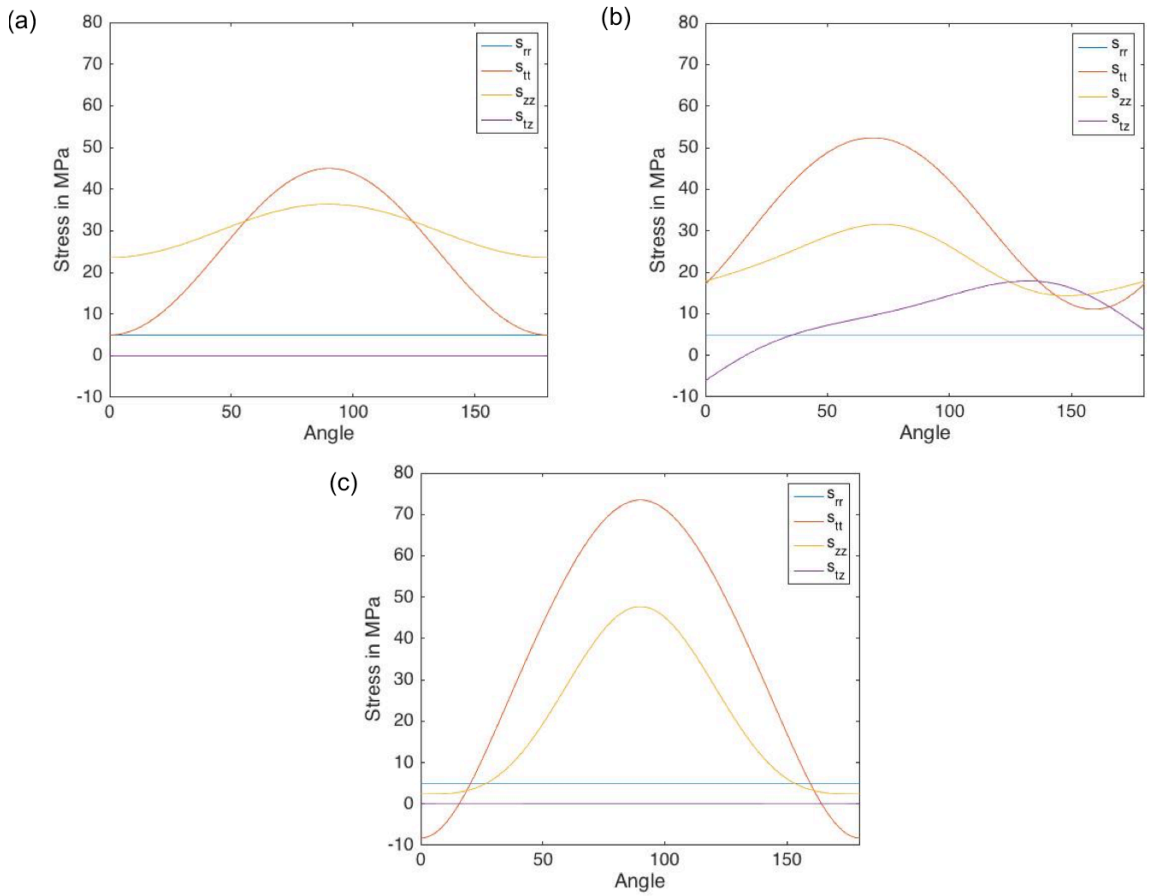

Figure 46: Validation of anisotropic solution to stress around an arbitratily oriented wellbore. Three cases are tested (a) Case 1, (b) Case 2 and (c) Case 3. Details of each case is shown in Table 2 and the elastic material constants used for the validation are shown in Table 1. The results are compare to those obtained by Gaede et al. (2012). The angles shown are in degrees.

Case Study: The Barnett Shale formation

The Barnett Shale formation is location in North Texas extending less than 20 miles from the Texas-Oklahoma border. It consists sedimentary rock dating back to the Mississippian period and lies between the Marble Falls and Ellenburger formations. The Forestburg Limestone divides the Barnett Shale formations in to the Upper and Lower Barnett. This paper examines rock properties and fracture pressures of the Lower Barnett

Shale at a depth of 8500 ft. The marker depth of the top of the Ellenburger formation is shown in Figure 47. It is assumed that the top of the Ellenburger formation and the top of the lower Barnett shale formation are parallel. Note that there are many faults surrounding the Fort Worth Basin. These faults cause the Barnett Shale formation to be in a strike-slip faulting environment. In such environment, the maximum horizontal stress is larger than the overburden stress. Data from the structural map of the formations in the Fort Worth Basin are extracted to calculate the bedding azimuth and bedding dip angle. A contour map of the bedding orientation is shown in Figure 48. Note that the bedding dip angle range from 0° to 1.4° and the bedding orientation range from N40°W to N80°E. In the analysis done in this paper, we use an average value of 0.64° bedding dip and N51°E azimuth.

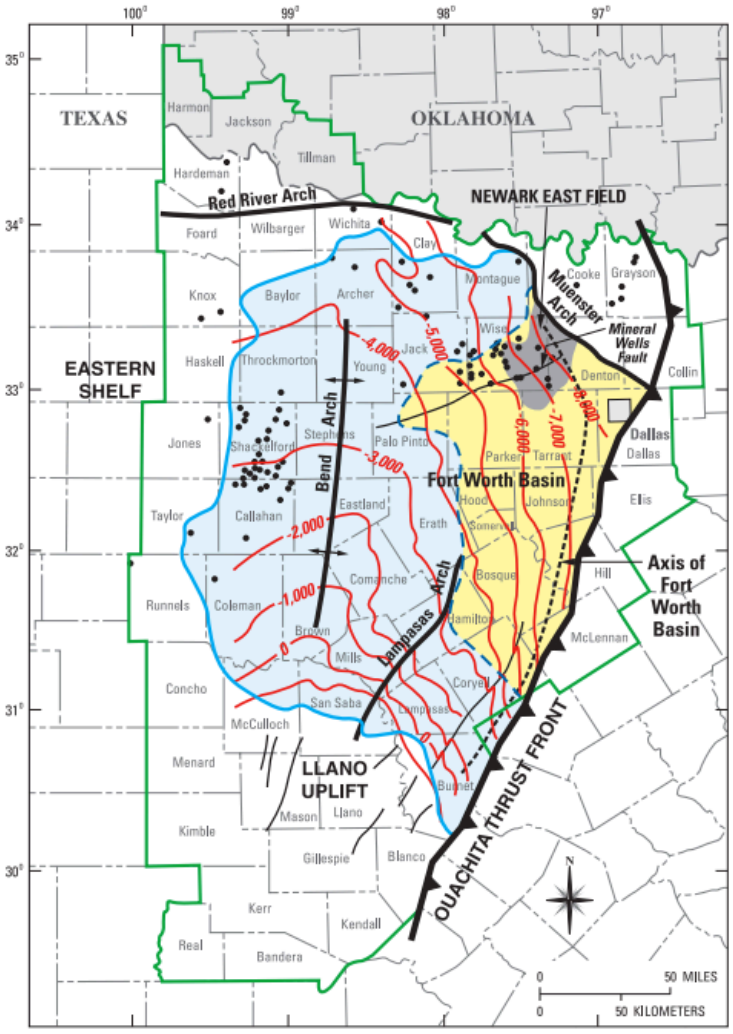

Figure 47: Structural contour map of the Ellenburger formation in the Fort Worth Basin (Bruneret et al, 2011).

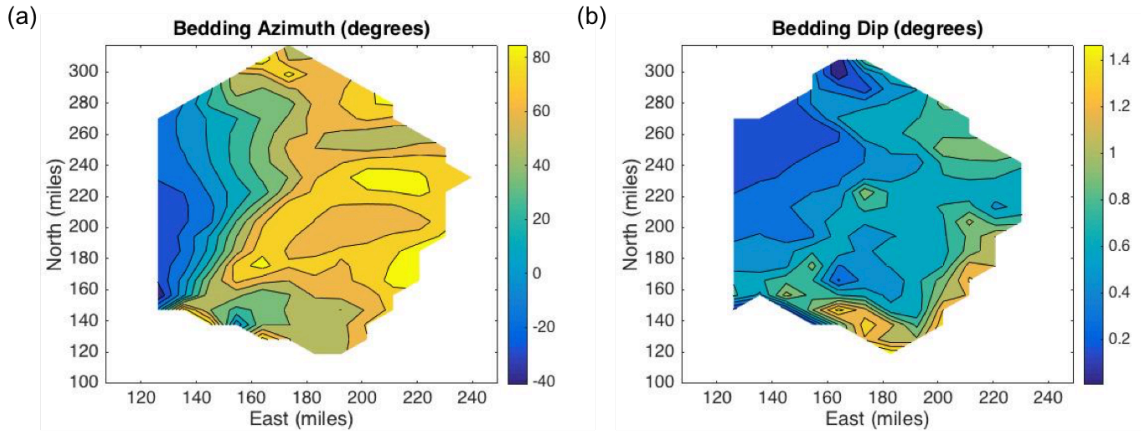

Figure 48: Lower Barnett shale bedding orientation contours - (a) bedding azimuth contour, (b) bedding dip contour.

In-situ stress direction, in-situ stress magnitude and formation elastic properties are key parameters for calculating fracture-pressure. Sone et al. (2014) examined image logs of drilling induced fractures and concluded that the maximum horizontal stress lies in the N20°E direction and constrained the maximum horizontal stress to be in the range of 65 and 85 MPa. Through analysis of closure pressure in LOT tests, Sone et al. (2014) have narrowed down the range of the minimum horizontal stress to be between 44 and 47 MPa. In this paper we use the average value of 45.5 MPa for the minimum horizontal stress magnitude. Interpretation of the density logs yields an overburden stress of 65 MPa at 8500 ft. Anisotropic elastic property data for the Lower Barnett Shale is obtained from Sone at al. (2013). A summary of the elastic properties is shown in

Table 6.

Table 6: Elastic material constants for the Lower Barnett Shale assuming a transversly isotorpic medium (Sone et al., 2013).

Elastic Parameters	
E_z	25.9 GPa
E_x	45.3 GPa
v_{xy}	0.267
v_{zx}	0.16
v_{xz}	0.28
G_{yz}	16 GPa

Rock failure is typically evaluated through analysis of the effective stress. The effective stress of the rock is given by $\sigma = S - \alpha P_p$ where σ is the effective stress, S is the total stress, α is the Biot coefficient, and P_p is the pore pressure (Biot, 1962). Montgomery et al. (2005) calculated the pore pressure at 8500 ft of the Lower Barnett Shale to be 30.5 MPa. Sone et al. (2014) assume $\alpha = 1$ as there is no accurate method to date that measures Biot coefficient of a shale formation.

In this paper we examine how variations in the maximum horizontal stress magnitude and the Biot coefficient affect the predicted fracture pressure for both the isotropic and anisotropic solution in a horizontal well drilled in the direction of minimum horizontal stress. The isotropic elastic properties are obtained by assuming that the vertical elastic properties shown in

Table 6 are isotropic.

Assuming a Biot coefficient of one, we first analyze the predicted fracture pressure at different maximum horizontal stress magnitudes ranging from 65 MPa to 85

MPa as constrained by Sone et al. (2014). Results are shown in Figure 49. As expected, the larger the difference between the overburden and the maximum horizontal stress, the lower the fracture pressure. Note that at low maximum horizontal stress, the isotropic solution yields a higher fracture pressure than the anisotropic solution. As the maximum horizontal stress increases, the fracture pressure predicted by the anisotropic solution surpasses the isotropic solution fracture pressure prediction. At a maximum horizontal stress of 85 MPa, the difference between the anisotropic solution and the isotropic solution is 7 MPa. This suggests that as the difference between the far-field stresses acting on the wellbore increases, the effect of the material elastic anisotropy is more evident. Note that it is unlikely that the rock will be fractured during drilling operation at this depth and wellbore orientation as the fracture pressures range between 80 and 100 MPa. At 8500 ft, this corresponds to a range of [26 ppm, 32 ppm] mud weight. However, in estimating the required surface pressure for a hydraulic fracturing operation, the difference between the isotropic and anisotropic solution is significant and may lead to error in estimating the fracture initiation pressure.

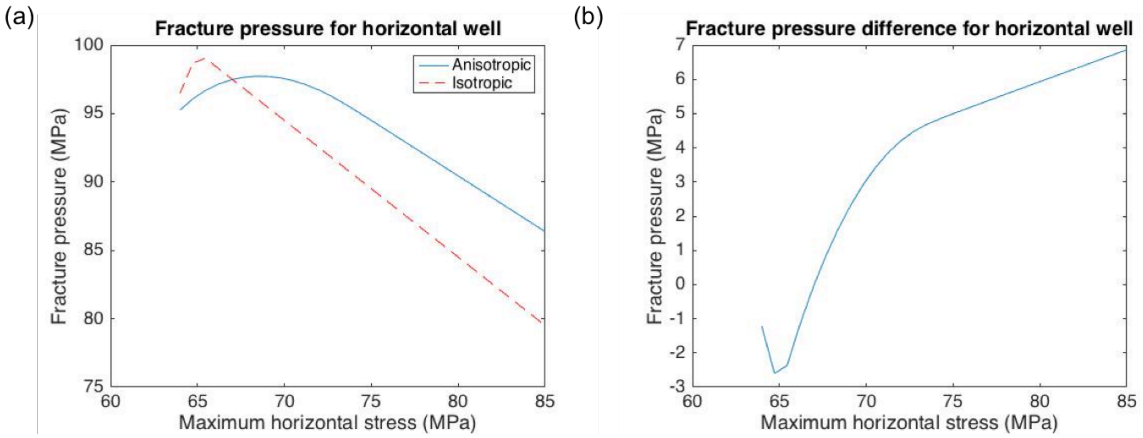

Figure 49: (a) Comparison of fracture pressure in the Lower Barnett Shale at 8500 ft depth as a function of maximum horizontal stress for the anisotropic model vs. the isotropic model of stress around a horizontal borehole. (b) the fracture pressure difference between the anisotropic model and the isotorpic model are various maximum horizontal stress magnitudes. Note that the biot coefficent was assumed to be one in these cases.

We now vary both the maximum horizontal stress and the Biot coefficient to examine their relative effects on the predicted fracture pressure for isotropic and anisotropic solution. Results are shown in Figure 50. Note that as the difference between the overburden stress and the maximum horizontal stress increases, the effect of the material elastic anisotropy is more evident. The difference between the isotropic and anisotropic solution is not sensitive to variability in the Biot coefficient, especially at lower maximum horizontal stress magnitudes. Results for the isotropic and anisotropic fracture pressure predictions show that the fracture pressure is sensitive to both Biot coefficient and the maximum horizontal stress. It is therefore important to obtain accurate estimates of both the maximum horizontal stress and the Biot coefficient in predicting the fracture pressure.

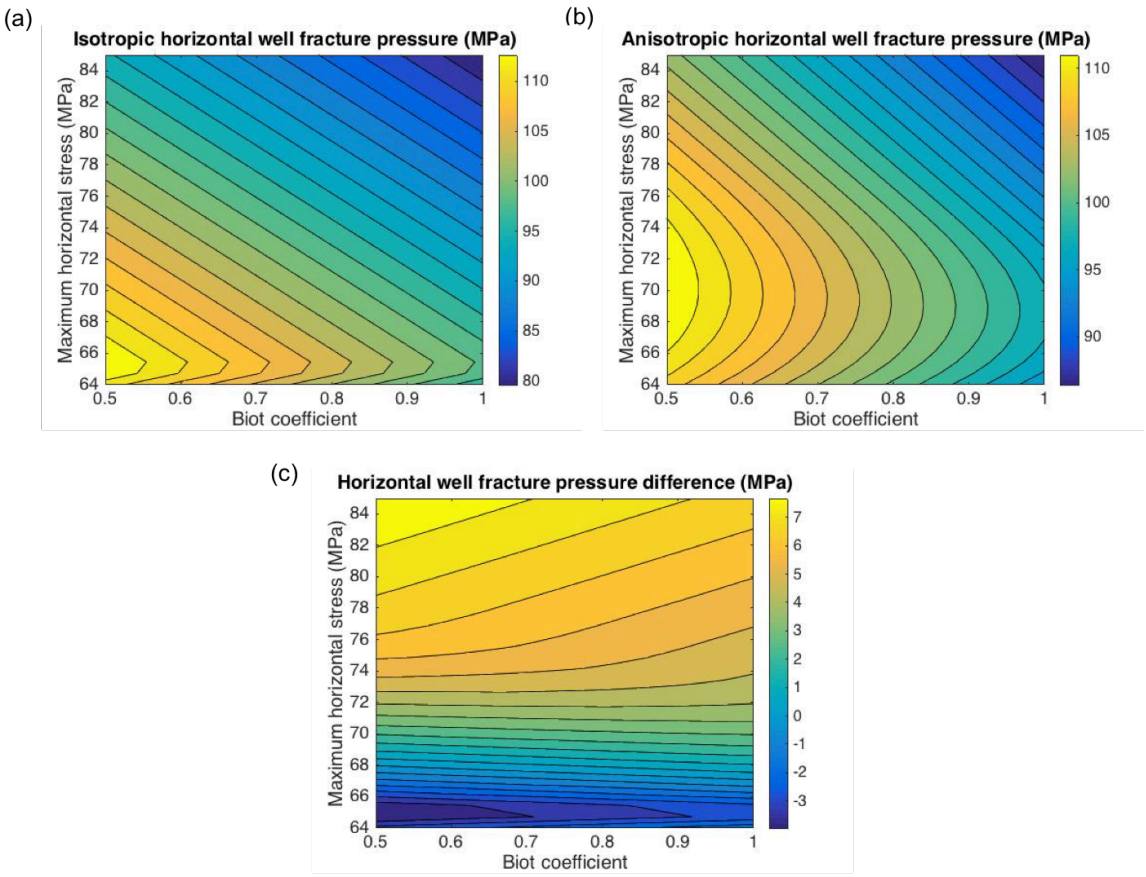

Figure 50: Shown are the contours of the fracture pressure for a horizontal wellbore drilled in the Lower Barnett Shale at a depth of 8500 ft. Both the maximum horizontal stress and the biot coefficent are varied to observe their relative effects on the fracture pressure. Shown in (a) the results from the isotorpic model, (b) results from the anisotropic model and (c) the difference between the anisotropic and the isotropic model.

CONCLUSIONS

Fracturing of the borehole was studied for horizontal wells by use of a linear elastic isotropic and anisotropic model. Input parameters were obtained from Sone et al. (2014), Montgomery et al. (2005) and Bruner et al. (2011). The objective was to compare the predicted fracture pressure from the isotropic and anisotropic model using Lower Barnett Shale, Fort Worth Basin as a case study. More specifically, we examined the

effect of the maximum horizontal stress and the Biot coefficient on the predicted fracture pressure for each model. The results from the analysis done suggest that the larger the difference between the far-field stresses acting on the wellbore, the more evident the effect of the material elastic anisotropy. In addition, the fracture pressure is shown to be sensitive to both the maximum horizontal stress and the Biot coefficient.

Chapter 5: Conclusion

Methods for improving the representation of the current and future state of hydrocarbon reservoirs are explored throughout this thesis. With a CT scan image of real rock, we showed that a combination of the fast marching squared method and the lattice-Boltzmann method can be used to estimate the full permeability tensor. In doing so, we can accurately represent the initial flow behavior of a reservoir.

The reservoir permeability changes throughout the development of the reservoir due to hydrocarbon production. To accurately forecast production, the appropriate coupling between geomechanics and fluid flow must be incorporated into reservoir simulators. Through a combination of the Kirsch equations and the stress-strain constitutive relation for isotropic elastic media, the anisotropic permeability changes around a production well can be modeled by the strain-induces permeability alteration relationship developed in Wong (2003). A case study of a vertical production well in Tor formation in Valhall field was done and our results suggest that the isotropic permeability change assumption commonly used in industry can lead to the overestimation of near-wellbore radial permeability with reservoir depletion due to the high strain anisotropy developed from the hoop stress. The Wong model is therefore a more accurate representation of permeability alteration as pore pressure decreases.

As the Kirsch equations assume isotropic elastic rock properties and real rocks exhibit anisotropic elastic behavior, we then explore the use of the anisotropic counterpart of the Kirsch equations, referred in this thesis as the Amadei solution, to evaluate the fracture pressure profile of the Lower Barnett Shale in Fort Worth Basin (Amadei, 1983). Results show that the use of Kirsch equations to estimate rock failure

modes in anisotropic formations, like the Lower Barnett Shale, can lead to significant error when the far-field stresses acting on the wellbore are highly anisotropic.

RECOMMENDATION FOR FUTURE WORK

FMM^2 has proven to be effective in determining the trajectory of a fluid through the pore-matrix of a rock and estimating tortuosity. FMM^2 has many potential applications in core analysis that were not explored in this thesis. We recommend the validation of FMM^2 use to obtain the pore network of a core sample by identifying the pore connectivity. In doing so, the effective porosity can be estimated and a more accurate representation of the recoverable hydrocarbon in place is obtained. In addition, the scheme presented in combining FMM^2 and LBM to measure the full permeability tensor can be potentially used to obtain the parameters of the Wong model experimentally. The coupling between geomechanics and fluid flow should be studies by imaging a core sample while applying confining pressure through the use of a pressure vessel that is transparent to x-ray. In evaluating the associated deformation to the load applied and measuring the change in the permeability tensor through FMM^2 and LBM, parameters of the Wong model could potentially be obtained experimentally.

Appendices

APPENDIX A

We demonstrate the technique for calculating the tortuosity tensor through a directional tortuosity data set. In two dimensions, this is done by fitting an ellipse centered at the origin to a rose diagram of the directional tortuosity of a porous medium through minimizing the sum of the squared algebraic distances. By doing so, the principal flow directions and maximum and minimum tortuosity are obtained.

The equation of an ellipse centered at the origin is given by

$$F(\underline{a}, \underline{x}) = \underline{a} \cdot \underline{x} = 0 \tag{A.1}$$

where $\underline{a} = [a, b, c, -1]^T$ and $\underline{x} = [x^2, xy, y^2, 1]^T$. $\underline{a} \cdot \underline{x}$ is the "algebraic distance" of a point to the conic $F(\underline{a}, \underline{x}) = 0$. Fitting data to this equation can be done by minimizing $D_A(\underline{a})$, the sum of the squared algebraic distances, in Equation 2.7 (Pilu et al., 1996; Fitzgibbon et al., 1999).

$$D_A(\underline{a}) = \sum_{i=1}^{N} F(\underline{a}, \underline{x_i})^2 \tag{A.2}$$

In Equation A.2, $\underline{x_i} = [{x_i}^2, x_i y_i, {y_i}^2, 1]^T$ and N is the total number of data points. By evaluating $\frac{\partial D(\underline{a})}{\partial a} = 0, \frac{\partial D(\underline{a})}{\partial b} = 0, \frac{\partial D(\underline{a})}{\partial c} = 0$, we obtain the system of equations defined by

$$\begin{bmatrix} X^4 & X^3Y & X^2Y^2 \\ X^3Y & X^2Y^2 & XY^3 \\ X^2Y^2 & XY^3 & Y^4 \end{bmatrix} \begin{bmatrix} a \\ b \\ c \end{bmatrix} = \begin{bmatrix} X^2 \\ XY \\ Y^2 \end{bmatrix} \tag{A.3a}$$

$$C\underline{a} = \underline{b} \tag{A.3b}$$

where $X^n = \sum_{i=1}^{N} {x_i}^n$, $Y^n = \sum_{i=1}^{N} {y_i}^n$, $X^n Y^m = \sum_{i=1}^{N} {x_i}^n {y_i}^m$. Inverting matrix C yields $\underline{a}$ such that $D(\underline{a})$ is minimized and the data-fitted ellipse is obtained.

The principal axis theorem is used to identify the principal tortuosity axes. As described in Strang (1994), Equation A.1 is reformulated such that

$$ax^2 + bxy + cy^2 = [x \quad y]\begin{bmatrix} A_{11} & A_{12} \\ A_{21} & A_{22} \end{bmatrix}\begin{bmatrix} x \\ y \end{bmatrix} = \bar{x}^T A \bar{x} = 1. \tag{A.4}$$

This can be done by setting $A = \begin{bmatrix} a & b/2 \\ b/2 & c \end{bmatrix}$. The tortuosity tensor is given by

$$\tau = V \tau_d V^{-1} \tag{A.5a}$$

$$\tau_d = \begin{bmatrix} \frac{1}{\sqrt{\lambda_1}} & 0 \\ 0 & \frac{1}{\sqrt{\lambda_2}} \end{bmatrix} \tag{A.5b}$$

$$V = [\bar{u}_1 \quad \bar{u}_2] \tag{A.5c}$$

where $\bar{u}_1$, $\bar{u}_2$ and λ_1, λ_2 are the eigenvectors and eigenvalues of A respectively such that $\lambda_1 < \lambda_2$. Note that τ_d is the diagonalized tortuosity tensor hence the maximum and minimum tortuosity are given by ${\lambda_1}^{-0.5}$ and ${\lambda_2}^{-0.5}$. The principal tortuosity axes are given by $\bar{u}_1$ and $\bar{u}_2$, the eigenvectors of matrix A.

APPENDIX B

The methodology for obtaining the tortuosity tensor described in Appendix A can be extended to three-dimensions. The extension of an ellipse in three-dimensions is an ellipsoid, hence directional tortuosity data can be fitted to an ellipsoid and the principal axes theorem is used to identify the principal flow direction and the diagonalized tortuosity tensor.

The equation of an ellipsoid centered at the origin is given by

$$F(\underline{a}, \underline{x}) = \underline{a} \cdot \underline{x} = 0 \tag{B.1}$$

where $\underline{a} = [a, b, c, d, e, f, -1]^T$ and $\underline{x} = [x^2, xy, xz, yz, y^2, z^2, 1]^T$. $\underline{a} \cdot \underline{x}$ is the "algebraic distance" of a point to the conic $F(\underline{a}, \underline{x}) = 0$. Fitting data to this equation can be done by minimizing the sum of the squared algebraic distances.

$$D_A(\underline{a}) = \sum_{i=1}^{N} F(\underline{x}_i)^2 \tag{B.2}$$

Note that $\underline{x}_i = [{x_i}^2, x_i y_i, x_i z_i, y_i z, {y_i}^2, {z_i}^2, 1]^T$ and N is the total number of data points in Equation B.2. By evaluating $\frac{\partial D(\underline{a})}{\partial a} = 0, \frac{\partial D(\underline{a})}{\partial b} = 0, \frac{\partial D(\underline{a})}{\partial c} = 0, \frac{\partial D(\underline{a})}{\partial d} = 0, \frac{\partial D(\underline{a})}{\partial e} = 0,$ $\frac{\partial D(\underline{a})}{\partial f} = 0$, a simultaneous system of equations defined by

$$\begin{bmatrix} X^4 & X^3Y & X^3Z & X^2YZ & X^2Y^2 & X^2Z^2 \\ X^3Y & X^2Y^2 & X^2YZ & XY^2Z & XY^3 & XYZ^2 \\ X^3Z & X^2YZ & X^2Z^2 & XYZ^2 & XZY^2 & XZ^3 \\ X^2YZ & XY^2Z & XYZ^2 & Y^2Z^2 & ZY^3 & YZ^3 \\ X^2Y^2 & XY^3 & XZY^2 & ZY^3 & Y^4 & Y^2Z^2 \\ X^2Z^2 & XYZ^2 & XZ^3 & YZ^3 & Y^2Z^2 & Z^4 \end{bmatrix} \begin{bmatrix} a \\ b \\ c \\ d \\ e \\ f \end{bmatrix} = \begin{bmatrix} X^2 \\ XY \\ XZ \\ YZ \\ Y^2 \\ Z^2 \end{bmatrix} \tag{B.3a}$$

$$C\underline{a} = \underline{b} \tag{B.3b}$$

is obtained where $X^n = \sum_{i=1}^{N} {x_i}^n$, $Y^n = \sum_{i=1}^{N} {y_i}^n$, $X^n Y^m = \sum_{i=1}^{N} {x_i}^n {y_i}^m$. Inverting matrix C yields $\underline{a}$ such that $D(\underline{a})$ is minimized and the data-fitted ellipsoid is obtained.

In order to identify the principal flow direction the principal axes theorem is used. By reformulating the Equation B.1, we obtain

$$ax^2 + bxy + cxz + dyz + ey^2 + fz^2 = \begin{bmatrix} x & y & z \end{bmatrix} \begin{bmatrix} a & b/2 & c/2 \\ b/2 & e & d/2 \\ c/2 & d/2 & f \end{bmatrix} \begin{bmatrix} x \\ y \\ z \end{bmatrix} \tag{B.4}$$
$$= \bar{x}^T A \bar{x} = 1.$$

The tortuosity tensor is given by

$$\tau = V \tau_d V^{-1} \tag{B.5a}$$

$$\tau_d = \begin{bmatrix} \frac{1}{\sqrt{\lambda_1}} & 0 & 0 \\ 0 & \frac{1}{\sqrt{\lambda_2}} & 0 \\ 0 & 0 & \frac{1}{\sqrt{\lambda_3}} \end{bmatrix} \tag{B.5b}$$

$$V = \begin{bmatrix} \bar{u}_1 & \bar{u}_2 & \bar{u}_3 \end{bmatrix} \tag{B.5c}$$

where $\bar{u}_1$, $\bar{u}_2$, $\bar{u}_3$ and $\lambda_1, \lambda_2, \lambda_3$ are the eigenvectors and eigenvalues of A respectively such that $\lambda_1 < \lambda_2 < \lambda_3$. Note that τ_d is the diagonalized tortuosity tensor hence the maximum and minimum permeability are given by ${\lambda_1}^{-0.5}$, ${\lambda_2}^{-0.5}$, and ${\lambda_3}^{-0.5}$. The principal tortuosity axes are given by $\bar{u}_1$, $\bar{u}_2$ and $\bar{u}_3$, the eigenvectors of matrix A.

APPENDIX C

The stress-strain relationship for an isotropic medium is given by Equation C.1. c_{ij} is the matrix representation of the stiffness tensor in Voigt notation. Note that there are two independent elastic constants.

$$\begin{bmatrix}\sigma_{11}\\ \sigma_{22}\\ \sigma_{33}\\ \sigma_{23}\\ \sigma_{31}\\ \sigma_{12}\end{bmatrix} = \begin{bmatrix} c_{11} & c_{12} & c_{12} & 0 & 0 & 0 \\ c_{12} & c_{11} & c_{12} & 0 & 0 & 0 \\ c_{12} & c_{12} & c_{11} & 0 & 0 & 0 \\ 0 & 0 & 0 & c_{44} & 0 & 0 \\ 0 & 0 & 0 & 0 & c_{44} & 0 \\ 0 & 0 & 0 & 0 & 0 & c_{44} \end{bmatrix} \begin{bmatrix}\varepsilon_{11}\\ \varepsilon_{22}\\ \varepsilon_{33}\\ \varepsilon_{23}\\ \varepsilon_{31}\\ \varepsilon_{12}\end{bmatrix}, c_{44} = (c_{11} - c_{12})/2 \tag{C.1}$$

The stress-strain relationship for a transversely isotropic medium is given by Equation C.2. Note that there are five independent elastic constants.

$$\begin{bmatrix}\sigma_{11}\\ \sigma_{22}\\ \sigma_{33}\\ \sigma_{23}\\ \sigma_{31}\\ \sigma_{12}\end{bmatrix} = \begin{bmatrix} c_{11} & c_{12} & c_{13} & 0 & 0 & 0 \\ c_{12} & c_{11} & c_{13} & 0 & 0 & 0 \\ c_{13} & c_{13} & c_{11} & 0 & 0 & 0 \\ 0 & 0 & 0 & c_{44} & 0 & 0 \\ 0 & 0 & 0 & 0 & c_{44} & 0 \\ 0 & 0 & 0 & 0 & 0 & c_{66} \end{bmatrix} \begin{bmatrix}\varepsilon_{11}\\ \varepsilon_{22}\\ \varepsilon_{33}\\ \varepsilon_{23}\\ \varepsilon_{31}\\ \varepsilon_{12}\end{bmatrix}, c_{66} = (c_{11} - c_{12})/2 \tag{C.2}$$

The compliance matrix is obtained by inverting the stiffness matrix. In transforming the compliance matrix into the coordinate frame of the borehole and applying the generalized plain strain assumption, Equation C.3 is obtained. Note that a_{ij} are components of the compliance matrix in Voigt notation in the coordinate frame of the borehole.

$$\begin{bmatrix}\varepsilon_{11}\\ \varepsilon_{22}\\ 0\\ \varepsilon_{23}\\ \varepsilon_{31}\\ \varepsilon_{12}\end{bmatrix} = \begin{bmatrix} a_{11} & a_{12} & a_{13} & a_{14} & a_{15} & a_{16} \\ a_{12} & a_{22} & a_{23} & a_{24} & a_{25} & a_{26} \\ a_{13} & a_{23} & a_{33} & a_{34} & a_{35} & a_{36} \\ a_{14} & a_{24} & a_{34} & a_{44} & a_{45} & a_{46} \\ a_{15} & a_{25} & a_{35} & a_{45} & a_{55} & a_{56} \\ a_{16} & a_{26} & a_{36} & a_{46} & a_{56} & a_{66} \end{bmatrix} \begin{bmatrix}\sigma_{11}\\ \sigma_{22}\\ \sigma_{33}\\ \sigma_{23}\\ \sigma_{31}\\ \sigma_{12}\end{bmatrix} \tag{C.3}$$

APPENDIX D

The governing equations describing stress around a circular cavity in an anisotropic medium are equilibrium equations given by Equation D.1.

$$\nabla\bar{\bar{\sigma}} = 0 \tag{D.1}$$

By application of the generalized plain strain formulation and the stress functions F(x,y) and G(x,y) given by Equation D.2, we obtain the two Beltrami-Michell coupled partial differential equations for a generalized plain strain problem. The Beltrami-Michell equations can be uncoupled such that F is the only dependent variable with x and y as the independent variables. By substituting $e^{x+\mu y}$ for the stress function F we obtain the characteristic equation given by Equation D.3.

$$\begin{aligned}&\sigma_{xx} = \frac{\partial^2 F}{\partial y^2};\ \sigma_{yy} = \frac{\partial^2 F}{\partial x^2};\ \sigma_{xx} = \frac{\partial^2 F}{\partial y^2};\\ &\tau_{xy} = -\frac{\partial^2 F}{\partial x \partial y};\ \tau_{xz} = \frac{\partial G}{\partial y};\ \tau_{yz} = -\frac{\partial G}{\partial x}.\end{aligned} \tag{D.2}$$

$$l_4(\mu)l_2(\mu) - l_3(\mu)^2 = 0 \tag{D.3}$$

$$l_2(\mu) = \beta_{44} - 2\beta_{45}\mu + \beta_{55}\mu^2 \tag{D.4a}$$

$$l_3(\mu) = -\beta_{24} + (\beta_{25} + \beta_{46})\mu - (\beta_{14} + \beta_{56})\mu^2 + \beta_{15}\mu^3 \tag{D.4b}$$

$$l_4(\mu) = -\beta_{22} - 2\beta_{26} + (2\beta_{12} + \beta_{66})\mu^2 - 2\beta_{16}\mu^3 + \beta_{11}\mu^4 \tag{D.4c}$$

β_{ij} are the reduced strain coefficients given by Equation D.5.

$$\beta_{ij} = a_{ij} - \frac{a_{i3}a_{j3}}{a_{33}}, \qquad i,j = 1,\ldots,6. \tag{D.5}$$

Lekhnitskii (1963) has shown that there are six complex or pure imaginary roots to Equation D.3. Three of the roots are principal roots (μ_1, μ_2, μ_3), and the other three are complex conjugates of the principal roots $(\overline{\mu_1}, \overline{\mu_2}, \overline{\mu_3})$.

The equations for the stress around an arbitrarily oriented wellbore in an anisotropic formation are given by Equation D.6-D.14. Note all stresses are in Voigt

notation in the coordinate frame of the borehole. $\bar{\sigma}_{TOH}$ is the far-field in-situ stress in the coordinate frame of the borehole. $\bar{\sigma}_{BH}(\theta)$ is the stress at the wellbore wall at location defined by azimuthal coordinate θ.

$$\bar{\sigma}_{BH}(\theta) = \bar{\sigma}_{TOH} + \bar{\sigma}_{bi}(\theta) \tag{D.6}$$

$$\bar{\sigma}_{bi}(\theta) = \begin{bmatrix} \sigma_{xx,bi} \\ \sigma_{yy,bi} \\ \sigma_{zz,bi} \\ \tau_{yz,bi} \\ \tau_{xz,bi} \\ \tau_{xy,bi} \end{bmatrix} =$$

$$\begin{bmatrix} 2\,\mathrm{Re}\left[{\mu_1}^2 {\phi'}_1(\theta) + {\mu_2}^2 {\phi'}_2(\theta) + \lambda_3 {\mu_3}^2 {\phi'}_3(\theta)\right] \\ 2\,\mathrm{Re}\left[{\phi'}_1(\theta) + {\phi'}_2(\theta) + \lambda_3 {\phi'}_3(\theta)\right] \\ -\left(a_{31}\sigma_{xx,bi} + a_{32}\sigma_{yy,bi} + a_{34}\tau_{yz,bi} + a_{35}\tau_{xz,bi} + a_{36}\tau_{xy,bi}\right)/a_{33} \\ -2\,\mathrm{Re}\left[\lambda_1 {\phi'}_1(\theta) + \lambda_2 {\phi'}_2(\theta) + {\phi'}_3(\theta)\right] \\ 2\,\mathrm{Re}\left[\lambda_1\mu_1 {\phi'}_1(\theta) + \lambda_2\mu_2 {\phi'}_2(\theta) + \mu_3 {\phi'}_3(\theta)\right] \\ -2\,\mathrm{Re}\left[\mu_1 {\phi'}_1(\theta) + \mu_2 {\phi'}_2(\theta) + \lambda_3\mu_3 {\phi'}_3(\theta)\right] \end{bmatrix} \tag{D.7}$$

$$\lambda_1 = -\frac{l_3(\mu_1)}{l_2(\mu_1)};\ \lambda_2 = -\frac{l_3(\mu_2)}{l_2(\mu_2)};\ \lambda_3 = -\frac{l_3(\mu_3)}{l_4(\mu_3)}. \tag{D.8}$$

$$\overline{\phi'}(\theta) = \begin{bmatrix} {\phi'}_1(\theta) \\ {\phi'}_2(\theta) \\ {\phi'}_3(\theta) \end{bmatrix} = \bar{\gamma}(\theta)\Gamma\bar{\omega}(\theta) \tag{D.9}$$

$$\Gamma = \begin{bmatrix} \lambda_2\lambda_3 - 1 & \mu_2 - \mu_3\lambda_2\lambda_3 & \lambda_3(\mu_3 - \mu_2) \\ 1 - \lambda_1\lambda_3 & \mu_3\lambda_1\lambda_3 - \mu_1 & \lambda_3(\mu_1 - \mu_3) \\ \lambda_1 - \lambda_2 & \mu_1\lambda_2 - \mu_2\lambda_1 & \mu_2 - \mu_1 \end{bmatrix} \tag{D.10}$$

$$\bar{\omega}(\theta) = \begin{bmatrix} \left(P_w - \sigma_{xx,TOH}\right)\cos\theta - \tau_{xy,TOH}\sin\theta - i\left[\left(P_w - \sigma_{xx,TOH}\right)\sin\theta + \tau_{xy,TOH}\cos\theta\right] \\ -\left(P_w - \sigma_{yy,TOH}\right)\sin\theta - \tau_{xy,TOH}\cos\theta - i\left[\left(P_w - \sigma_{yy,TOH}\right)\cos\theta + \tau_{xy,TOH}\sin\theta\right] \\ -\tau_{xz,TOH}\cos\theta - \tau_{yz,TOH}\sin\theta - i\left(\tau_{yz,TOH}\cos\theta - \tau_{xz,TOH}\sin\theta\right) \end{bmatrix} \tag{D.11}$$

$$\bar{\gamma}(\theta) = \begin{bmatrix} \gamma_1(\theta) & 0 & 0 \\ 0 & \gamma_2(\theta) & 0 \\ 0 & 0 & \gamma_3(\theta) \end{bmatrix} \tag{D.12}$$

$$\gamma_j(\theta) = \left[-2\Delta\left(\mu_j \cos\theta - \sin\theta\right)\right]^{-1},\ j = 1, \ldots, 3 \tag{D.13}$$

$$\Delta = \mu_2 - \mu_1 + \lambda_2\lambda_3(\mu_1 - \mu_3) + \lambda_1\lambda_3(\mu_3 - \mu_2) \tag{D.14}$$

References

Aadnoy, B.S. (1988). Modeling of the stability of highly inclined boreholes in anisotropic rock formations, *SPE Drilling Engineering, 3*(3), 259-268.

Aadnoy, B.S., & Chenevert M.E. (1987). Stability of Highly Inclined Boreholes. *SPE Drilling Engineering*. 2(4), 364-374.

Aadnoy, B.S. (1991). Effects of reservoir depletion on borehole stability, *Journal of Petroleum Science and Engineering, 6*(1), 57-61.

Addis, M.A. (1997). The Stress-Depletion Response of Reservoirs. SPE38720 was presented at the SPE Annual Technical Conference and Exhibition held in San Antonio, Texas. 508 October.

Ali, A., Kalloo, C.L., & Singh, U.B. (1994). Preventing lost circulation in severely depleted unconsolidated sandstone reservoirs, *SPE Drilling & Completion, 9*(1), 32-38.

Álvarez, D., Gómez, J. V., Garrido, S., & Moreno, L. (2015). 3D Robot Formations Path Planning with Fast Marching Square. *Journal of Intelligent & Robotic Systems*, *80*(3-4), 507-523.

Amadei B. (1983). Rock Anisotropy and the Theory of Stress Measurements. *Lecture Notes in Engineering Series, Volume 2*. Berlin, Heidelberg, New York, Tokyo: Springer-Verlag.

American Petroleum Institute (1956). *API Recommended Practice for Determining Permeability of Porous Media: RP-27*. Dallas, Texas.

American Petroleum Institute (1998). *API Recommended Practices for Core Analysis: RP-40*. Washington, DC.

Bærentzen, J. A. (2001). *On the implementation of fast marching methods for 3D lattices*.

Bhatnagar, P.L., Gross, E.P & Krook, M. (1954). A model for collisional processes in gases I: small amplitude processes in charged and in neutral one-component systems, Phys. Rev. 94, 511-525.

Biot, M. A. (1962). Mechanical Deformation and Acoustic Propagation in Porous Media. *Journal of Applied Physics* 33, 1482-1498.

Bird, R. B., Lightfoot, E. N., & Stewart, E. W. (2007). *Transport phenomenon*. Wiley.

Brace, W.F. (1980). Permeability of crystalline and argillaceous rocks. International Journal of Rock Mechanics, Mining Sciences & Geomechanics Abstracts, 17: 241–251.

Bruner, K., & Smosna, R. (2011). A comparative study of the Mississippian Barnett Shale, Fort Worth Basin, and Devonian Marcellus Shale, Appalachian Basin. U.S. Department of Energy, National Energy Technology Laboratory Report.

Carman, P. C. (1937). Fluid flow through granular beds. *Transactions-Institution of Chemical Engineeres*, *15*, 150-166.

Chan, A. W. (2005). *Production-induced reservoir compaction, permeability loss and land surface subsidence* (Order No. 3153107). Available from ProQuest Dissertations & Theses Global. (305434757). Retrieved from http://ezproxy.lib.utexas.edu/login?url=http://search.proquest.com/docview/305434757?accountid=7118

Clennell, M. B. (1997). Tortuosity: a guide through the maze. *Geological Society, London, Special Publications*, *122*(1) 299-344.

Cui, X., Bustin, A. M. M., & Bustin, R. M. (2009). Measurements of gas permeability and diffusivity of tight reservoir rocks: different approaches and their applications. *Geofluids*, *9*(3) 208-223.

Daigle, H., Dugan, B. (2011). Permeability anisotropy and fabric development: A mechanistic explanation, *Water Resources Research*, *47*, W12517.

Darabi, H., Ettehad, A., Javadpour, F., & Sepehrnoori, K. (2012). Gas flow in ultra-tight shale strata. *Journal of Fluid Mechanics*, *710*, 641-658.

Darcy, H. (1856). Les Fontaines Publiques de la Ville de Dijon, Victor Dalmont, Paris.

Dusseault, M. B., Bruno, M. S., & Barrera, J. (1998, January). Casing shear: causes, cases, cures. In *SPE International Oil and Gas Conference and Exhibition in China*. Society of Petroleum Engineers.

Engelder, T., & Fischer, M. P. (1994). Influence of poroelastic behavior on the magnitude of minimum horizontal stress, Sh in overpressured parts of sedimentary basins. *Geology*, *22*(10), 949-952.

Feeze, R.A., & Cherry, J.A. (1979). *Groundwater*. Englewood Cliffs, NJ: Prentice Hall. 604 pp.

Fitzgibbon, A., Pilu, M., & Fisher, R. B. (1999). Direct least square fitting of ellipses. *Pattern Analysis and Machine Intelligence, IEEE Transactions on*,*21*(5), 476-480.

Gaede, O., Karpfinger, F., Jocker, J., & Prioul, R. (2012). Comparison between analytical and 3D finite element solutions for borehole stresses in anisotropic elastic rock. *International Journal of Rock Mechanics and Mining Sciences*, *51*, 53-63.

Gangi, A. F. (1978, October). Variation of whole and fractured porous rock permeability with confining pressure. In *International Journal of Rock Mechanics and Mining Sciences & Geomechanics Abstracts* (Vol. 15, No. 5, pp. 249-257). Pergamon.

Gao, Y., Zhang, X., Rama, P., Liu, Y., Chen R., Ostadi H., & Jiang K. (2012). Calculating the anisotropic permeability of porous media using the lattice Boltzmann method and X-ray computed tomography. *Transport in porous media, 92(2), 457-472*.

Garrido, S., Moreno, L., Blanco, D., & Martin, F. (2007, September). FM2: A real-time fast marching sensor-based motion planner. In *Advanced intelligent mechatronics, 2007 IEEE/ASME international conference on* (pp. 1-6). IEEE.

Gómez, J. V., Arismendi, C., Garrido, S., & Moreno, L. (2012, May). On path planning: Adaptation to the environment using Fast Marching. In *Evolving and Adaptive Intelligent Systems (EAIS), 2012 IEEE Conference on* (pp. 74-79). IEEE.

Hassouna, S. M., & Farag, A. A. (2007). Multistencils fast marching methods: A highly accurate solution to the eikonal equation on cartesian domains.*Pattern Analysis and Machine Intelligence, IEEE Transactions on*, *29*(9), 1563-1574.

Hillis, R. R. (2001). Coupled changes in pore pressure and stress in oil fields and sedimentary basins. *Petroleum Geoscience*, *7*(4), 419-425.

Johnson, W.E., & Hughes, R.V. (1948). Directional permeability measurements and their significance. *Producers monthly, 13*(1), 17-25.

Kirsch, G. (1898). *Die Theorie der Elastizität und die Bedürfnisse der Festigkeitslehre*. Zeitschrift des Vereines deutscher Ingenieure, 42, 797–807.

Klinkenberg, L. J. (1941, January). The permeability of porous media to liquids and gases. In *Drilling and production practice*. American Petroleum Institute.

Kozeny, J. (1927). *Über kapillare Leitung des Wassers im Boden:(Aufstieg, Versickerung und Anwendung auf die Bewässerung)*. Hölder-Pichler-Tempsky.

Kristiansen, T. G. (2007, December 1). Drilling Wellbore Stability in the Compacting and Subsiding Valhall Field: A Case Study. Society of Petroleum Engineers. doi:10.2118/87221-PA

Latt, J. (2009). Palabos, Parallel Lattice Boltzmann Solver. http://www.palabos.org. Accessed 20 April 2016.

Lekhnitskii S.G. (1963). Theory of elasticity of an anisotropic body. Moscow: MIR Publishers.

Mase, G.E. (1970). Theory and problems of continuum mechanics. McGraw-Hill Book Company, N.Y.

Meng, F., & Fuh, G. (2010). Reservoir Depletion Effect on In-Situ Stresses and Mud Weight Selection. *44 US Rock Mechanics Symposium and 5th US Canada Rock Mechanics Symposium*, Salt Lake City, Utah, 27-30 June.

Mokhtari, M. (2015). Characterization of anisotropy in organic-rich shales: shear and tensile failure, wave velocity, matrix and fracture permeability. PhD thesis. Colorado School of Mines.

Montgomery, S.I., Jarvie, D.M., Bowker, K.A., & Pollastro, R.M. (2005). Mississippian Barnett Shale, Fort Worth basin, north-central Texas: Gas-shale play with multi-trillion cubic foot potential. AAPG Bull. 89 (2), 155-175.

Mordecai, M., & Morris, L.H. (1971). An investigation into the changes of permeability occurring in a sandstone when failed under triaxial stress conditions. In Proceedings of the 12th Symposium of Rock Mechanics, University of Missouri-Rolla, Rolla, Mo., American Institute of Mining, Metallurgy, and Petroleum Engineers (AIME), pp. 221–229.

Munns, J. W. (1985). The Valhall field: a geological overview. *Marine and Petroleum Geology*, *2*(1), 23-43.

Narváez, A., & Harting, J. (2010). Evaluation of pressure boundary conditions for permeability calculations using the lattice-Boltzmann method. *arXiv preprint arXiv:1005.2322*.

Ong, S. (1994). Borehole stability. PhD thesis. University of Oklahoma.

Ong, S., & Roegiers, J. (1995). Fracture initiation from inclined wellbores in anisotropic formations In: International meeting on petroleum engineering, Society of Petroleum Engineers 29993:423–35.

Patillo, P.D., Kristiansen, T.G, Sund, G.V., & Kjelsadli, R.M. (1998). Reservoir

Compaction and Seafloor Subsidence at Valhall. Paper SPE 47274 presented at the SPE/ISRM Rock Mechanics in Petroleum Engineering, Trondheim, Norway, 8-10 July. DOI: 10.2118/47274-MS.

Pilu, M. Fitzgibbon A., Fisher R. *1996. Ellipse-specific Direct least-square Fitting* ", IEEE International Conference on Image Processing, Lausanne, September 1996.

Rushing, J. A., Newsham, K. E., Lasswell, P. M., Cox, J. C., & Blasingame, T. A. (2004, January 1). Klinkenerg-Corrected Permeability Measurements in Tight Gas Sands: Steady-State Versus Unsteady-State Techniques. Society of Petroleum Engineers. doi:10.2118/89867-MS

Scheidegger, A. E. (1954). Directional permeability of porous media to homogeneous fluids. *Geofisica pura e applicata*, *28*(1), 75-90.

Scholes, O. N., Clayton, S. A., Hoadley, A. F. A., & Tiu, C. (2007). Permeability anisotropy due to consolidation of compressible porous media.*Transport in porous media*, *68*(3), 365-387.

Segall, P., & Fitzgeral S. D. (1998). A note on induced stress changes in hydrocarbon and geothermal reservoirs. Technophysics 289 11-128.

Sethian, J. A. (1996). A fast marching level set method for monotonically advancing fronts. *Proceedings of the National Academy of Sciences*, *93*(4), 1591-1595.

Sone, H., & Zoback, M. D. (2013). Mechanical properties of shale-gas reservoir rocks—Part 1: Static and dynamic elastic properties and anisotropy.*Geophysics*, *78*(5), D381-D392.

Sone, H., & Zoback, M. D. (2014). Viscous relaxation model for predicting least principal stress magnitudes in sedimentary rocks. *Journal of Petroleum Science and Engineering*, *124*, 416-431.

Strang, G. (*1994). Introduction to Linear Algebra*. Wellesley-Cambridge Press. *ISBN 0-9614088-5-5*.

Streit, J.E., & Hillis, R.R. (2002). Estimating fluid pressures that can induce reservoir failure during hydrocarbon depletion. SPE/ISRM Rock Mechanics Conference, Society of Petroleum Engineers, Irving, Texas, 20-23 October 2002, paper SPE 78226.

Sukop M., & Thorne D. Jr. (2006). Lattice Boltzmann Modeling: An Introduction for Geoscientists and Engineers. New York: Springer

Sulak, A.M., Danielsen, J. (1988). Reservoir aspects of Ekofisk subsidence, Offshore Technology Conference. Society of Petroleum Engineers, Houston, Texas, 2-5 May 1988, paper SPE 5618.

Terzaghi, K.V. (1924). Die Theorie der hydrodynamischen Spannungserscheinungen und ihr erdbautechnisches Anwendungsgebiet. Proc., First International Congress for Applied Mechanics, Delft, The Netherlands, 22–26 April, 288–294.

Teufel, L. W., Rhett, D. W. & Farrell, H. P. (1991). Effect of reservoir depletion and pore pressure drawdown on in situ stress and deformation in the Ekofisk field, North Sea. In: Roegiers, J. C. (EDS), Rock mechanics as a multidisciplinary science: 63-72. Rotterdam: Balkena.

Tortike, W.S., & Farouq Ali, S.M. (1993). Reservoir Simulation Integrated with Geomechanics. Journal of Canadian Petroleum Technology, Vol. 32, No. 5, pp. 28-37.

Touhidi-Baghini, A. 1998. Absolute permeability of McMurray Formation oil sands at low confining stresses. Ph.D. thesis, Department of Civil and Environmental Engineering, University of Alberta, Edmonton, Alta.

Valero-Gomez, A., Gomez, J. V., Garrido, S., & Moreno, L. (2013). Fast Marching Methods in Path Planning. *IEEE Robotics and Automation Magazine, no*.

van Oort, E., Gradishar, J., Ugueto, G., Cowan, K.M., Barton, K.K., & Dudley, J.W. (2003). Accessing deep reservoirs by drilling severely depleted formations. SPE/IADC Drilling Conference, Society of Petroleum Engineers, Amsterdam, The Netherlands, 19-21 February 2003, paper SPE 79861.

Van Uitert, R., & Bitter, I. (2007). Subvoxel precise skeletons of volumetric data based on fast marching methods. *Medical physics*, *34*(2), 627-638.

Wang, Y., & Xue, S. (2002, January). Coupled reservoir-geomechanics model with sand erosion for sand rate and enhanced production prediction. In*International Symposium and Exhibition on Formation Damage Control*. Society of Petroleum Engineers.

Witt, K. J., & Brauns, J. (1983). Permeability-anisotropy due to particle shape.*Journal of geotechnical engineering*, *109*(9), 1181-1187.

Wong, R. C. (2003). A model for strain-induced permeability anisotropy in deformable granular media. *Canadian geotechnical journal*, *40*(1), 95-106.

York, S. D., Pong, C. P., & Joslin, T. H. (1992, August 1). Reservoir Management of Valhall Field, Norway. Society of Petroleum Engineers. doi:10.2118/20992-PA

Zhai, Z., & Sharma, M.M. (2005). A new approach to modeling hydraulic fractures in unconsolidated sands. SPE Annual Technical Conference and Exhibition, Society of Petroleum Engineers, Dallas, Texas, 9-12 October 2005, paper SPE 96246.

Zoback, M.D. & Zinke, J.C. (2002). Production-induced normal faulting in the Valhall and Ekofisk oil fields. Pure and Applied Geophysics, 159, 403-420.

Zou, Q. &He, X. (1997). On pressure and velocity boundary conditions for the lattice Boltzmann BGK model. Phys. Fluids 9, 1591-1598.